Journal Name

Dynamic Article Links ▶

ARTICLE TYPE

Cobalt-based compounds and composites as electrode materials for high-performance electrochemical capacitors†

Kian Keat Lee,[*a] **Wee Shong Chin,**[*a] **and Chorng Haur Sow**[b]

Transition metal compounds (oxides, hydroxides *etc.*) are emerging electrode materials for electrochemical capacitors (ECs) due to their rich redox properties involving multiple oxidation states and different ions. Pseudocapacitance derived from the reversible faradaic reactions can be ten times higher than the state-of-the-art carbon-based electric double layer capacitors (EDLCs). As one of the most well-
10 known electroactive inorganic materials, extensive studies of cobalt-based compounds (Co_3O_4, $Co(OH)_2$, CoOOH, CoS *etc.*) for ECs have mushroomed, and the relevant literatures have grown exponentially in the past ten years. This review consolidates and evaluates the recent progress, achievements, weaknesses and challenges in the research of cobalt-based compounds and nanocomposites for ECs. The triangular relationship between synthesis strategies, tailored material properties and the electrochemical
15 performances are thoroughly assessed, unveiling the advanced electrode material design and development.

1. Introduction

In the list of the "Top Ten Problems Facing Humanity for Next 50 Years" outlined by Professor Richard E. Smalley ten years
20 ago, among the complex, interconnected and multi-faceted grand challenges, "Energy" was prioritized as the single most important problem.[1, 2] Ever-increasing world energy demand, coupled with the diminishing fossil fuel reserves and environmental issues associated with fossil fuels consumption, has brought increasing
25 pressures towards the development of clean and renewable energy sources. Successful exploitations of renewable but intermittent energy sources such as solar and wind power require efficient and reliable electrical energy storage, with electrochemical energy storage serving as the key components.[3-5]
30 Electrochemical energy storage technologies include batteries, fuel cells and electrochemical capacitors (ECs).[4, 6-42] The differences of the trio are best simplified by a Ragone plot.[4, 6, 22, 30] Accordingly, ECs deliver much higher power density while compensatory lower energy density than batteries. The border
35 between batteries and ECs has been blurred with recent advancements in "high rate/power" batteries and "battery-like" pseudocapacitors. However, ECs can still be differentiated from batteries based on their operational characteristics namely: 1) symmetrical (high reversibility) and sloping charge-discharge
40 profiles, 2) very short charge-discharge time (a few seconds), 3) exceptional cycle life, and 4) continuous variation of free energy with the degree of conversion.[14, 43]

Based on charge storage mechanisms, ECs can be categorized into two groups: electric double layer capacitors
45 (EDLCs) and pseudocapacitors (also known as redox and faradaic supercapacitors). EDLCs based on high surface area carbonaceous materials continue to expand due to their versatile

forms[44-53] such as activated carbons[54, 55], carbon aerogels[56], carbide-derived porous carbons[57], templated-porous carbons[57],
50 carbon nanotubes[54, 58-63] and graphene materials[64-70]. In spite of the impressive progress, carbon-based EDLCs face a major bottleneck of its intrinsic limit of charge stored in the form of electric double layer, and thus resulting in low energy density. To increase the energy density of ECs, additional charge storage
55 system offered by transition metal compounds[43, 71-78] and conductive polymers[79] presents a viable alternative. Pseudocapacitance reactions involve (quasi-)reversible redox reactions at the surface of electrodes. On charging (discharging), ions (K^+, H^+, OH^- *etc.*) are inserted/ absorbed to (extracted/
60 desorbed from) an electrode; with the electrons transfer through the external circuit.

Early research on pseudocapacitors has been focused on noble metal oxides such as RuO_2 and IrO_2. Notably, RuO_2 is a conductive metal oxide with three oxidation states accessible
65 within 1.2 V, exhibiting an impressive reported specific capacitance up to 1580 F/g.[22, 43, 80] The extremely high cost limits their use in space and military applications. Hence, cheaper base transition metal oxides such as manganese oxides, iron oxides, nickel oxides and cobalt oxides are actively studied. Among
70 them, manganese oxides are the most investigated due to their environmental abundance and low cost, with reasonably high capacitance (normally ranged in 20-400 F/g with some exceptional cases near to 700 F/g) in 1 V.[73] However, their poor cycling stability, low mass loading and low density, low
75 conductivity associated with unsatisfactory high rate capability remain to be improved.

Being widely used in electrocatalysts and secondary batteries, cobalt-based compounds and composites have also been

extensively studied as pseudocapacitors. Especially in the last five years, extraordinary achievements were accomplished arising from better understanding in materials design: specific capacitances closed to theoretical value (up to 3000 F/g),[81] high areal capacitance (25 F/cm^2) based on high mass loading,[82] cycling stability up to 10000 cycles,[83] among others. To date, nonetheless, there is no exclusive review dedicated to this important material family. This review thus presents a timely effort to critically and comprehensively evaluate the development, in order to promote future breakthroughs in this field.

We will begin the discussion with a brief account of basic properties of cobalt compounds, follow by detailed assessment on the triangular relationship of advanced electrode materials design through various synthesis strategies, materials properties and the resultant electrochemical performance as presented in Scheme 1. Finally, a summary and outlook for future studies is presented.
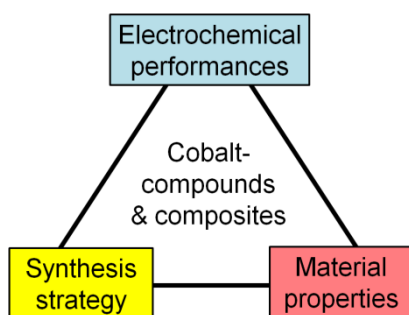
Synthesis strategy:

1. Low dimensional nanostructures
2. Binder-free and self-standing nanoarrays
3. Composition tuning
4. Nanostructured current collectors
5. Synergistic coupling of binary or multiple components
6. Complex nanoarchitectural design of electrodes

Materials properties:

1. Chemical properties: composition
2. Textural properties: surface area and porosity
3. Structural properties: structure and morphology
4. Electrical properties: impedance and conductivity

Electrochemical performances:

1. Specific (gravimetric) and areal capacitances
2. High rate capability
3. Cycling stability
4. Potential window

Scheme 1. Discussion framework of this review

2   Basic properties of cobalt compounds

2.1   Early pseudocapacitance studies and electrochemistry of cobalt compounds

Early electrochemical studies on cobalt hydroxide or oxide electrodes were motivated by the chemical similarities between cobalt and nickel.[84, 85] The utilization of transition metal oxides as pseudocapacitance for electrochemical energy storage was demonstrated by pioneering work of Conway and co-workers in 1990s.[35, 86, 87] In 1997, Srinivasan and Weidner electrodeposited metal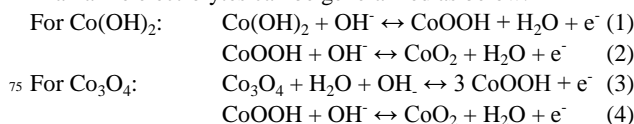 hydroxide films followed by heating in air to obtain porous metal oxide films.[88] Cobalt oxides electrodes exhibited a specific capacitance of ~10 F/g in a two-electrode device. High surface area cobalt hydroxide xerogel powder was prepared by Lin *et al.*[89] in 1998 using a sol-gel process. Amorphous Co(OH)$_2$ heated at 150 °C exhibited the highest surface area (198 m^2/g) and largest pore volume (0.43 cm^3/g), thus presenting the highest capacitance of 291 F/g. The capacitance was attributed to a surface redox mechanism, considering the one-electron exchange redox reaction taking place on the particle surfaces.

The electrochemical reactions and formation of different cobalt phases at the cobalt-based electrodes can be interpreted by comparing the equilibrium potentials of the current peaks with those calculated from the thermodynamics and potential-pH diagram (Pourbaix diagram).[90-92] The electrode potentials calculated by Behl and Toni[93] as well as the half cell reactions were presented in Table 1. In the lower potential range, the redox reaction should be related to Co(II)/ Co(III) system. While at higher potential preceding oxygen evolution reaction (OER), the Co(III)/ Co(IV) system should predominate. Notably, the oxidation peak of CoOOH → CoO$_2$ is often hidden by the polarization curve of OER.[93-95]

Table 1 Standard equilibrium potentials in the Co/KOH systems. Reproduced from Ref. [93] with permission from Elsevier.

Electrode couple	Half-cell reaction	V vs. Hg/HgO
Co(OH)$_2$/Co$_3$O$_4$	3Co(OH)$_2$ + 2OH$^-$ ↔ Co$_3$O$_4$ + 4H$_2$O + 2e-	-0.192
CoO/Co$_3$O$_4$	3CoO + 2OH$^-$ ↔ Co$_3$O$_4$ + H$_2$O + 2e-	-0.369
Co(OH)$_2$/CoOOH	Co(OH)$_2$ + OH$^-$ ↔ CoOOH + H$_2$O + e-	-0.054
CoO/CoOOH	CoO + OH$^-$ ↔ CoOOH + e-	-0.172
Co$_3$O$_4$/CoOOH	Co$_3$O$_4$ + OH$^-$ + H$_2$O ↔ 3CoOOH + e-	+0.222
Co(OH)$_2$/CoO$_2$	Co(OH)$_2$ + 2OH$^-$ ↔ CoO$_2$ + 2H$_2$O + 2e-	+0.254
CoO/CoO$_2$	CoO + 2OH$^-$ ↔ CoO$_2$ + H$_2$O + 2e-	+0.195
Co$_3$O$_4$/CoO$_2$	Co$_3$O$_4$ + 4OH$^-$ ↔ 3CoO$_2$ + 2 H$_2$O + 4e-	+0.477
CoOOH/CoO$_2$	CoOOH + OH$^-$ ↔ CoO$_2$ + H$_2$O + 4e-	+0.562

The redox reactions involved at Co(OH)$_2$ and Co$_3$O$_4$ electrodes in alkaline electrolytes can be generalized as below:[93-104]

For Co(OH)$_2$: $Co(OH)_2 + OH^- \leftrightarrow CoOOH + H_2O + e^-$ (1)

$CoOOH + OH^- \leftrightarrow CoO_2 + H_2O + e^-$ (2)

For Co$_3$O$_4$: $Co_3O_4 + H_2O + OH_- \leftrightarrow 3\ CoOOH + e^-$ (3)

$CoOOH + OH^- \leftrightarrow CoO_2 + H_2O + e^-$ (4)

2.2   Oxidation mechanism between different cobalt compounds and topotactic relationship

Understanding of the oxidation mechanism[84, 85, 105-107] between different cobalt compounds is crucial based on two reasons: 1.) the syntheses of cobalt oxide and oxyhydroxide nanomaterials often involve the transformation of intermediate phases such as cobalt hydroxide,[108-121] cobalt oxyhydroxides,[122-124] and cobalt carbonates;[113] 2.) the oxidation mechanism is relevant to the electrochemical cycling rate and stability, as well as thermal stability of the electrodes.

2.2.1   Oxidation of Co(OH)$_2$ to CoOOH

Electrochemical oxidation and chemical oxidation–Benson *et al.*[80] observed the phase transition of blue Co(OH)$_2$ (α form) to black CoOOH via anodic oxidation, while atmospheric oxidation of blue Co(OH)$_2$ in KOH solution yielded brown CoOOH. The structurally different forms of CoOOH were possibly due to two different types of mechanism: 1.) nucleation of new phase via a

solution intermediate corresponding to the slow atmospheric oxidation, and 2.) transformation of the lattice by electron and proton migration through the solid phase corresponding to the anodic oxidation.

The oxidation mechanism via electrochemical/chemical routes has been further investigated systematically.[106] The positive $Co(OH)_2$ electrode dismantled from a charged $Co(OH)_2/Cd$ cell (electrolyte: 5 M KOH) over 20 h was evaluated. It was found that the oxidation reaction was biphasic. The final product was β-CoOOH particles with irregular contours. This transformation is referred to as *metasomatic* process, where dissolved chemical species react on the external surface of a solid. On the other hand, chemical oxidation of $Co(OH)_2$ to β-CoOOH with NaClO (8 M) in 5 M KOH was *pseudomorphic*, aka the phase change did not change the particle morphology. Accordingly, a single particle domain consisted of several slightly disoriented coherent diffraction domains. In addition, SAED pattern of partly transformed particles indicated the topotactic relationship between the $Co(OH)_2$ precursor and oxidized β-CoOOH product: the [001] and [110] axis directions of the β-$Co(OH)_2$ phase were parallel to the [003] and [110] directions of the β-CoOOH phase, respectively. Both pseudomorphic retention and topotactic relationship implied that the reaction most likely occurred in the solid state. The mosaic texture was due to the induced strain within the particles during solid state growth caused by the unit cell mismatch between the β-$Co(OH)_2$ and β-CoOOH.

Hydrothermal oxidation–Chemical oxidation of $Co(OH)_2$ in 5 M KOH under hydrothermal condition (oxygen pressure of 20 bar) produced hexagonal β-CoOOH with irregular contours possessed high porosity and internal granular structure. The oxidation reaction followed two steps: 1.) partial dissolution of $Co(OH)_2$ and growth of CoOOH on the exterior or grain boundaries of the partially dissolved $Co(OH)_2$; 2.) the initial platelet cores undergo solid state transformation, which involved a proton diffusion process. The misfit due to strain thus produced an internal mosaic structure.

Isothermal oxidation–By isothermal heating in an air flow or water suspension, Figlarz et. al.[105] studied the solid evolution of β-$Co(OH)_2$ (rose color) to CoOOH. Isothermal heating of β-$Co(OH)_2$ at 60 °C in an air flow produced CoOOH particles with fine porosity and cracks. The decreased crystallite sizes deduced from the (101̄1) diffractions based on Scherrer formula were 8, 6, 7 nm, at 60, 80 and 100 °C respectively. Furthermore, the phase transformation was *topotactic* as revealed by SAED. The hexagonal unit cell axes of CoOOH were parallel to the unit cell axes of $Co(OH)_2$ although the CoOOH crystallites were more misoriented.

2.2.2 Oxidation of CoOOH to Co_3O_4

Based on XRD result, CoOOH totally decomposed to Co_3O_4 by heating in air at 250 °C.[107] The major morphology of CoOOH was retained, the inhomogeneous porosity of CoOOH however turned to Co_3O_4 of regular porosity with tiny round pores. According to SAED pattern, the thermal transformation was a topotactic reaction with [001] and [111] axis directions of CoOOH phase parallel to [110] and [110] axis directions of Co_3O_4 phase. Moreover, the {110} CoOOH reflections were not separated from the {440} Co_3O_4 reflections due to the very close value of their interplanar spacings (1.425 Å for CoOOH d_{110} and

1.429 Å for Co_3O_4 d_{440}).

2.2.3 Oxidation of $Co(OH)_2$ to CoO or Co_3O_4

Topotactic transformation of $Co(OH)_2{\rightarrow}CoO$[125] and $Co(OH)_2{\rightarrow}Co_3O_4$[119, 126] has also been reported. β-$Co(OH)_2$ has a brucite-like layered structure with an interlayer spacing of 4.65 Å, while spinel Co_3O_4 has cubic structure with 3-fold symmetry viewed along [111]. Thus, β-$Co(OH)_2$ to Co_3O_4 transition is topotactic with the relationship [001] $Co(OH)_2$//[111] Co_3O_4.

3. Cobalt oxide (Co_3O_4) electrodes

3.1 Powder electrodes

3.1.1 Chemical precipitation[127-136]

During chemical precipitation, various process parameters are controllable to obtain Co_3O_4 with desirable composition, structure, morphology and properties.[127, 128, 134, 135, 137-142] By tuning the amount, combination and feeding order of various reactants, Wang *et al.* achieved controllable synthesis of cobalt oxalates of different morphologies.[127] Cobalt oxalates decomposed to Co_3O_4 upon calcination, largely with their original morphologies conserved. The BET specific surface area of Co_3O_4 nanorods, nanowires and layered parallel folding (LPF) nanostructures were 45.1, 35.6 and 75.9 m²/g. The average pore diameters were 17.28, 19.37 and 8.58 nm for the Co_3O_4 nanorods, nanowires and LPF nanostructures. Correspondingly, the samples exhibited specific capacitances of ~128 (nanorods), ~103 (nanowires) and ~203 (LPF nanostructures) F/g. The higher capacitances demonstrated by the LPF nanostructures can be attributed to their higher surface area, smaller pores and particle sizes which shorten the diffusion length of OH⁻ ions. Morphologies influence the surface area and porosity of electrode materials and thus determine the resultant charge storage properties.[127, 141]

Heat treatment temperatures also affected the textural properties of a material. As the calcination temperature to convert $Co(OH)_2$ microflowers into Co_3O_4 porous microflowers increased from 300 to 500 °C, the crystal sizes and pore diameter enlarged.[128] The BET specific surface areas for the samples heat-treated at 300, 400 and 500 °C were 77.33, 32.02 and 12 m²/g, respectively. The decreasing surface areas of the samples with the increasing calcination temperatures were due to nanocrystals aggregation. As expected, sample calcined at 300 °C presented higher specific capacitance (160 F/g) than samples calcined at 400 °C (88 F/g) and 500 °C (71 F/g).

Guerlou-Demourgues and co-workers prepared Co_3O_4 by chemical precipitation in ternary alkaline medium of KOH (8 M), NaOH (0.5 M) and LiOH (0.5 M).[129] Their works dealt with the development of conductive spinel cobalt oxide, which is a significant aspect for high performance ECs. Generally pure Co_3O_4 possesses normal cubic spinel structure (space group Fd3m) and is insulating. In the presence of LiOH, conductive nanosized cobalt oxides containing hydrogen and lithium within the structure and exhibiting a high electronic conductivity (10⁻¹ S.cm⁻¹ at room temperature) were prepared. The markedly improved conductivity was due to the presence of Co^{4+} ions which ensure a charge balance and thus allow an electronic delocalization in the octahedral network.[130] The average

oxidation state of cobalt determined from the iodometric titration method was higher in this conductive Co_3O_4 (2.81) than in the ideal spinel (2.67). With only 5 % of carbon black additive in the composite electrode, the maximum specific capacitance of 320 F/g was obtained.

Using anodic aluminum oxide (AAO) as a hard template, Xu *et al.* obtained Co_3O_4 nanotube bundles after precipitation, heat treatment and template removal.[131] The BET specific surface area and the pore sizes of the Co_3O_4 nanotubes were 218 m^2/g and 38-110 nm, respectively. The specific capacitances of the Co_3O_4 nanotubes were 574, 551, 538 and 484 F/g at 0.1, 0.2, 0.5 and 1 A/g, respectively. The electrode also demonstrated good cycling stability to retain 95 % of capacitance after 1000 cycles. Combination of polystyrene (PS) spheres and carbowax (polyethylene glycol) were used as templates to fabricate mesoporous Co_3O_4 and meso-macroporous Co_3O_4 electrodes. The meso-macroporous Co_3O_4 electrode exhibited the highest specific capacitance of 453 F/g. Su and coworkers[132] applied saw dust with particle size of 0.3-2 nm as template to synthesize Co_3O_4 nanoparticles with the highest specific capacitance of 290 F/g.

Cao and coworkers[133] prepared a series of mesoporous Co_3O_4 nanoparticles by using mesoporous silicas, KIT-6 and SBA-15 as templates. The BET surface area and porosity of mesoporous Co_3O_4 nanoparticles could be tuned by different KIT-6 templates with different textural parameters. The specific capacitances decreased with the increase of the calcination temperature due to the decrease of the BET surface area. The specific capacitance of the sample with the highest BET surface area of 184.8 m^2/g was 370 F/g. Large pore size and high order of mesopore in the sample facilitated ion transfer. However, the electrochemical results indicated that the interior surface of mesoporous sample was not fully utilized probably due to the weak electrical conductivity of metal oxide.

Thermal treatment of various precipitated precursors, such as cobalt-citrate complex[134] and cobalt acetate hydroxide[135] led to mesoporous structures and hollow boxes of Co_3O_4 with the highest capacitances of ~427 F/g and ~278 F/g, respectively.

3.1.2 Hydrothermal/solvothermal method[143-157]

Hydrothermal or solvothermal synthesis is a group of methods to crystallize inorganic substances from aqueous (thus named hydrothermal) or organic (thus named solvothermal) solutions at elevated vapour pressures and temperatures.[143, 144] In comparison to co-precipitation and sol-gel methods, the products of hydro/solvothermal are crystalline, eliminating the necessity of post-annealing in some cases.[145] Overall, hydro/solvothermal methods offer benefits such as high reaction yield, low cost of equipment setup and reagents, energy efficient and versatility of controllable parameters.[145-147] Through hydrothermal synthesis, both powder and thin-film (grown on current collectors) electrodes can be conveniently prepared via different nucleation and growth routes.

By tuning the volume ratio of water and ethanolamine, β-$Co(OH)_2$ hexagonal nanosheets or microspheres self-assembled from nanosheets were synthesized.[148] Pure phase spinel mesoporous Co_3O_4 were obtained by thermal treatment of β-$Co(OH)_2$. The BET specific surface area and micropore area were 25.12 and 2.80 m^2/g for the Co_3O_4 nanosheets, 21.53 and 1.29 m^2/g for the Co_3O_4 microspheres, respectively. The average pore

diameters were 26.7 and 23.5 nm for the Co_3O_4 nanosheets and microspheres respectively. The specific capacitances of the Co_3O_4 nanosheets were 92, 91, 90 and 85 F/g at 5, 10, 15, 20 mA/cm^2. By reacting cobalt salt and urea under hydrothermal conditions followed by a thermal treatment, Co_3O_4 nanorods with specific capacitances of 281 and 456 F/g were obtained.[149, 150]

Controllable synthesis of cobalt carbonate hydroxide nanostructures with different morphologies and their thermal conversion to pure phase Co_3O_4 nanostructures were reported.[151-154] Among the different samples (needle-like nanorods, leaf-like nanosheets, microparticles) synthesized in PEG-H_2O medium,[150] needle-like nanorods presented the highest capacitance as expected from the BET specific surface area. The Co_3O_4 nanorods possessed BET specific surface area of 121.5 m^2/g, compared to 86.16 and 110.2 m^2/g for leaf-like nanosheets and microparticles respectively. The specific capacitance for the nanorods, nanosheets and microparticles were 111, 44 and 62 F/g respectively. Porous Co_3O_4 nanowires thermally converted from the long $Co(CO_3)_{0.5}(OH).0.11H_2O$ nanowires exhibited improved specific capacitances of 260 F/g.[152]

By a proper choice of surface directing agents (e.g. neutral surfactant Triton X-100 and biomolecule, lysine), Co_3O_4 complex architectures such as micrometer-length ultralayered structure[155] and urchin-like Co_3O_4 microspherical hierarchical superstructures[156] were synthesized. The microscopic ultralayers with high surface area (97 m^2/g) and mesopore volume (0.2 cm^3/g) allowed quicker electrolyte permeation by reducing the diffusion time of OH^- ions, and secured sufficient Faradaic reactions at high rate. The specific capacitances were 604, 548, 474, 359 and 167 F/g at 4, 8, 16, 32 and 64 A/g. The oriented Co_3O_4 nanowires in the radial organization as shown in Figure 1a-d created abundant V-shape porous channels that would facilitate the fast electrolyte penetration into the complex structures and react with the electroactive surfaces.[156] Optimized ionic diffusion pathway is necessary to reduce ionic diffusion resistance and charge transfer resistance, in order to achieve high electrochemical utilization at high rate. Each Co_3O_4 nanowire was formed by many connected Co_3O_4 nanoparticles (10-50 nm). The superstructures were stable even under prolonged ultrasonication. A type-IV N_2 adsorption-desorption isotherm with a hysteresis loop in the range of ca. 0.5-1.0 P/P_o indicated the sample possessed multi-modal and hierarchical macro/mesoporosity. The BET specific surface area, BJH average pore diameter and mesopore volume were ca. 113 m^2/g, 28 nm and 0.32 cm^3/g, correspondingly. The specific capacitances at 1 and 4 A/g were 614 and 536 F/g respectively. Based on the BET specific surface area, capacitance attributable to EDLC was estimated as ca. 23 F/g.

A morphology evolution of nanorods to sheaf-like bundles, to flower-like structures, to dumbbell-like particles, and eventually twin-sphere with an urchin-like structure was presented.[157] A proposed multi-step splitting growth mechanism provided a chance to control the morphology of different dimensionalities and structures. The resultant 3D hierachical Co_3O_4 twin spheres fabricated into electrode exhibited high specific capacitance of 781 F/g, high rate capability and cycling stability.

3.1.3 Sol-gel method[158, 159]

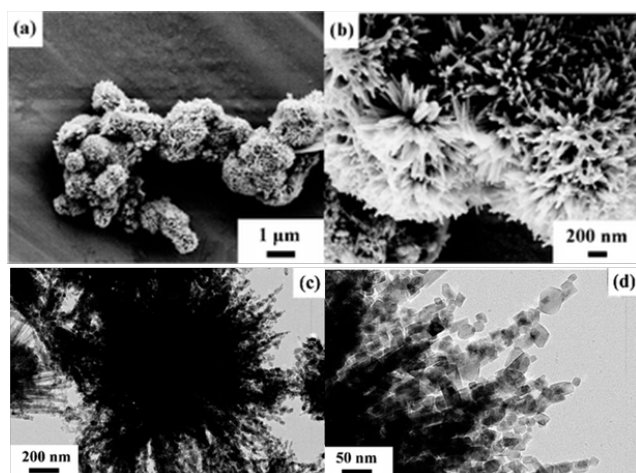Hu and colleagues prepared cobalt oxide aerogels via an

Fig. 1 SEM and TEn M images of urchin-like microspherical hierarchical superstructures constructed by Co_3O_4 nanowires composed of connected nanoparticles. Adapted from Ref. [156].

epoxy-mediated sol-gel procedure, followed by supercritical carbon dioxide drying and calcination.[158] In the thermal treatment, they observed an increase of Co_3O_4 grain size from 8 to 12 nm with increasing calcination temperature from 200 to 400 °C. The highest specific surface area of 235 m^2/g was observed for samples calcined at 200 °C, followed by a drastic drop to 123 m^2/g at 300 °C and 69 m^2/g at 400 °C. All aerogel samples exhibited type IV isotherms and type H3 hysteresis loops typical for mesoporous features. The specific capacitances (potential window: 0.23-0.53 V) were 623, 239, 174 F/g for Co_3O_4 aerogels calcined at 200, 300 and 400 °C, respectively. Clearly, the specific capacitances decreased with the lowering of specific surface areas, consistent with the observations made by Popov et al[89].

Lee and co-workers presented a sol-gel route coupled with a freeze-drying method to synthesize interconnected macro-/mesoporous Co_3O_4 nanocrystals.[159] Comparatively, cryogel offers several advantageous features: 1.) higher porosity due to low surface tension during drying, 2.) enabling a macroporous structure from an ice-templated effect, 3.) lower agglomerations. The sample prepared by using triblock polymer P123 as a template at pH 3 exhibited BET surface area of 82.8 m^2/g. Although the surface area of the sample was lower than previous sol-gel synthesized cobalt oxide samples[89, 158], it demonstrated a higher specific capacitance of 742 F/g.

3.2 Thin film electrodes

3.2.1 Hydrothermal/solvothermal method[160-167]

Co_3O_4 nanoflower structures on Ni foam were prepared via solvothermal synthesis followed by post-annealing.[160] The nanosheets were grown on the entire surface of Ni foam at various angles, offering efficient electron transport channels (Figure 2a-b). Sample post-annealed at 250 °C exhibited specific capacitances of ~1937, ~1518, ~1377, ~1309 F/g at the current densities of 0.2, 1, 2, 3 A/g in a narrow potential window of 0-0.34 V. Nevertheless, the electrode suffered from a considerable loss of 21.8 % capacitance after 1000 cycles, possibly due to the material dissolution in high concentration KOH electrolyte (6 M). Zhang et al.[161] deposited Co_3O_4 nanoparticles on Ni sheet by hydrothermal method without post-annealing step (Figure 2c-d).

The authors noted that the pre-etching step of Ni sheet determines the phase of cobalt compounds: β-$Co(OH)_2$ formed on HCl-etched Ni sheet but Co_3O_4 formed on HNO_3-etched Ni sheet. Co_3O_4 nanoparticles (NPs) with mean size ranging from 50-150 nm with mesopores between neighbouring NPs were observed. The porosity helped the electrolyte ions to penetrate into the inner electrode and contact with a larger electroactive surface for Faradaic reactions. A specific capacitance of 928 F/g was obtained at 1.2 A/g. When the current density increased to 12 A/g, 84 % (776 F/g) of the specific capacitance was retained, showing a high rate capability. Mesoporous Co_3O_4 nanowire arrays were also prepared on HCl-etched Ni foam.[162] The sample exhibited improved capacitances of 1160 and 861 F/g at 2 and 20 A/g respectively, demonstrating 71 % capacitance retention when the charge-discharge current density increased from 2 to 20 A/g.

Co_3O_4 nanowire arrays were grown on the seed-coated substrates (Ni foil, Ni foam and Si wafer).[163] Without the presence of oxygen, only interconnected $Co(OH)_2$ nanowalls were obtained. An annealing step was required to transform the mixed phases to pure Co_3O_4 phase. The nanowires exhibited porous structures with roughened walls and hollow center. The porosity allows easier electrolyte penetration, while roughened walls and hollow center present high surface-to-bulk ratio for ions transport and diffusion. The hollow Co_3O_4 nanowire arrays exhibited specific capacitance of 295 and 599 F/g before and after 1000-cycle activation. Capacitance retention of 73 % was observed when the current density increased from 2 A/g to 40 A/g. Notably, a high Co_3O_4 mass loading of 15 mg/cm^2 was used in their study and thus a high areal capacitance (~9 F/cm^2) was achieved. After 7500 cycles, the sample retained 91 % and 82 % of the highest capacitance value at 2 A/g and 10 A/g, respectively. The same research group also successfully prepared Co_3O_4 nanowire arrays on Ni foam by hydrothermal method with an annealing step.[164] In the presence of NH_4F as surface-directing agent, smooth and very long (25 μm) single-crystalline cobalt carbonate hydroxide nanowires were obtained (Figure 2e, f). After annealing in argon, rough Co_3O_4 nanowires consisted of interconnected nanoparticles with high mesoporosity were obtained and attributed to the release of CO_2 and H_2O during thermal conversion process (Figure 2g, h). After activation, the specific capacitances were 754 and 610 F/g at 2 and 40 A/g respectively, presenting an excellent high rate capability. The electrode exhibited remarkable cycling stability for 4000 cycles.

Beside single-component nanostructures, Yang et al. reported the synthesis of hierarchical Co_3O_4 nanosheet @ nanowire arrays (NSWA) on Ni foam (Figure 3).[165] The hierarchical structures involved firstly the formation of nanosheet arrays on Ni foam and secondly the growth of the nanowires around the nanosheets. NH_4F was an essential additive in the hydrothermal synthesis. In the absence of NH_4F, the mass loading of Co_3O_4 NSWA was only less than 1.5 mg/cm^2, about 5 times lower when the sample was synthesized in the presence of NH_4F. In addition, the presence of NH_4F helped to increase the adhesion between Co_3O_4 NSWA and the substrate. The specific capacitances of the Co_3O_4 NSWA were 715 and 491 F/g (5.44 and 3.73 F/cm^2) at 5 and 30 mA/cm^2, respectively. In comparison, single-component Co_3O_4 nanosheet arrays and nanowire arrays exhibited lower specific capacitance or inferior rate capability. The enhanced capacitance and rate

capability were undoubtedly attributed to the synergistic effect of the three-dimensional architecture of the hierarchical structures. Higher electroactive surface area, hierarchical porosity and open space, enhanced electrolyte-electrode contact area and good adhesion between current-collector and active materials, are all positive factors leading to an impressively high capacitance, especially an areal capacitance of ~5.44 F/cm^2.
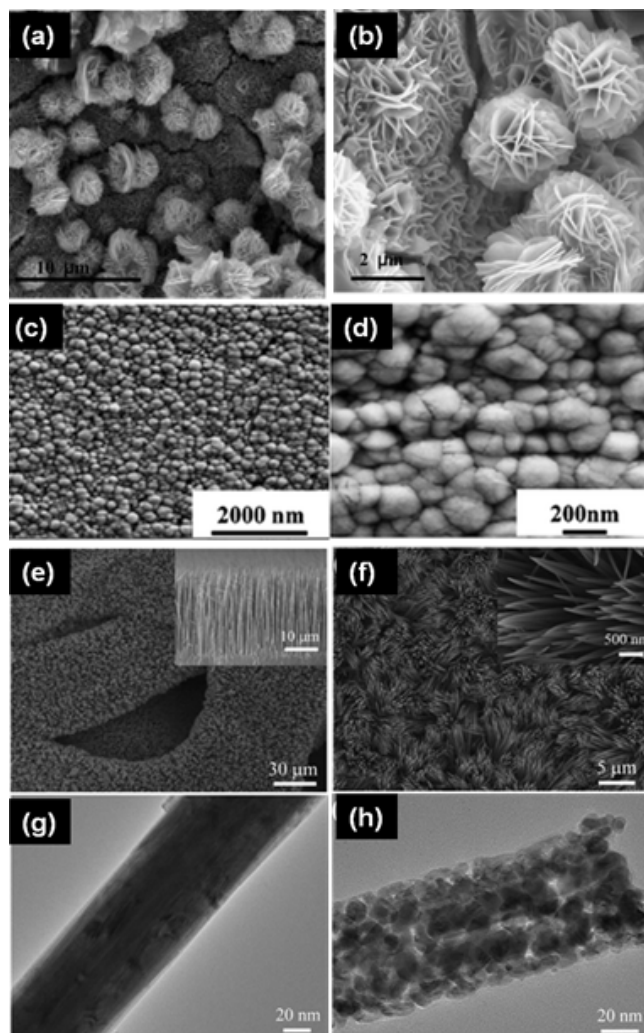

Fig. 2 Self-supported Co_3O_4 nanostructures with different morphologies on Ni substrates synthesized by hydrothermal methods. SEM images of nanosheets (a, b), nanoparticles (c, d) and nanowire arrays (e, f); TEM images of smooth $Co_2(OH)_2(CO_3)_2$ nanowire (g) and Co_3O_4 nanowire after annealing (h), demonstrates that thermal decomposition of precursors involves release of H_2O and CO_2 often generates mesoporosity on the nanostructures. (a, b) adapted with permission from Ref. [160], ©2011 Elsevier; (c, d) adapted from Ref. [161], (e-h) adapted from [164].

By employing monolayer polystyrene spheres as template, Duan and Cao fabricated hierarchical porous Co_3O_4 film composed of monolayer hollow sphere arrays and the porous net-like nanoflakes.[166] The individual nanoflake composed of nanoparticles with the size of ~5-15 nm and showed continuous pores ranging from 2-5 nm. Compared with the Co_3O_4 nanoflakes synthesized without the template, the hierarchical porous Co_3O_4 film exhibited smaller potential separation between redox peaks and has better reaction reversibility. Hierarchical porous Co_3O_4 film also had smaller polarization during the charge-discharge

processes. The specific capacitances of hierarchical porous Co_3O_4 film and Co_3O_4 nanoflakes were 352 and 325 F/g respectively at 2 A/g. For the hierarchical porous Co_3O_4 film and Co_3O_4 nanoflakes, 82.7 % and 66.8 % of capacitance were retained when discharge current density increased from 2 to 40 A/g. In addition, hierarchical porous Co_3O_4 film also presented better cycling stability.
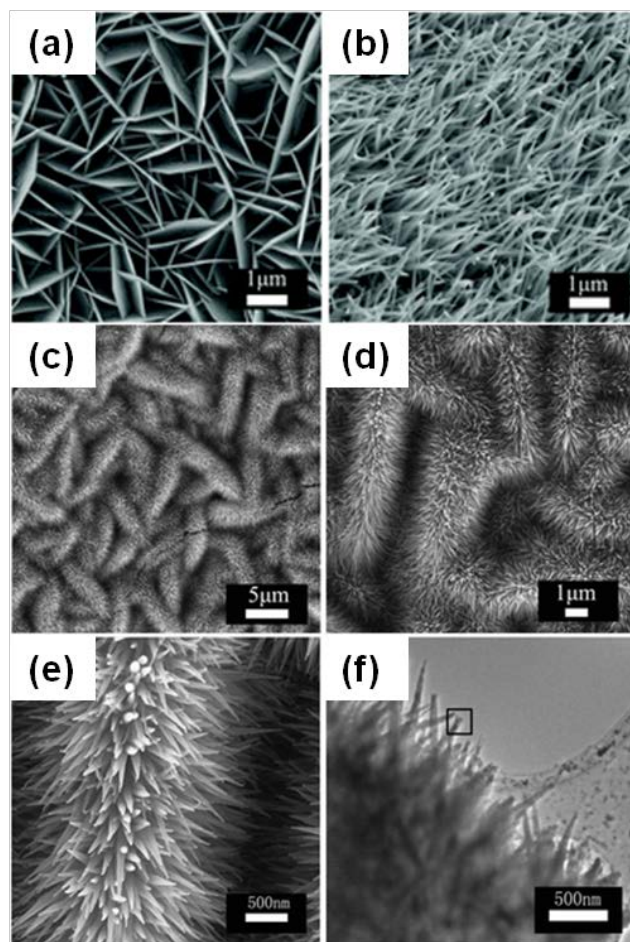

Fig. 3 SEM images of Co_3O_4 nanosheet arrays (a), nanowire arrays (b), Co_3O_4 nanosheet @ nanowire arrays (NSWA) (c-d) grown on Ni foam; (f) TEM image of NSWA. Adapted from Ref. [165].

3.2.2 Chemical bath deposition[168-181]

Chemical bath deposition (CBD, or known as chemical solution deposition), is a simple wet chemical technique to deposit wide varieties of thin films on various substrates.[168-171] CBD involves the occurrence of a relatively slow chemical reaction in solution resulting in the formation of a solid reaction product on a substrate. Similar chemical precursors can be used for CBD, hydrothermal method and chemical precipitation. However, hydrothermal method involves the use of sealed autoclave and higher temperature synthesis; while the main product of chemical precipitation appears as powders.

Co_3O_4 nanowire arrays were deposited on Ni foam[172] and Ti substrate[173] by an ammonia-evaporation method.[174] The open space between the loosely packed nanowires allows easy diffusion of electrolyte into the inner region of the electrode, resulting in reduced internal resistance and improved capacitance.

With a high mass loading of 16 mg/cm^2, the sample on Ni foam exhibited a high specific capacitance of 746 F/g in 6 M KOH.[172] However, the capacitance decreased to 86 % after 500 cycles. Using KOH of higher concentration, the specific capacitance increased with more pronounced redox peaks, due to decreasing internal resistance and electrolyte starvation near the material surface. The Co$_3$O$_4$ nanowires grown on Ti substrate were further deposited by Ag nanoparticles. The specific capacitance of the Co$_3$O$_4$ nanowires-Ag was found to be 1006 F/g, improved from that at 922 F/g of the pristine Co$_3$O$_4$ nanowires. More importantly, Ag deposition improved the rate capability substantially from 54.2 % to 95 % (capacitance retention at 10 A/g compared to 2 A/g). Both the electrodes demonstrated good cycling life by retaining more than 95 % of the initial capacitance after 5000 cycles.

Lokhande and co-workers deposited cobalt oxide layer onto copper substrates by controlled hydrolysis of hexamine complex.[175] The maximum specific capacitance of 118 F/g for the sample was obtained at 1.5 M KOH electrolyte. The current under CV curve has decreased by 4.71 % up to 500 cycles. On a side note, it has been widely reported that Cu substrates reacted with basic solutions (e.g. NaOH and ammonia) to form Cu(OH)$_2$ and CuO nanostructures on the surface.[176-179] Consequently, the possibility of capacitance contributed by copper oxide/hydroxide as well as long term stability of copper substrates as current collectors in alkaline electrolytes need to be further clarified.

Huang et al.[180] prepared porous Co$_3$O$_4$ thin film composing of spherical coarse particles on ITO coated glass plate. The sample exhibited a maximum specific capacitance of 227 F/g at 0.2 A/g but reduced to 152 F/g (67 %) when the current density increased to 1.4 A/g. The specific capacitance dropped substantially to 66 % after 500 cycles and remained stable up to 1000 cycles. The capacitance loss was believed to be associated to the loss of active material due to dissolution or detachment during early cycles. Mitlin's group has grown various Co$_3$O$_4$ micro/nanostructures (e.g. lath-like, necklace-like and net-like morphologies) on Ni foam by simply tuning the bath temperature.[181] Among the different morphologies, Co$_3$O$_4$ net-like structures presented the best specific capacitance of 1090 F/g with a mass loading of 1.4 mg/cm^2.

3.2.3　Electrodeposition[182-186]

Srinivasan and Weidner compared electrodeposited cobalt oxide's performance as either positive or negative electrodes in devices.[182] In addition, the capacitances of Co(OH)$_2$ and Co$_3$O$_4$ heat-treated at different temperatures were studied, along with the charge storage mechanism. When electrodeposited Co(OH)$_2$ was heated to temperatures between 100 and 350 °C, the capacitance of the film decreased. For films heated to 300 °C and below, CVs showed the presence of a redox reaction in addition to electric double layer (EDL) capacitance. Notably, the authors commented that, at low temperature, the occurrence of H$^+$ diffusion allows the bulk material to be accessed, while on heating, the reaction shifts to OH$^-$ adsorption on the surface. Overall, the Co$_3$O$_4$ film exhibited specific capacitances of 76 and 164 F/g as the negative and positive electrodes, respectively.

Lee et al.[183] prepared different electrodeposited Co$_3$O$_4$ thin films on ITO glass substrates in the absence or presence of surfactants cetyltrimethylammonium bromide (CTAB) and sodium dodecyl sulfate (SDS). Without surfactant, the sample displayed a dendrite like morphology, while sample prepared in the presence of 1 % CTAB appeared as sphere-like morphology with a mean pore size of 3-4 nm and a wall thickness of 3-4 nm. In comparison, specific capacitance of Co$_3$O$_4$-CTAB (491 F/g) was higher than those of Co$_3$O$_4$-SDS (373 F/g) and Co$_3$O$_4$-without surfactant (255 F/g).

Wu et al.[184] prepared Co$_3$O$_4$ film of vertically-aligned interconnected nanowalls on Ni foam by cathodic electrodeposition followed by annealing. The open spaces between the nanowalls had a diameter of 30 to 300 nm, providing huge porosity for electrolyte diffusion and sufficient contact between the active materials and electrolyte. In comparison, the specific capacitances of the Co$_3$O$_4$ nanowalls film and Co$_3$O$_4$ dense film were 325 and 230 F/g at 2 A/g, respectively. In addition, the Co$_3$O$_4$ nanowalls film exhibited a higher discharge plateau and a lower charge plateau, indicating lower internal resistance and smaller polarization. When current density increased 20 times to 40 A/g, the Co$_3$O$_4$ nanowalls film retained the specific capacitance at 76.0 %, while the Co$_3$O$_4$ dense film secured the specific capacitance at 72.6 %. Moreover, the porous film of Co$_3$O$_4$ nanowalls possessed better cycling stability over the dense film. After 2000 cycles, the porous film of Co$_3$O$_4$ nanowalls preserved its original structure, but many cracks were present in the dense film probably due to volume change during charge-discharge cycles.

Alternatively, electrodeposition methods can be employed in the presence of template structures to replicate a wide variety of structures. By using liquid crystalline template, Yuan et al.[185] prepared hierarchically porous Co$_3$O$_4$ film of interconnected porous nanowalls. In contrast to the sample prepared without liquid crystalline template[184], the nanoflakes presents a continuous net-like structure possessing fine pores of 5-25 nm. Nanoparticles in the nanoflakes showed mesoporous walls with mesopores of 2-3 nm. The hierarchical porous Co$_3$O$_4$ film showed 37 % increment of specific capacitance (443 F/g) than the Co$_3$O$_4$ film prepared without liquid crystalline template[184]. The capacitance retained at 94.3 % of the maximum specific capacitance after 3000 cycles. Tu and co-workers[186] used polystyrene (PS) spheres as a template to prepare Co$_3$O$_4$ monolayer hollow sphere arrays. The skeleton of the arrays was made of interconnected 600-nm hollow spheres, and the interstices between the hollow spheres were filled with Co$_3$O$_4$ nanoflakes. The sample exhibited specific capacitance of 358 F/g at 2 A/g and retained 85 % of capacitance when the current density increased to 40 A/g. Upon cycling, the capacitance increased up to 500 cycles and remained constant over 4000 cycles, displaying excellent stability.

3.2.4　Spray deposition[187, 188]

Spray pyrolysis is a solution deposition technique by spraying the solution (aerosol) directly on a heated substrate surface. By spraying a cobalt chloride solution onto heated fluorine-doped tin oxide (FTO) coated glass substrates, the formed Co$_3$O$_4$ grainy thin film exhibited specific and areal capacitances of 74 F/g and 32 mF/cm^2.[187] On the other hand, Guduru's group presented a solution precursor plasma deposition route to prepare nanostructured and porous Co$_3$O$_4$ thin film on a stainless steel sheet.[188] The high temperatures of plasma plume accelerated the

thermo-chemical conversion of cobalt acetate solution into Co_3O_4 agglomerates or fused particles. The Co_3O_4 thin film possessed specific capacitance of ~250 F/g at 0.2 A/g and this reduced to ~150 F/g when current density increased to 4.5 A/g. However, the thin film suffered from capacitance loss of 27.8 % after 1000 cycles.

4.   Cobalt hydroxide ($Co(OH)_2$) electrodes

4.1   Powder electrodes

4.1.1   Chemical precipitation[189-193]

Mesoporous α-$Co(OH)_2$ with high BET surface area of 283 m^2/g, pore size distribution of 2-50 nm and average pore size of 11 nm was synthesized by chemical precipitation.[189] A specific capacitance of 341 F/g was obtained for the mesoporous α-$Co(OH)_2$. The α-$Co(OH)_2$ electrode experienced a considerable loss of 19 % capacitance after 700 cycles. Subsequently, the same research group applied an ultrasonic-assisted precipitation to obtain β-$Co(OH)_2$ whisker-like structures.[190] The β-$Co(OH)_2$ nanowhiskers sample possessed a BET surface area of 112 m^2/g and specific capacitance of 325 F/g at 20 mA/cm^2 (1.33 A/g). When the charge-discharge current density increased to 80 mA/cm^2 (5.33 A/g), the electrode retained 85.8 % (279 F/g) of the highest specific capacitance. More importantly, the electrode demonstrated an improved cycling life and retain 93 % of the initial specific capacitance after 1000 cycles.

Two different series of α-$Co(OH)_2$ with different intercalated anions (Cl^-, NO_3^-, CH_3COOH^-, SO_4^{2-} and dodecyl sulfate, benzoate, nitrate) were synthesized by two different research groups.[191, 192] The intercalated anions of different radii presented critical effects on the structural, morphological, compositional and surface properties of the α-$Co(OH)_2$ products. For example, the specific capacitances of the samples with intercalated chloride, nitrate, acetate and sulfate were 697, 638, 526 and 420 F/g respectively. It is interesting to note that although the sample with intercalated sulfate possessed smaller crystallite size, more disordered structure and almost perfect alveolate nanostructure with a large surface area, this sample gave poorer specific capacitance. The phenomenon was explained by the hydrogen bonding between the interlayer water molecules and OH groups bound to cobalt ions, and the affinity between the intercalated anions and protons. Hydrogen bonding may be beneficial to mitigating polarization of the electrode or enhancing utilization of the active materials. As shown by TG-DTG analysis and IR spectra, the content of interlayer water in the intercalated samples decreased in the order of chloride, nitrate, acetate and sulfate anions. The electrodes underwent degradation during continuous cycling for 100 cycles, thus resulting in noticeable capacitance loss.

Kong et al.[193] employed a low temperature (10 °C) method to prepare α-$Co(OH)_2$ nanoflakes by precipitation, followed by heat treatment in air at different temperatures. After heating at 150 °C and higher temperatures, the samples were converted to spinel Co_3O_4. The as-synthesized α-$Co(OH)_2$ showed loosely packed and interconnected nanoflakes. After heat treatment, the nanoflakes grew to a stacking structure due to the loss of H_2O during annealing. The BET specific surface area of the α-$Co(OH)_2$ and Co_3O_4 materials obtained at 100 and 250 °C were 85.4 and 71

m^2/g, respectively. Meanwhile, the pore size distribution of the α-$Co(OH)_2$ and Co_3O_4 were 4-20 and 5-50 nm, respectively. The specific capacitances of the α-$Co(OH)_2$ electrode were 735, 702, 637.5 and 609 F/g, respectively at 5, 10, 20 and 30 mA/cm^2. With increasing annealing temperature, the capacitances of converted Co_3O_4 electrodes decreased due to the decrease in surface area.

4.1.2   Hydrothermal method[194-196]

Zhang and co-workers developed biomolecule-assisted hydrothermal processes to synthesize different $Co(OH)_2$ mesocrystals and nano-superstructures.[194-196] When lysine was used, three-dimensional urchin-like β-$Co(OH)_2$ microspheres were obtained.[193] The oriented nanowires in a radial form created abundant V-shape porous channels. N_2 adsorption-desorption isotherm revealed that the sample possessed multi-modal and hierarchical macro- and mesoporosity. Pore size distribution showed a peak at ~4.7 nm attributable to mesopores in the nanowires, and another peak at 20-100 nm attributable to the V-shape porous channels. In summary, the hierarchical 3D nanostructures exhibited BET specific surface area of 101 m^2/g, mesopores volume of 0.3 cm^3/g and average pore size of 15 nm. The specific capacitance of the β-$Co(OH)_2$ sample was 421 F/g at 10 mA/cm^2 (~1.33 A/g) and remained at 370 F/g when current density increased to 40 mA/cm^2 (~5.33 A/g). After continuous 1000 cycles, the specific capacitance of the electrode decreased ~3.6 %. Flowerlike β-$Co(OH)_2$ hierarchical superstructures self-assembled from mesoporous (~3 nm) nanobelts were synthesized when $Co(SO_4)_2.6H_2O$ was used as the cobalt precursor.[196] When L-arginine was used as hydrolysis-controlling agent[195], α-$Co(OH)_2$ triangular nanosheets with a thickness of ~10 nm (Figure 4) were synthesized. Each porous nanosheet was composed of many isolated nanocrystals of 2-3 nm. Further analysis by SAED (Figure 4h) presented clear spotted pattern which is associated with single crystallinity characteristic of the mesocrystals. The narrow pore size distribution of the mesocrystal nanosheets was centered at 1.6 nm. At 10 mA/g (~1.33 A/g) and 40 mA/g (~5.33 A/g), the α-$Co(OH)_2$ mesocrystal nanosheets displayed specific capacitances of 506 and 427 F/g, respectively. The electrode showed good cycling stability to retain 97.0 % of its initial capacitance after 1000 cycles.

4.2   Thin film electrodes

4.2.1   Hydrothermal method[197, 198]

Beside growing various $Co(OH)_2$ nanostructures in the form of powder, hydrothermal route also allows the growth of $Co(OH)_2$ nanostructures directly onto substrates.[197, 198] The one-dimensional and well-aligned nanowire arrays grown directly on substrates established efficient and fast electron transport pathways, and is able to reduce the ionic diffusion to the inner part of electrodes, thus improving utilization of the active materials. The specific capacitance of the binder and additive-free α-$Co(OH)_2$ electrode was ~643 F/g.[196]

4.2.2   Electrochemical deposition[199-210]

Gupta et al.[199] fabricated α-$Co(OH)_2$ nanosheets on stainless steel by cathodic potentiostatic deposition. The thickness of the nanosheets was 10 nm and the thickness of the deposit was several micrometers. For a α-$Co(OH)_2$ mass loading of 0.8

mg/cm^2, specific capacitances of 881 and 772 F/g were obtained at 1 and 10 A/g, respectively. The studies showed that the electrode exhibited remarkably high rate capability and cycling stability.

5   An ordered mesoporous α-Co(OH)$_2$ nanosheets were electrodeposited on Ni foam and Ti plate, using liquid crystals as the surface directing agent.[200-202] The low angle XRD pattern of the designated H$_I$-e Co(OH)$_2$ sample exhibited well-defined peak at 2θ = 1.42° corresponding to a d-spacing of 6.2 nm and a
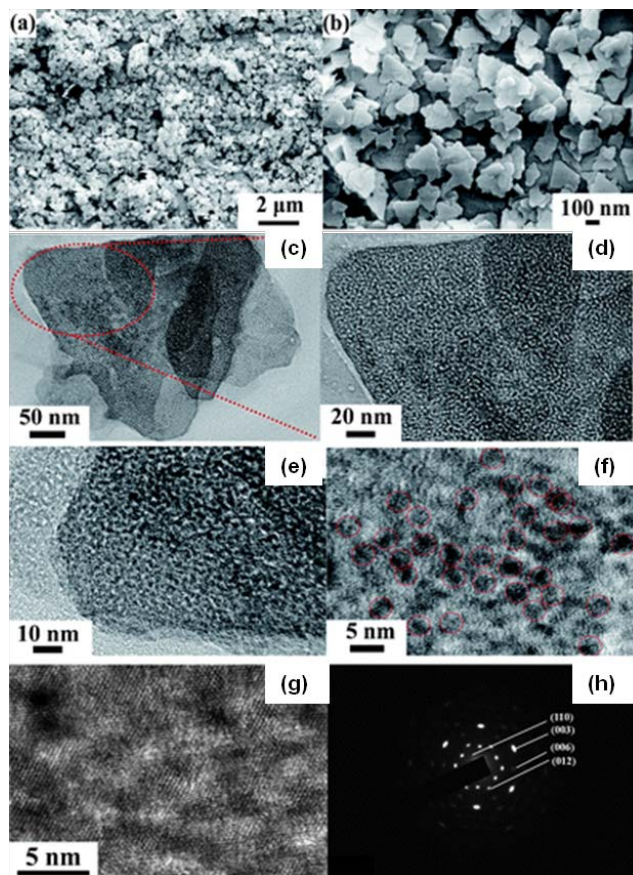
10   **Fig. 4** SEM (a, b), TEM (c-e), HRTEM (f, g) images and SAED (h) of α-Co$_3$O$_4$ mesocrystal nanosheets synthesized by L-arginine-assisted hydrothermal route. Adapted from Ref [195].

pore-to-pore distance of 7.2 nm. The ordered mesoporosity was
15 contributed from the templating effect of the lyotropic liquid crystalline; this was further confirmed by the absence of low angle diffraction for Aq-e Co(OH)$_2$ sample electrodeposited without the template. Comparatively, the H$_I$-e Co(OH)$_2$ presented a more uniform, continuous and dense growth of interlaced
20 nanosheets (Figure 5), while the Aq-e Co(OH)$_2$ exhibited discontinuous distribution of coarse and aggregated nanosheets. Under TEM observation, the H$_I$-e Co(OH)$_2$ nanosheet showed a well-ordered mesoporous structure consisting of cylindrical pores of about 3 nm arranged on a hexagonal lattice. The pore wall
25 thickness was about 4 nm with the center-to-center pore distance of about 7 nm. The specific capacitances of the H$_I$-e Co(OH)$_2$ and Aq-eCo(OH)$_2$ deposited on Ti plates were 1084 and 370 F/g, respectively. The remarkably improved capacitance of the H$_I$-e Co(OH)$_2$ was attributed to the nanoscale ordered mesoporosity
30 and the corresponding higher surface area. In comparison with

planar Ti plate, Ni foam with large cavities allowed better dispersion of the α-Co(OH)$_2$ mesoporous nanosheets, as well as easy penetration of electrolyte to access the active materials. Specific capacitances of 2646 and 2274 F/g were obtained at 8
35 and 48 A/g respectively for the H$_I$-e Co(OH)$_2$ deposited on Ni foam.

Most reported cobalt oxide and cobalt hydroxide electrodes exhibited pseudocapacitance in a limited potential window, which eventually limits the energy and power density of their devices.
40 Nayak and Munichandraiah reported an effort to understand the origin of the small potential window of electrodeposited Co(OH)$_2$ and to tune the potential window by varying the electrolyte and its concentration.[203] They have found that the anodic and cathodic current peaks became increasingly broader by decreasing the
45 NaOH concentration to 0.5 M, 0.1 M and 0.05 M (Figure 6a). In addition, the peak potentials shifted towards the positive direction. The OER potential extended to about 0.85 V in 0.05 M NaOH. On the other hand, when Na$_2$SO$_4$ was used as electrolyte, OER commenced at about 1.30 V (Figure 6b). Specific
50 capacitances obtained in 1 M, 0.1 M and 0.05 M NaOH were 487, 390 and 375 F/g in potential windows of 0.60, 0.75, 0.85 V, respectively. Despite the lower capacitance when 0.05 M NaOH was used, it offered a higher energy density and power density due to the larger potential window.
55 Chou *et al.* prepared 20-30 nm amorphous Co(OH)$_2$ nanoflakes on stainless steel mesh by galvanostatic electrodeposition followed by annealing at 150 °C.[204] For the smallest mass loading of 0.14 mg/cm^2, the specific capacitance was 562 F/g at 0.1 mA/cm^2. When the mass loading was
60 increased to 0.62 mg/cm^2 the specific capacitance decreased by less than 5 %. After 3000 cycles, the electrode suffered a loss of 19 %. Importantly, the authors analyzed the CV curves after 50 and 3000 cycles, which showed that the amorphous Co(OH)$_2$ gradually transformed to Co$_3$O$_4$ during cycling. Electrochemical
65 Impedance Spectroscopy (EIS) showed that the electrochemically active specific surface area of the electrode remained virtually unchanged after 3000 cycles, indicating that the capacitance loss after 3000 cycles was due to the phase conversion.

Dai's group synthesized Co(OH)$_2$ nanoflakes on etched Ni
70 foam by cathodic potentiostatic deposition in water and water-ethanol (1:1) mixed solution.[205] They found that the Co(OH)$_2$ nanoflakes deposited in water-ethanol (2369 F/g) possessed higher specific capacitance than Co(OH)$_2$ nanoflakes deposited in water (1035 F/g). The significantly higher specific capacitance of
75 Co(OH)$_2$ nanoflakes deposited in water-ethanol was attributed to characteristics of ethanol that can reduce the surface strain and improve the attachment between the Ni foam and liquid boundary during deposition. In addition, ethanol was possibly embedded into the layered structure of Co(OH)$_2$ to increase the layer
80 distance between crystal lattices, thus enhancing the reversibility of the Co^{2+}/Co^{3+} redox reaction.

Ma's group added various amount of N-methylpyrrolidone (NMP) in their deposition solutions for cathodic potentiostatic deposition of Co(OH)$_2$ nanosheets on stainless steel.[206] In the
85 presence of 20 % NMP, the densest Co(OH)$_2$ nanosheets of 10 nm thickness were obtained. The specific capacitances of the Co(OH)$_2$ samples prepared with 0, 10, 20, 30 vol. % NMP in the deposition electrolyte were 473, 571, 651 and 473 F/g,

correspondingly. Clearly, the best capacitance was achieved by the sample prepared with 20 vol. % NMP in the deposition electrolyte. Although the electrode exhibited good rate capability, the electrode experienced a considerable loss of capacitance upon continuous cycling and only retained 76 % after 500 cycles. The declining capacitance was probably due to slow oxidation of $Co(OH)_2$ to CoOOH and "peeling off" of the active materials from the current collector. In another report, Kong *et al.* investigated the effects of deposition conditions, type of substrates, and concentration of cobalt precursor solution on the performance of electrodeposited α-$Co(OH)_2$ nanosheets.[207] $Co(OH)_2$ film deposited for 100 s was found to exhibit the highest specific capacitance. Beyond deposition time of 100 s, the specific capacitance decreased due to the blockage of pores by nanosheets grown on top of the surface. For the cathodic deposition potential, α-$Co(OH)_2$ film prepared at -1 V exhibited the highest specific capacitance. When a more positive potential

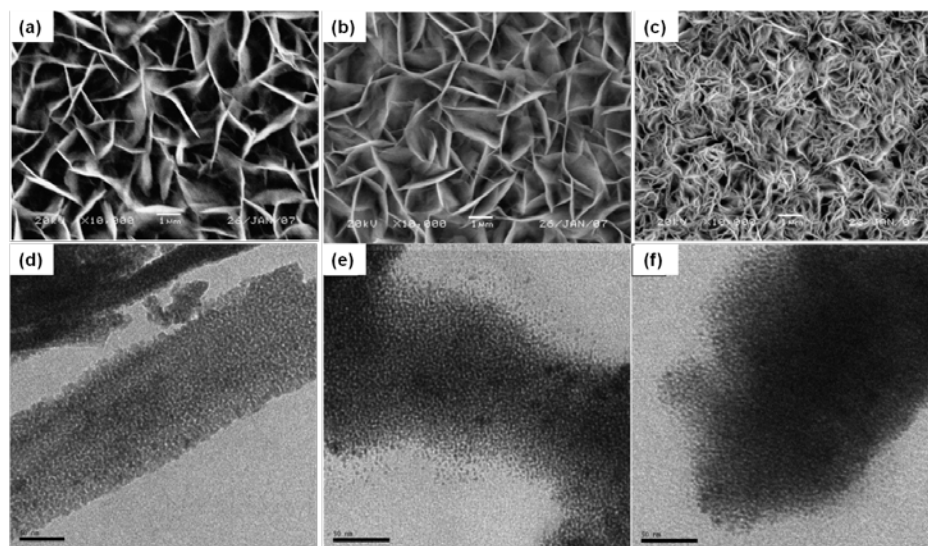**Fig. 5** SEM and TEM images of H_I-e $Co(OH)_2$ nanosheets deposited at various deposition potentials at 50 °C. (a and d): -0.65 V, (b and e): -0.75 V and (c and f): -0.85 V. Adapted with permission from Ref. [202], ©2008 Elsevier.
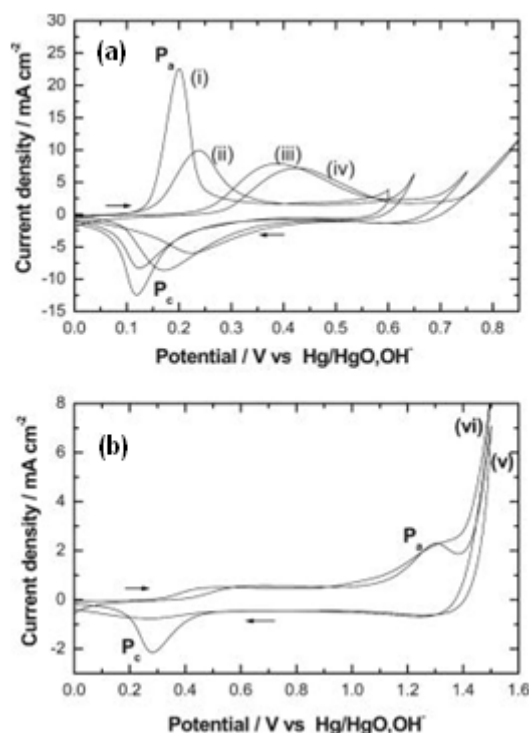

Fig. 6 CV curves of $Co(OH)_2$ electrode in different electrolytes and concentrations, (i) 1.0 M NaOH, (ii) 0.5 M NaOH, (iii) 0.1 M NaOH, (iv) 0.05 M NaOH, (v) 1.0 M Na_2SO_4 and (vi) 0.1 M Na_2SO_4. Reproduced with permission from Ref. [203], ©2008 The Electrochemical Society.

was applied, the deposition rate became slow and the film structure was compact with smaller pores that may not be favorable for electrolyte access.

In the contrary, when the applied potential became more negative, the growth of crystal was too fast and films with lower specific capacitance were obtained. In addition, it was shown that the capacitance of α-$Co(OH)_2$ deposited on Ni foam was about 2 times higher than that on planar Ni plate. CV curve of the α-$Co(OH)_2$ film deposited on Ni foam consisted of two pairs of redox peaks whereas that deposited on Ni plate only consisted of one pair of redox peaks. The additional pair of redox peaks in the former was probably due to the highly distributed active materials and more reactive sites of α-$Co(OH)_2$ on three-dimensionally structured Ni foam.

In the absence of a hard template, most $Co(OH)_2$ prepared by cathodic deposition appear in a flake-like or sheet-like morphology due to intrinsic crystallographic preference. Hoshino and co-workers presented a different approach to prepare cobalt compound nanowires (CCNW) by potentiostatic electroreduction from electrolyte containing cobalt ammine complex, $[Co(NH_3)_6]Cl_3$ in N_2 atmosphere.[208, 209] After the first potential sweep, the CV curve in the potential window of 0-0.55 V showed a redox pair closely similar in peak shapes and positions as the reported CV curve of mesoporous $Co(OH)_2$ film. Furthermore, TOF-SIMS, XPS, EDX and XRD analysis revealed that the CCNW surface was covered with $Co(OH)_2$ while the CCNW bulk composed of cobalt metal. A maximum specific capacitance of 420 F/g was achieved by the CCNW electrode in 0.1 M LiOH.

By using porous anodic alumina (PAA) and lyotropic liquid

crystal (LLC) as dual-template, α-Co(OH)$_2$ mesoporous nanowires on PAA/Ti/Si substrates were prepared via cathodic potentiostatic electrodeposition (Figure 7).[210] The composition of LLC template was similar to that used previously by Li *et al.*[200]. Low angle XRD pattern of the as-synthesized α-Co(OH)$_2$ nanowires exhibited a strong reflection peak at 2θ = 1.24°, corresponding to d$_{100}$ plane of the P6mm space group with d-spacing of 71.2 Å and pore-to-pore distance of 8.2 nm. Interestingly, the templated nanowires still obeyed the rules of layered structure and sheet packing. Under HRTEM, the ordered hexagonal mesopores with cylindrical channels of about 3.6 nm in diameter, pore-to-pore distance of about 7.9 nm and pore wall thickness of 4.3 nm were observed. The specific capacitances of the electrode were 993, 922, 873 and 810 F/g at current densities of 1, 5, 10 and 20 A/g, respectively. Notably, when the current density increased from 1 to 20 A/g, the electrode was able to retain 81.5 % of the initial specific capacitance.
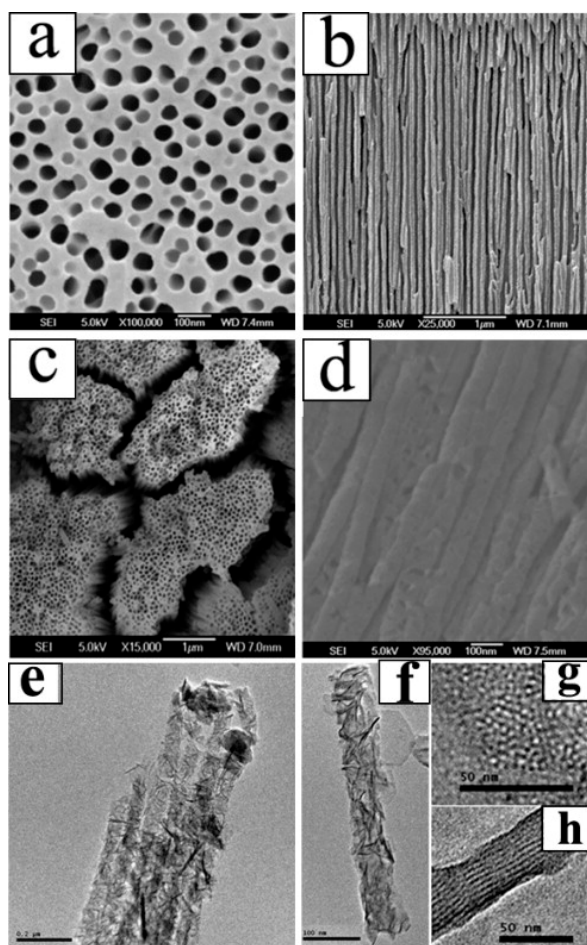

Fig. 7 SEM images of PAA templates (end view (a) and cross view (b)) and mesoporous Co(OH)$_2$ nanowire (end view (c) and side view (d)). TEM images of mesoporous Co(OH)$_2$ nanowires (e and f). (g) and (h) are the end view and side view of the pores respectively. Reproduced with permission from Ref. [210], ©2012 Elsevier.

5   Cobalt oxyhydroxide (CoOOH) electrodes[211-214]

CoOOH is well-known as a highly conductive material with conductivity of 5 S/cm and a highly electroactive material.[211-213]

Layered hydroxide cobalt acetate (LHCA) nanosheets were first prepared by a CBD procedure, the as-synthesized LHCA films were then converted to CoOOH by alkaline treatment.[211] These CoOOH nanoflakes possessed surface area of about 100 m^2/g and porosity of 65 %. At 10 mV/s, the specific capacitance of the CoOOH electrode was 200 F/g, which remained at 79.1 % and 63.6 % when the scan rates increased to 250 and 500 mV/s, respectively. The excellent rate capability was due to the high conductive nature of CoOOH as well as micro/nanometer scaled morphology. Besides, electrodeposition was also applied to prepare CoOOH nanoflakes thin film on stainless steel and a specific capacitance of 449 F/g was achieved by the electrode.[214] Capacitance loss of 44 % was observed after 10000 cycles due to surface contamination or loss of active material from the substrate.

6.   Cobalt sulfide (Co$_x$S$_y$) electrodes[215-223]

The electrochemical capacitance properties of amorphous cobalt sulfide was first reported by Li's group in 2007.[215] Based on CV curves of the electrode in neutral and alkaline electrolytes, the mechanism of cobalt sulfide redox processes was proposed to be similar with Co(OH)$_2$ in alkaline electrolyte. The highest specific capacitance obtained was 475 F/g at 5 mA/cm^2 and the capacitance retained at 369 F/g (77.6 %) when current density was increased to 50 mA/cm^2. Different self-assembled CoS nanostructures were synthesized via a L-cysteine assisted hydrothermal route.[216] Capacitance of CoS nanowires (508 F/g at 2.5 mA/cm^2) was higher than CoS spheres, possibly due to a looser structure and larger specific surface area. EIS analysis further indicated that CoS nanowires exhibited lower Faradaic reaction and diffusion resistances. While the prepared CoS electrodes[215-217] exhibited good high rate capability, the cycling stability was not satisfactory with considerable capacitance loss of 9-23 % after small cycling numbers of 100 to 500 cycles. It is clear that further investigations to understand the capacitance loss are required.

Substantial improvement in cycling life of cobalt sulfide electrode was achieved by Wang *et al.*[218] In their studies, flower-like CoS$_{1.097}$ hierarchical structures were synthesized by solvothermal method. The CoS$_{1.097}$ nanostructures exhibited high specific capacitance of 555 F/g at 5 mA/cm^2 and good rate capability to retain 86 % of the specific capacitance (464 F/g) when current density increased to 100 mA/cm^2. The capacitance retention after continuous 2500 cycles was about 98 %, demonstrating good electrochemical stability of the electrode.

Further insights on the pseudocapacitive charge-storage mechanism of amorphous CoS$_x$ nanoparticles was revealed by Zhang's group.[219] The amorphous CoS$_x$ nanoparticles (Figure 8a) were prepared by interfacial reaction of aqueous Co(OOCCH$_3$)$_2$ solution and CS under hydrothermal condition. The electrochemical capacitive performance of the as-prepared CoS$_x$ was poor (Figure 8c). However, after continuous 240 CV cycles, capacitance was enhanced significantly with a totally different electrochemical storage mechanism and suggested a new phase formed electrochemically. A significant change in the internal resistance of the electrode was observed before (2.34 Ω) and after (0.78 Ω) CV cycling. At the 240th CV cycle, two pairs of redox peaks were observed in the CV curves. More importantly, the CV

shape resembled the reported $Co(OH)_2$ phase in the KOH electrolyte. FTIR analysis demonstrated the existence of Co-O stretching mode, further supporting the $Co(OH)_2$ phase formation during the CV cycles. Interestingly, TEM images showed the transformation of morphology from CoS_x nanoparticles (Figure 8a) to $Co(OH)_2$ nanowhiskers (Figure 8b). Specific capacitances for $Co(OH)_2$ nanowhiskers of 910 F/g and 651 F/g could be obtained at current densities of 0.4 A/g and 40 A/g, respectively. Similar electrochemically induced phase transformation of NiS to $Ni(OH)_2$ in alkaline electrolyte was observed by the same group.[220] However, it is unclear at present stage whether this phenomenon can be generalized to other cobalt sulfide electrode materials. This calls for further fundamental studies to examine the electrochemical events of cobalt sulfide electrodes.
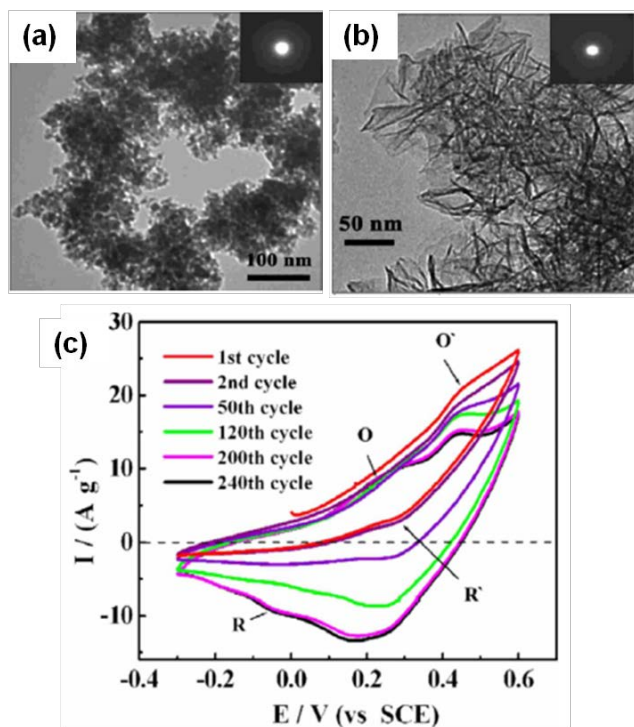

Fig. 8 TEM images of (a) as-synthesized CoS_x nanoparticles and (b) $Co(OH)_2$ nanowhiskers after 240th CV cycles, (c) CV curves of the CoS_x electrode at different CV cycles. Adapted with permission from Ref.[219], ©2009 The Electrochemical Society.

Lou's group synthesized microsized CoS_2 ellipsoids with tube-like cavities by thermal decomposition and sulfidation of a ellipsoidal cobalt carbonate precursor in a gas flow (10 % H_2S: 90 % N_2).[221] The original cobalt carbonate ellipsoids showed dense solid texture without pores. After thermal sulfidation, CoS_2 ellipsoids presented unique tube-like cavities oriented from the centre to the surface with openings on both ends of the ellipsoids. The growth of the cavities, as postulated by the authors, was due to the different reactivity of H_2S gas on different parts of the surface. The specific capacitances of the CoS_2 electrode were 1040, 980, 965, 750 and 224 F/g at 0.5, 1, 2.5, 5 and 10 A/g, respectively. It can be seen that the electrode showed good rate capability to retain 72.1 % of the highest capacitance when the current density increased to 5 A/g, comparable to other reported CoS electrodes discussed earlier.[215-217, 219, 222] However, the capacitance dropped dramatically when the current density was

further increased to 10 A/g. Similar to most reported CoS electrodes,[215-217] the CoS_2 electrode also suffered from detrimental cycling stability. After 1000 cycles, only 66 and 44 % of the initial specific capacitance can be retained at 5 and 2.5 A/g.

Electrodeposition is a facile way to prepare CoS nanostructured thin film directly on a current collector. Uniform CoS nanosheets were cathodically electrodeposited on Ni foam. The specific capacitance was reported as 1471 F/g at 4 A/g and able to retain 89% of the value when the current density increased to 40 A/g.[223]

7. Cobalt based layered double hydroxides (LDHs)[224, 225]

Layered double hydroxides (LDHs) represent a unique class of ionic lamellar compounds, which consist of positively charged layers with a hydrated interlayer region containing charge balancing anions[224, 225]. A general formula for LDHs is written as $[M^{2+}_{1-x}M^{3+}_x(OH)_2][A^{n-}]_{x/n}.yH_2O$, where M^{2+} is a divalent cation e.g. Mg^{2+}, Zn^{2+}, Ni^{2+}, Co^{2+}; whereas M^{3+} is a trivalent cation e.g. Al^{3+}, Fe^{3+}, Mn^{3+}. The identities of M^{2+} and M^{3+}, the interlayer anions A^{n-} (e.g. Cl^-, SO_4^{2-}, CO_3^{2-}) and the value of the stoichiometric coefficient x (normally 0.2-0.4) can be varied and tailored, providing an enormous class of isostructural materials.

A series of Co/Ni-Al LDHs with different ratio of Co to Ni prepared via co-precipitation method was reported by Zhang and colleagues in 2004[226]. It was found that Ni/Co mole ratio of 4:6 was the optimum composition to yield the highest specific capacitance of 960 F/g, as compared to 140 F/g of Ni-Al LDH. With the incorporation of TiO_2 nanotubes as a dispersing agent for the Co/Ni-Al LDH, enhanced electrical properties improved the specific capacitance to 1053 F/g[227]. Afterward, the group extended the co-precipitation scheme in sodium benzoate to obtain benzoate-intercalated Co-Al LDHs and eventually carbon-inserted double oxides[228]. The specific capacitances of the three different samples were between 190-213 F/g with excellent high rate capability.

Subsequently, the same authors investigated the electrochemical capacitive behavior of Co-Al LDH in 1 M LiOH electrolyte[229]. A specific capacitance of 322 F/g at 0.5 A/g was obtained for Co-Al LDH in 1 M LiOH. It was further found that Co-Al LDH exhibited two independent electrochemical reactions in LiOH, involving the simultaneous intercalation of lithium cation and hydroxyl group, which was different from the mechanisms in NaOH and KOH. Nevertheless, the process of Li intercalation/ de-intercalation was not stable. The initial capacitance of 268 F/g was decreasing with cycling uptill 800 cycles. The capacitance remained stable from 850 to 1000 cycle due to a complete Li ion insertion into the Co-Al LDH and the formation of a new phase.

Zhang *et al.* also attempted to improve the capacitance performance of Co-Al LDHs by investigating the effect of electrolyte[230]. By adding hexacyanoferrate into KOH electrolyte, the electrochemical redox reactions of $Fe(CN)_6^{3-}/Fe(CN)_6^{4-}$ took place in the electrode surface layer and in the electrolyte. This resulted in the increase of the whole reaction rate. Besides Co-Al LDHs, Zhang's group prepared Co-In LDHs and Co-Cr LDHs via precipitation or precipitation-hydrothermal methods to investigate the effects of different trivalent cations on the electrochemical

properties[231]. Basically, the specific capacitances of Co-Al LDHs, Co-In LDHs and Co-Cr-LDHs obtained at 1 A/g were 447, 159, 78 F/g, respectively.

On the other hand, preparation of Co-Al LDHs via similar co-precipication method was reported by Duan *et al.*[232] Effects of post-thermal treatment on their microstructures, surface area, crystallinity and electrochemical behavior were investigated. Under an optimum thermal treatment (160 °C), the sample exhibited high specific capacitance of 684 F/g. However, the cycling stability is less satisfactory with 20 % loss after 1000 cycles. Hu *et al.* synthesized Co-Ni LDHs by co-precipitation using polyethylene glycol as the structure directing agent[233]. Specific capacitance of 1809 F/g was the maximum for $Co_{0.41}Ni_{0.59}$ LDHs, compared to 638 F/g and 1399 F/g for $Co(OH)_2$ and $Ni(OH)_2$, respectively.

Yang and co-workers fabricated a highly oriented and densely packed Co-Al LDHs nanosheets thin film electrode by drying a tranparent colloidal Co-Al LDHs nanosheets suspension on a pretreated ITO glass plate[234]. Electrochemical studies revealed that this electrode presented high specific and volumetric capacitances (667 F/g and 2000 F/cm^3, respectively). Several structural features such as open framework and highy exposed surface sites of the nanosheets, close contact between the Co-Al LDHs nanosheets thin film and ITO current collector were responsible for the high capacitance, high rate capability and electrochemical stability. Further studies showed that partial isomorphic substitution of Co^{2+} by Al^{3+} helped retain the original layered structure during the redox reaction, favouring the oxidation of Co to higher oxidation state, as well as shifting the oxygen evolution potential to a more positive value.[235] LDHs with a Co/Al molar ratio of 3:1 presented the largest specific capacitance of 833 F/g (2500 F/cm^3).

With a co-precipitation method, Zn-Co LDH with a composition of $[Zn^{2+}_{0.50}Co^{2+}_{0.28}Co^{3+}_{0.22}(OH)_2][0.22NO_3^-]\cdot0.55H_2O$ was synthesized[236]. The restacked assembly of exfoliated LDH nanosheets was coated on an ITO substrate and used for ECs. The specific capacitance was measured to be ~160-170 F/g. The obtained capacitance is considerably lower than the other LDHs constituted mainly of Ni and Co, probably due to the presence of less pseudocapacitive Zn^{2+}. With two-step microwave-assisted hydrothermal techniques, a series of Co-Ni LDHs nanocones with tuneable Co/Ni content, interlayer distance and aspect ratio were prepared by Liu and co-workers as presented in Figure 9a-f.[237] From the charge-discharge curves, the specific capacitances of $Co_{1-x}Ni_x$ hydroxide nanocones approximated 490, 1100, 1580, 1400, 740 F/g for Co, $Co_{0.75}$-$Ni_{0.25}$, $Co_{0.5}$-$Ni_{0.5}$, $Co_{0.25}$-$Ni_{0.75}$ and Ni hydroxides nanocones, respectively (Figure 9h). Obviously, bimetallic hydroxides were better than those of monometallic hydroxides.

Alternatively, different LDHs such as Co-Ni LDHs, Co-Al LDHs and Co-Ni-Al LDHs in the form of nanosheets can be prepared.[238-242] Studies of various molar ratio of Co/Ni in Co-Ni LDHs demonstrated that $Co_{0.72}Ni_{0.28}$ LDHs had the highest specific capacitance of 2104 F/g.[238] On the other hand, isomorphic substitution of aluminum into pure $Co(OH)_2$ changed the CV curve dramatically to rectangular shape even at a low level of 8 % substitution.[239] Electrodeposited CoNiAl LDHs presented a distinctly different charge-discharge behavior than

their CoNi and CoAl LDHs counterparts.[240] A nearly ideal and symmetric charge-discharge curve was observed, mainly due to the high conductive nature of the electrode. The highest specific capacitance of 1263 F/g was obtained for $Co_{0.50}Ni_{0.21}Al_{0.20}$ LDHs.
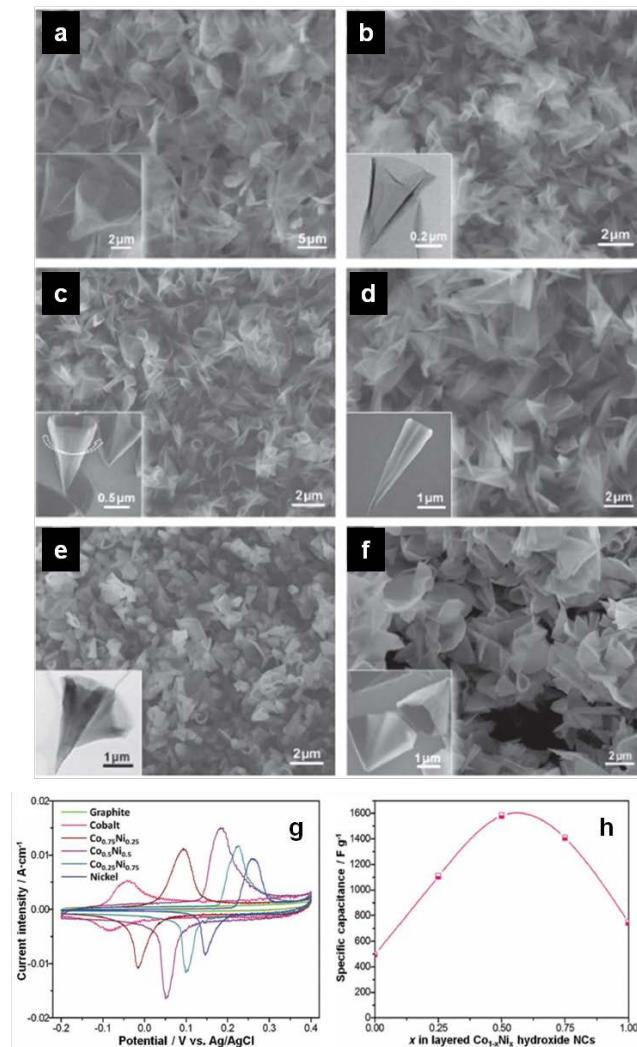

Fig. 9 SEM images of LDHs nanocones (NCs) with tunable transition metals content and ratio: (a) Ni, (b) $Co_{0.25}$-$Ni_{0.75}$, (c) $Co_{0.5}$-$Ni_{0.5}$, (d) $Co_{0.75}$-$Ni_{0.25}$, (e) $Co_{0.5}$-$Cu_{0.5}$, (f) $Co_{0.5}$-$Zn_{0.5}$; (g) CV curves of Co-Ni LDHs NCs with different composition of Co and Ni depositied on graphite substrates and (h) specific capacitance of NCs with different Co-Ni composition. Adapted with permission from Ref. [237], ©2012 Wiley-VCH.

Most recently, Leroux's group revisited monometallic $Co^{II}Co^{III}$-CO_3 LDH prepared by topochemical oxidative reaction (TOR) of β-$Co(OH)_2$.[243] The chemical composition analysed by X-ray Photoelectron Spectroscopy (for surface) and iodometric titration (for bulk) revealed that only 1/6 of the Co^{II} sites within the hydroxide layers are oxidized to Co^{III} using TOR. Based on the quantification of electroactive Co^{II} cations involved in the electro-oxidation process by CV, the obtained values are 28% for monometallic $Co^{II}Co^{III}$-CO_3 LDH and only 10% for bimetallic Co_2Al-CO_3 LDH. At a current density of 0.5 A/g, $Co^{II}Co^{III}$-CO_3 LDH exhibits specific capacitance of 1490 F/g, much higher than 760 F/g possessed by Co_2Al-CO_3 LDH.

8.   Cobalt-based mixed and ternary oxides/sulfides

8.1   Cobalt-nickel oxide and nickel cobaltite electrodes

Nickel cobaltite ($NiCo_2O_4$) has been reported to possess at least two orders of magnitude higher electronic conductivity than nickel oxides and cobalt oxides. This property is particularly important for high rate charge-discharging.

8.1.1   Electrodeposition[244-248]

Co-Ni oxides were deposited on graphite and FTO substrates by anodic potentiostatic electrodeposition.[244, 245] The specific capacitances of the $(CoNi)(OH)_2.nH_2O$ were 760, 700, 660 F/g at 4, 25, 50 °C respectively. By using an anodic potentiodynamic electrodeposition method, Gupta and colleagues synthesized nanostructured cauliflower-shape Co-Ni/Co-Ni oxides composites on stainless steel.[246] XRD patterns showed the presence of Co, Ni, Co_3O_4 and NiO. A specific capacitance of 331 F/g (areal capacitance of 46 mF/cm^2) was obtained for the composite electrode.

Li and colleagues applied galvanostatic electrolysis method to fabricate $Co(OH)_2/Ni(OH)_2$.[247] Upon heat treatment, mesoporous $Co_3O_4/Ni(OH)_2$ nanosheet networks (NNs) were formed from the precursor. The presence of Ni was confirmed by EDS, giving ratio of Co/Ni of about 2. The specific capacitance of the $Co(OH)_2/Ni(OH)_2$ was 823 F/g. However, the specific capacitance dropped dramatically to 520 F/g after 500 cycles. The reason of such degradation was probably due to the transformation of metastable α-$Co(OH)_2$ to β-$Co(OH)_2$. In order to improve the cycling stability, $Co(OH)_2/Ni(OH)_2$ was thermally treated at 200, 300 and 400 °C (denoted NiCoO-200, NiCoO-300 and NiCoO-400). At 200 °C, Co_3O_4 phase was observed from XRD pattern. When the annealing temperatures were 300 °C and 400 °C, the XRD patterns could be indexed to $NiCo_2O_4$. Among the samples, the NiCoO-200 possessed the highest BET surface area of about 80.3 m^2/g, compared to as-synthesized sample (10.8 m^2/g), NiCoO-300 (59.1 m^2/g) and NiCoO-400 (37.7 m^2/g). NiCoO-200 mesoporous NNs displayed a specific capacitance of 684 F/g, lower than the value of as-synthesized $Co(OH)_2/Ni(OH)_2$, but higher than NiCoO-300 (282 F/g) and NiCoO-400 (136 F/g) mesoporous NNs. Moreover, NiCoO-200 managed to solve the cycling instability of the as-synthesized $Co(OH)_2/Ni(OH)_2$. The specific capacitance of NiCoO-200 was eventually maintained at 93.4 % of the maximum value after 500 cycles.

8.1.2   Sol-gel synthesis[249-253]

Hu *et al.*[249] devised an innovative epoxide-driven sol-gel process to prepare nickel cobaltite ($NiCo_2O_4$) aerogels. Structural parameters of the samples derived from N_2-adsorption/desorption isotherms are presented in Table 2. Upon post-calcination of the $NiCo_2O_4$ aerogels at 200 °C, larger pore volumes and pore size attributed to the removal of physisorbed moisture and solvent were observed. However, when the calcination temperature increased to 300 °C, a composition change from $NiCo_2O_4$ to Co_3O_4 took place with significant increase of grain size from 6 to 22.4 nm. In general, post-annealing of $NiCo_2O_4$ at 200 °C presented an optimum combination of composition, crystallinity, specific surface area, pore volume and pore size, achieving a specific capacitance of 719 F/g. Cycling study showed that 500 cycles were needed to fully activate the sample, thus achieving

the highest specific capacitance of 1400 F/g. After 2000 cycles, the specific capacitance was maintained at 91 % of the maximum value.

Table 2 Surface area, porosities and specific capacitances of as-prepared $NiCo_2O_4$ aerogels (denoted as Ni-Co-O) and $NiCo_2O_4$ aerogels after different calcination temperatures (200°C and 300 °C for Ni-Co-O-200 and Ni-Co-O-300 respectively). Reproduced with permission from Ref [249], ©2010 Wiley-VCH.

	BET specific surface area (m^2/g)	BJH pore volume (cc/g)	NLDFT pore diameter (nM)	Specific capacitance (F/g)
Ni-Co-O	123	0.114	2.6	634
Ni-Co-O-200	122	0.137	3.5	719
Ni-Co-O-300	43	0.1	3.5	420

Gong and co-workers prepared a series of Ni-Co oxides with different Ni/Co ratios by a sol-gel method.[250] With increasing Co concentration, the oxide phase changed from NiO crystal dominant structure to Co_3O_4 dominant structure. In the CV curves of three Ni-Co oxides (Ni/Co ratio of 1:1, 1:2 and 1:4), the redox peaks were broadened with an increase in Co, and both anodic and cathodic peaks shift to the negative direction. The calculated specific capacitances were 1289, 1410, 1539, 1060 and 361 F/g for $Ni(OH)_2/NiO$, Ni-Co oxide (1:1), Ni-Co oxide (1:2), Ni-Co oxide (1:4) and Co_3O_4, respectively. Comparatively, Ni-Co oxide (1:2) possesses larger pore width and cumulative pore volume, which allow better ion penetration to react with the active material more easily. Similar to Hu's work,[249] Gong observed an increase of capacitance at initial cycling study (240 cycles). Unfortunately, the capacitance retention after 2000 cycles was only 47 % due to peeling off of the active materials from the current collector.

By tuning the experimental parameters of a sol-gel process, Chen *et al.* prepared $NiCo_2O_4$ crystals with distinct morphologies.[251] With a fairly high mass loading (5.6 mg/cm^2) the specific capacitances of coral-like porous $NiCo_2O_4$ crystals, $NiCo_2O_4$ nanoparticles and submicron-sized $NiCo_2O_4$ were found to be 103, 188 and 217 F/g, respectively. The submicron-sized $NiCo_2O_4$ exhibited an excellent rate capability, retaining 92.6 and 86.6 % of highest capacitance when current densities increased to 10 mA/cm^2 and 20 mA/cm^2, respectively. Multi-component $NiO/NiCo_2O4/Co_3O_4$ synergistic composite with high specific surface and mesoporous structure was fabricated by a sol−gel process.[252] The composite exhibits high specific capacitance (1717 F/g), enhanced rate capability and excellent cycling stability.

8.1.3   Chemical precipitation[254-260]

Ni-Co oxide was also prepared via co-precipitation using Ni-Co carbonate as the precursor.[254] The specific capacitances of Ni-Co oxide (molar ratio 1:1) calcined at 300, 350, 400, and 450 °C were ~272, ~287, ~180 and ~124 F/g, respectively. A lower capacitance for product calcined at 300 °C as compared to that calcined to 350 °C could be attributed to the incomplete decomposition of precursor. Meanwhile, when calcination temperature was increased to 400 °C, the nanowire morphology changed to nanocolumn, leading to a decrease in specific surface area. The Ni-Co oxide (1:1) presented larger capacitance than those of pure NiO and Co_3O_4 electrodes. According to EIS analysis, the Ni-Co oxide (1:1) had the smallest charge transfer

resistance and internal resistance among other electrodes with Ni:Co ratio of 9:1, 7:3, 3:7 and 1:9.

$Co_{0.56}Ni_{0.44}$ oxide nanoflakes, $NiCo_2O_4$ spinel oxide nanostructures, $Ni_{0.37}Co_{0.63}(OH)_2$ and $Ni(OH)_2$-$Co(OH)_2$ composites were synthesized by chemical precipitation.[255-258] The BET specific surface area of the $Co_{0.56}Ni_{0.44}$ oxide nanoflakes was 110 m^2/g, while pore size distribution was 2-7 nm with average pore diameter of 5.9 nm. The specific capacitance of the $Co_{0.56}Ni_{0.44}$ oxide nanoflakes was 1227 F/g. A comparative studies of different samples showed that the optimum product possessed lower specific surface area and less pore volume, yet demonstrated the highest capacitance. Such improvement was attributed to the much higher electronic conductivity of the optimum sample.[235] $Ni(OH)_2$-$Co(OH)_2$ (2193 F/g) not only exhibited higher maximum specific capacitance than $Ni(OH)_2$ (1914 F/g), the rate capability of $Ni(OH)_2$-$Co(OH)_2$ is better, retaining 63.3 % of its highest specific capacitance when the current density increased ten times, as compared to 45.7 % for $Ni(OH)_2$.[258]

Hierarchical $NiCo_2O_4$ porous nanowires (constructed by nanoparticle aggregates) and ultralayered mesoporous nanowires (constructed by nanosheets) were obtained.[259, 260] The specific surface area of the porous nanowires was 202.2 m^2/g after annealing at 250 °C and decreased significantly to 62.1 m^2/g at calcination temperature of 400 °C.[256] The BJH pore size distribution curve of the sample annealed at 250 °C was found to show a sharp peak at ~2.4 nm and a wide peak at ~34.0 nm. The pore volume of the sample was ~1.14 cm^3/g. The maximum specific capacitance of the electrode was 743 F/g at 1 A/g and this was retained at 78.6 % (584 F/g) when the current density increased to 40 A/g.[256]

8.1.4 Hydro/solvothermal synthesis[261-269]

Exploiting hydrothermal method, $NiCo_2O_4$ nanowires self-assembling into microspheres were successfully prepared.[261] After annealing of the precursor, distinct mesopores on the nanowires surface were observed in the TEM images and further confirmed by Type IV N_2 adsorption-desorption isotherms. The BET specific surface areas of Ni-Co-O-1 ($NiCo_2O_4$ with starting Ni/Co molar ratio of 1:1) and Ni-Co-O-2 (starting Ni/Co molar ratio of 2:1) were 84.7 and 99.6 m^2/g respectively. The average mesopore sizes in Ni-Co-O-1 and Ni-Co-O-2 were 13.0 and 11.1 nm. The calculated specific capacitances at 1 A/g for Ni-Co-O-1 and Ni-Co-O-2 were 722 and 760 F/g, respectively. When the current density increased to 20 A/g, the capacitances of Ni-Co-O-1 and Ni-Co-O-2 were retained at 79 % and 70 %, revealing remarkable rate capability of the $NiCo_2O_4$ nanowires. After 3000 cycles, the capacitances of Ni-Co-O-1 and Ni-Co-O-2 were retained at 80 % and 81 % respectively.

Xiao and Yang[262] reported a detailed account on kinetic control and mechanistic studies of the formation of sea-urchin like Ni-Co carbonate hydroxide by hydrothermal process and its thermal conversion to porous $NiCo_2O_4$ spinel for pseudocapacitors. Upon calcination at 300 °C for 3 h, the metallic carbonate hydroxides were decomposed to desired products of Co_3O_4, NiO and $NiCo_2O_4$ phases (Figure 10d, e), and nearly preserving the original morphologies (Figure 10a-c). As expected, the smooth surfaces of carbonate hydroxides became rough and porous after thermal decomposition, due to the escape of small gas molecules. Basically, all the adsorption isotherms could be categorized as Type IV. The hysteresis loop of the Co_3O_4 samples could be categorized as Type H1, associated with a narrow pore size distribution (average pore diameter: 16.5 nm). Meanwhile, $NiCo_2O_4$ samples exhibited smaller mean pore size (average pore diameter: 5 nm). The hysteresis loop of the NiO samples is attributable to Type H3, featuring slit-shaped pores. The BET specific surface areas of Co_3O_4, $NiCo_2O_4$, and NiO were 31.3, 198.9, 186.4 m^2/g, respectively. Figure 11a presents CV curves of the samples. Comparatively, the CV curve of $NiCo_2O_4$ electrode exhibits an obviously larger CV integral area, as well as wider separated pair of redox couple than Co_3O_4 and NiO electrodes. Based on galvanostatic charge-discharge curves, the specific capacitances for $NiCo_2O_4$, Co_3O_4 and NiO electrodes were 658, 60, 194 F/g at current density of 1 A/g. When the current density increased to 10 A/g, the specific capacitances for $NiCo_2O_4$, Co_3O_4 and NiO electrodes remained at 80.5 % (530 F/g), 51.7 % (31 F/g) and 78.4 % (152 F/g), respectively. In addition to higher specific capacitance due to the richer redox reactions, $NiCo_2O_4$ electrode is superior in terms of high rate capability, mainly contributed by the much higher electrical conductivity as shown by a lower charge transfer resistance (Figure 11c).

When the hydrothermal-synthesized $Ni_{0.5}Co_{1.5}(OH)_2CO_3$ nanowire arrays (NWAs) were immersed in 6 M NaOH for 6 to 18h, small and thin nanoplatelets formed on the surface of the NWAs. The hierarchical nanowire@nanoplatelet arrays (NWPAs) showed both high areal capacitance and specific capacitance (9.59 F/cm^2 or 928.4 F/g at 5 mA/cm^2), at least 7 times larger than the pristine NWAs. In addition, the NWPAs exhibited good rate capability, retaining 81% of the highest capacitance at high current density of 50 mA/cm^2.[263]

Su and co-workers investigated the electrochemical performances of $Co(OH)_2/Ni(OH)_2$ composites specifically in LiOH solution,[264] extending their previous attempt on the use of LiOH electrolyte for Co-Al LDH[229] The $Ni(OH)_2$ and $Co(OH)_2$ were physically mixed to form a composite electrode.[265] Compared to the pure $Ni(OH)_2$ and $Co(OH)_2$ electrodes, $Co(OH)_2/Ni(OH)_2$ composite with a weight ratio of 3:2 lowered the IR drops of galvanostatic discharge curves by reducing the charge transfer resistance of the electrode. For the $Co(OH)_2/Ni(OH)_2$ composite, weight ratio of 3:2 was the optimum mixture that exhibited a specific capacitance in between the two pure phase electrodes. Importantly, the pure $Ni(OH)_2$ and $Co(OH)_2$ electrodes suffered from poor cycling stability. In contrast, all composites electrodes experienced improvement in cycling stability.

8.1.5 Chemical bath deposition[270-273]

Ahn's group synthesized $NiCo_2O_4$ nanorods and nanoflakes directly on ITO and stainless steels substrates by chemical bath deposition followed by calcination at 300 °C[270, 271]. Comparatively, the BET surface area of the $NiCo_2O_4$ nanorods and nanoflakes were 196 and 35 m^2/g, respectively. As expected from the higher surface area and porosity, $NiCo_2O_4$ nanorods (490 F/g) exhibited higher specific capacitance than $NiCo_2O_4$ nanoflakes (330 F/g).

8.1.6 Successive ionic layer adsorption and reaction (SILAR)[274]

Co-Ni mixed hydroxide films were deposited on stainless steel via successive ionic layer adsorption and reaction (SILAR).[274]

The thickness of the film was controlled by tuning the concentration of cationic solution and deposition cycles.
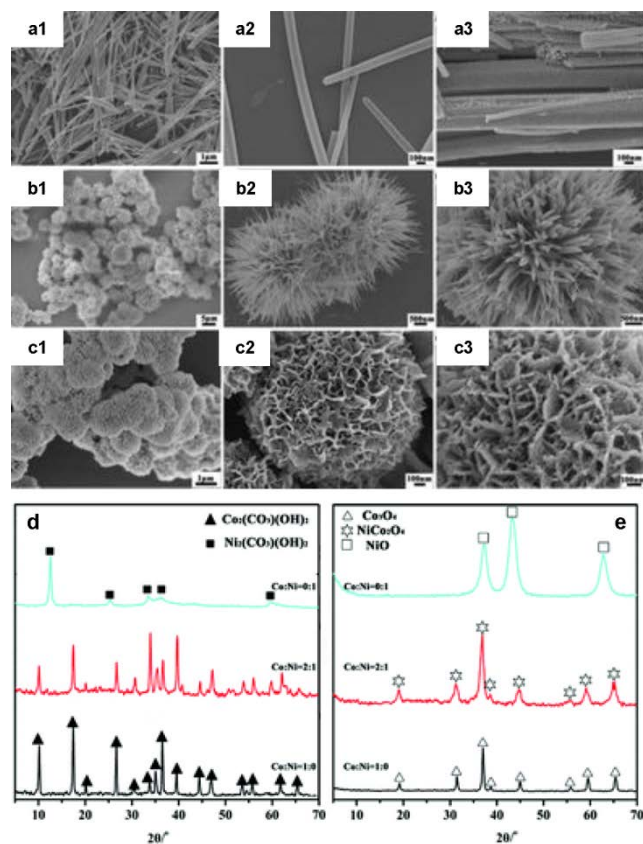

Fig. 10 (a-c) SEM images of metal carbonate hydroxide salts formed at various Co/Ni molar ratios: (a1, a2) Co/Ni = 1:0; (b1, b2) Co/Ni = 2:1; (c1, c2) Co/Ni = 0:1, and the corresponding metal oxides after 300 °C calcination for 3 h: (a3) Co_3O_4 (Co/Ni = 1:0); (b3) $NiCo_2O_4$ (Co/Ni = 2:1); (c3) NiO (Co/Ni = 0:1); XRD patterns of (d) metal carbonate hydroxide salts (Co/Ni = 1:0, 2:1, and 0:1) and (e) the corresponding metal oxides after 300 °C calcination for 3 h. Adapted from Ref. [262].
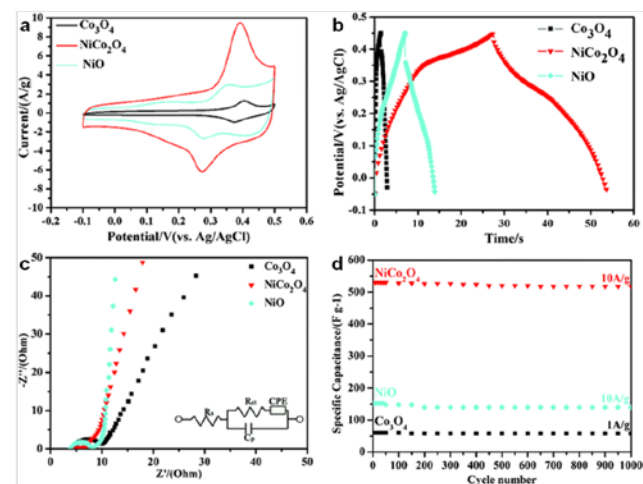

Fig. 11 (a) CV curves at scan rate of 5 mV/s, (b) galvanostatic charge-discharge curves at a charge-discharge current density, (c) Nyquist plot of the EIS and (d) the cycling stability test of 10 A/g of Co_3O_4, $NiCo_2O_4$, and NiO electrodes. Adapted from Ref. [262].

The Co-Ni hydroxide film was constructed by a dense layer of interconnected and agglomerated nanoparticles. On the other hand, cobalt hydroxide and nickel hydroxide films prepared from single cationic solution consisted of smooth grains and spongy nanoflakes, respectively. Hydrophilicity of the Co, Ni and Co-Ni hydroxide films was evaluated by water contact angle and found to be 47°, 32° and 19° respectively. Hydrophilicity is useful for the electrode surface to make intimate contact with aqueous electrolyte. The specific capacitances of the Co, Ni and Co-Ni hydroxide films were 354, 425 and 672 F/g, respectively. The specific capacitance of the Co-Ni hydroxide film was maintained at 57.6 % (387 F/g) when the scan rate increased from 5 to 100 mV/s. Nevertheless, all the three films experienced considerable capacitance loss upon continuous 1000 cycles due to the loss of active materials, probably caused by dissolution and detachment during the early cycles.

8.2 Cobalt-nickel sulfide electrodes[275-282]

Based on the success of nickel cobaltite ($NiCo_2O_4$), Chen *et al.* explored the use of nickel cobalt sulphide ($NiCo_2S_4$) in the application of ECs.[275] Interestingly, they found that $NiCo_2S_4$ shows much lower optical band gap energy and much higher conductivity compared to $NiCo_2O_4$. $NiCo_2S_4$ urchin-like structures were converted from Ni-Co carbonate hydroxide by reacting with Na_2S in a hydrothermal condition. The electrode presented a high specific capacitance of 1149 F/g at 1 A/g, as well as an impressive rate capability to retain 77% of the capacitance at 20 A/g, and 66% of the capacitance at 50 A/g.

8.3 Zinc cobaltite electrodes[283, 284]

The co-precipitated submicron crystalline $ZnCo_2O_4$ particles were mixed with carbon nanofoam and then pasted on stainless steel current collector.[283] A symmetric cell was fabricated by sandwiching the electrodes between a polypropylene separator using 6 M KOH as electrolyte. Based on the two-electrode study, a specific capacitance of 77 F/g was obtained for the composite electrode.

Zinc cobaltite aerogels can also be synthesized through the epoxide-driven sol-gel method.[284] The $ZnCo_2O_4$ samples were prepared in a stoichiometric (1:2) and a non-stoichiometric (1:1) molar ratio. Different gelation agents were used in the synthesis. From the SEM images in Figure 12, it showed that the choice of the epoxide [propylene oxide (P), glycidol (G) or n-butyl glycidyl ether (B)] and solvent [ethanol (E) or 2-propanol (P)] used could affect the morphologies. Table 3 depicts the surface and porosity properties, as well as specific capacitances of as-synthesized $ZnCo_2O_4$ aerogels and their annealed products. Based on the CV curves of the as-prepared and annealed PE (propylene oxide as epoxide and ethanol as solvent) sample, the electrical double layer capacitance was more dominant for the as-prepared than the annealed PE sample. Conversely, the annealed PE sample exhibited more pronounced pseudocapacitance correlated with a sharper redox peak. The specific capacitance of the annealed PE sample was 700 F/g. The relatively higher capacitance than other samples may be attributed to structurally interconnected porous morphology and high specific area. Notably, similar to some other materials prepared by sol-gel method, the annealed $ZnCo_2O_4$ underwent activation and increased capacitance in early cycles, and finally retained 95 % of the specific capacitance after 3000 cycles.
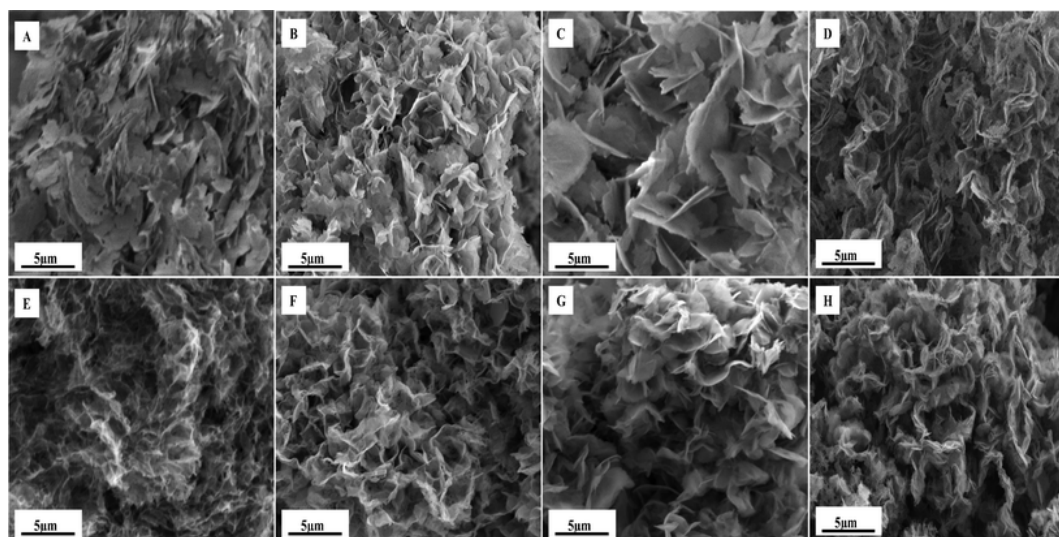
Fig. 12 SEM images of Zn–Co aerogels: A–D) as prepared PE, PP, BE, and BP, respectively. E–H) annealed PE, PP, BE, and BP, respectively. [Note: propylene oxide (P), glycidol (G) or n-butyl glycidyl ether (B), ethanol (E), 2-propanol (P)]. Reproduced from Ref. [284].
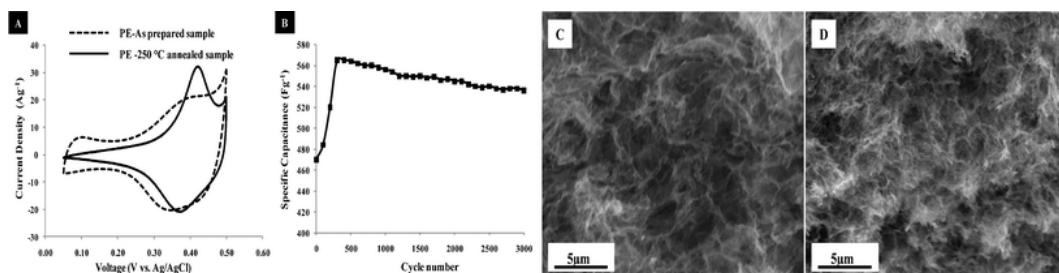

Fig. 13 A) CV curves of as prepared PE and annealed sample in 1 M NaOH with a 25 mV/s scan rate, B) Cycling stability test for the annealed PE sample. C and D) SEM micrographs of sample PE before and after electrochemical stability tests, respectively. Reproduced from Ref. [284].

Table 3 Structural characteristics and specific capacitances of $ZnCo_2O_4$ aerogels as prepared and their analogues annealed at 250 °C (in parentheses). [Note: propylene oxide (P), glycidol (G) or n-butyl glycidyl ether (B), ethanol (E), 2-propanol (P)]. Reproduced with permission from Ref. [284], ©2012 The Royal Society of Chemistry.

Sample	Surface area [m²g⁻¹]	Pore volume [cm³g⁻¹]	Pore radius [nm]	C_m [Fg⁻¹]
PE	251 (241)	0.69 (0.49)	2.58 (2.61)	589 (575)
PP	203 (176)	0.44 (0.28)	2.60 (2.60)	(452)
BE	187 (208)	0.39 (0.39)	2.89 (2.60)	(469)
BP	151 (187)	0.45 (0.42)	2.60 (2.60)	(482)

8.4   Other cobalt-related mixed oxides[285, 286]

Ternary Mn-Ni-Co oxide (MNCO) composites were synthesized by co-precipitation of Mn, Ni and Co salts, followed by thermal decomposition.[285] The composites were composed of Mn_3O_4, NiO and Co_3O_4. The morphology of the as-synthesized materials consisted of microparticles making up of networks of solid rods. These nanostructures increased the solid-electrolyte interfacial area, as well as provided an easier transport path for percolation of the electrolyte through the solid. CV curves of the MNCO and NCO (Ni-Co oxide) electrodes appeared similar, showing that manganese oxide did not participate in the redox process directly. However, the redox current of MNCO electrode is higher than NCO electrode, probably due to the ability of manganese oxide to store electrical charge by simultaneous injection of electrons and

charge-compensating cations into the solid. According to EIS analysis, despite having slightly higher internal resistance, MNCO electrode has a smaller electrochemical reaction resistance and a larger capacitance than that of the NCO electrode. The specific capacitance of the MNCO composite was 1080 F/g, about 270 F/g higher than that of NCO electrode.

9.   Other cobalt compounds

9.1   Co-based metal organic frameworks (Co-MOF)[287]

Zhang's group first utilized Co-MOF as an intermediate to obtain Co_3O_4 superstructures for EC.[287] Later it was revealed by Lee *et al.* that Co-MOF can be utilized directly as an electrode material for EC[288]. The Co-MOF film doctor-bladed onto ITO substrate consisted of mesoporous structure formed by MOF nanoparticles of 50-100 nm. Among various electrolytes i.e. LiOH, KOH, LiCl and KCl, LiOH was found to be the most suitable electrolyte for the Co-MOF film. The Co-MOF film demonstrated a specific capacitance of ~207 F/g at 0.6 A/g. In addition, the cycling stability of the electrode was evaluated for 1000 cycles. The organic-inorganic framework was highly stable in LiOH, LiCl and KCl, but the framework was destroyed in KOH due to its strong alkaline condition. After 1000 cycles in LiOH, the MOF was transformed into fine crystalline structure. The change of morphology was probably due to the continuous deformation-

formation associated with rearrangement of MOF crystal structure during cycling. The MOF film retained 98.5 % of the initial capacitance after 1000 cycles, showing an excellent cycling stability.

9.2   Cobalt carbonate hydroxide[289]

Instead of using Co-Al LDH as electrode materials, Sun and co-workers attempted to convert Co-Al LDH nanosheets to mesoporous cobalt carbonate hydroxide (MPCCH) nanosheets for ECs.[289] The Co-Al LDH film was pink in color and constructed with nanosheets of 0.5-1 μm in length and 50-80 nm in thickness. After immersion in 5 M NaOH solution, the film color turned to dark red. The original three dimensional nanosheets network was preserved, but the individual nanosheet became thinner with thickness of about 10 nm after the alkaline treatment. In addition, small pores of several to tens of nanometers were observed in the alkaline treated cracked nanosheets. Combined analysis by EDS, SEM and TEM demonstrated that etching in the 5 M NaOH led to the dissolution of Al from the Co-Al LDH creating holes and cracks in the nanosheets.

Overall, alkaline treatment thinned the nanosheets, created porosity and increased surface area, leading to a better penetration of electrolytes into the electrodes and shortened the diffusion distance. The specific capacitance of MPCCH at 5 mA/cm^2 was 1075 F/g, much higher than Co-Al LDH (~390 F/g). Furthermore, at very high current density of 50 mA/cm^2, MPCCH retained 72.4 % of its highest capacitance, whereas Co-Al LDH only 56.8 % of its highest capacitance.

9.3   Cobalt phosphate/phosphite[290, 291]

Pang and co-workers synthesized various cobalt phosphate[290] and phosphite[290, 291] nano/microarchitectures as electrodes for ECs. Through chemical precipitation under different formulations, $NH_4CoPO_4.H_2O$ with different morphologies (oblong plate, microplate, microflower, hierarchical architectures) were obtained.[290] Under hydrothermal condition, mixture of cobalt chloride and sodium pyrophosphate yielded cobalt phosphite ($Co_{11}(HPO_3)_8(OH)_6$) microarchitectures assembled with 20-30 μm long nanoribbons.[290, 291] The specific capacitance of the phosphate electrodes was higher than the phosphite electrode. The specific capacitance was varied from 366 to 1143 F/g depending on the morphologies, which may in turn control the surface-interface properties and thus the ion movement and electrolyte accessibility.

10.   Cobalt compounds related hetero-nanostructures[82, 292-309]

Recently, rational synthesis of complex heterostructures becomes an important research trend to seek a breakthrough in electrochemical performance. Basically, there are two approaches in constructing hetero-nanostructures made of two or more nano-components. In the first approach, the first nano-component acts as a nanostructured current collector to allow the deposition of second electroactive nano-component.[292-297] This approach enhances the connection and contact between electroactive materials and nanostructured current collector; maximizes the utilization of electrode materials on the high surface area current collector; provides efficient pathways for rapid charge transport

and eliminates the use of ancillary binders and conducting additives. In the second approach, both components are electroactive materials to be integrated into three dimensional (3D) hierarchical structures. 3D hierarchical nanostructures exhibit high specific surface area, high permeability and more surface active sites as electrode materials in ECs.[82, 298-306]

Fan and co-workers published a series of reports on the construction of heteronanostructures for electrochemical energy storage system by using both approaches mentioned earlier. For the first approach, they prepared an ultrathin $Ni(OH)_2$ nanoflake–ZnO nanowire hybrid array, which demonstrated high specific capacitance, excellent cycling stability and more importantly, high rate capability.[292] Among the various hybrid nanostructures, Co_3O_4 nanowire@ MnO_2 ultrathin nanosheets[298], CoO nanowire@ $Ni(OH)_2$ nanoflakes[299], Co_3O_4 nanowire@ NiO nanoflakes[300] hybrid systems (Figure 14), Co_3O_4 nanowire@ porous $Co(OH)_2$ nanosheets,[301] which modelled after the second approach, were exquisitely fabricated.

For pristine Co_3O_4 nanowire array in LiOH electrolyte, redox peaks that correspond to the reversible reaction of Co^{3+}/Co^{4+} could be clearly seen. For the Co_3O_4 nanowire@ MnO_2 ultrathin nanosheets[298], the hybrid material exhibited CV with an expanded integral area and became approximately rectangular. The change of CV shape due to the presence of MnO_2 suggested additional pseudocapacitance provided by MnO_2. The hybrid did not exhibit fast potential drop from 0.3 V in the discharge curve, in line with the integral area in the CV curve. The discharge areal capacitance of the hybrid was 0.56 F/cm^2 at 11.25 mA/cm^2, which is four times higher than the capacitance of pristine Co_3O_4 nanowire array (0.135 F/cm^2). When the current density increased from 4 to 44.7 mA/cm^2, the areal capacitance maintained at 56 %, which is 10 times higher than the specific capacitance of pristine Co_3O_4 nanowire array. Comparatively, after 5000 cycles, the capacitance loss for Co_3O_4 nanowire@ MnO_2 nanosheets was 2.7 %, while capacitance loss for the pristine Co_3O_4 nanowire array was 17.4 %. The excellent electrochemical performance was attributed to the synergistic contribution from the ultrathin MnO_2 nanosheets, the porous single crystalline Co_3O_4 nanowires and the ordered hierarchical configuration. In addition, the Co_3O_4 nanowire array was grown directly on stainless steel, assuring good mechanical adhesion and electrical connection, avoiding the use of polymer binders and conductive additives that add additional contact resistance and dead mass/volume.

Fan's group prepared porous CoO nanowalls composed of small nanobricks tightly interconnected with ordered porosity of around or below 100 nm on nickel foam (Figure 15a-d).[302] The quasi-aligned CoO nanowalls (mass loading: 4.3 mg/cm^2) exhibited a specific capacitance of 540 F/g and a remarkably high areal capacitance of 2.3 F/cm^2. The CoO electrode displayed excellent cycling stability and was able to retain 95 % of capacitance after 5000 cycles. In order to further boost up the areal capacitance, the CoO porous nanowalls can be further electrodeposited with $Ni(OH)_2$ nanolayers (Figure 16e-g).[302] The deposited $Ni(OH)_2$ nanolayers were selected based on several criteria: to contribute additional specific capacitance, to enlarge the surface area but not to block the electroactive CoO surface and to maintain structural integrity. The optimized $CoO@Ni(OH)_2$ hybrid electrode (~4.84 mg) presented an
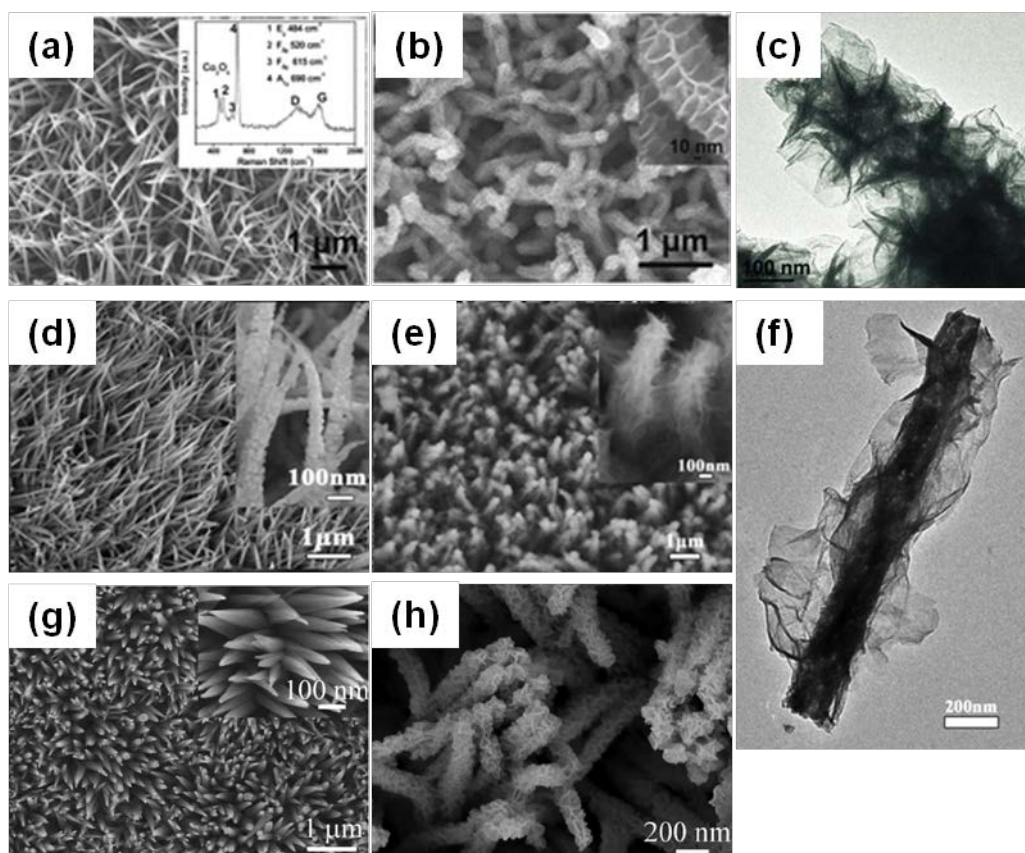
Fig. 14 Various heteronanostructures prepared by Fan and co-workers. (a) SEM image of carbon coated Co_3O_4 nanowire arrays on a stainless steel, (b) SEM and (c) TEM images of Co_3O_4 nanowire@ MnO_2 ultrathin nanosheets; (d) SEM images of CoO nanowires on a nickel foam, (e) SEM and (f) TEM images of CoO nanowire@ $Ni(OH)_2$ nanoflakes; SEM images of Co_3O_4 nanowire (g) and Co_3O_4 nanowire @ NiO nanoflakes (h) on a FTO substrate. (a-c) adapted with permission from Ref. [298], ©2011 Wiley-VCH, (d-f) adapted from Ref. [299], (g, h) adapted with permission from Ref. [300], ©2012 American Chemical Society.

extraordinary areal capacitance of 11.49 F/cm^2, about three times higher than the simple addition of separate CoO (2.3 F/cm^2) and Ni(OH) (1 F/cm^2) components.

Extending their previous attempt of fabricating Co_3O_4 nanosheet @ Co_3O_4 nanowire arrays (NSWA) on Ni foam[165] (discussed in Section 3.2.2), Sun and co-workers synthesized a hierarchical Co_3O_4 nanosheet @ Ni-Co oxides nanorods arrays with a high mass loading of 12 mg on Ni foam.[82] Significantly, the hierarchical electrode presented impressive areal capacitance (specific capacitances) of 24.95 F/cm^2 (2098 F/g) at 5 mA/cm^2 and maintained at ~73 % when the current density increased to 30 mA/cm^2. In addition, the electrode was stable upon continuous cycling and retained at 96 % after 1000 cycles. The electrochemical performance of this hybrid electrode was attributed to the uniform and thin (~10 nm in diameter) Ni-Co oxide nanorods that were accessible to the electrolyte, ensuring high utilization efficiency. Concurrently, the hybrid structure was tightly bound to the Ni foam to facilitate electron transport especially at high rates.

Lee *et al.* fabricated binderless ITO nanowire@$Co(OH)_2$ nanoflake heterostructures directly grown on stainless steel substrate.[293] The specific capacitances of ITO nanowire@ $Co(OH)_2$ nanoflake and $Co(OH)_2$ nanoflake on stainless steel substrates were 622 and 585 F/g respectively. When the scan rate

increased to 100 mV/s, the capacitance retentions for ITO nanowire@$Co(OH)_2$ nanoflake and $Co(OH)_2$ nanoflake were 72.3 and 33.3 % respectively, clearly revealed the improved high rate capability for the former sample. The improved high rate capability of the heterostructured electrode was mainly attributed to the hierarchical geometry. In the electrode, each $Co(OH)_2$ nanoflake was directly connected to the ITO nanowire, which serves as a facile electron path for charge transport, allowing efficient electron conduction during charge-discharge processes.

Mai *et al.* synthesized $MnMoO_4$ nanowire@ $CoMoO_4$ nanowire heterostructures by a combination of micro-emulsion and refluxing method.[303] Their samples were prepared in powder form, and required high weight % of conductive carbon (35.5 %) and binder (4.5 %) to fabricate the working electrode. The hierarchical $MnMoO_4/CoMoO_4$ heterostructures exhibited specific capacitance of ~187 F/g at 1 A/g, which is higher than that of pure $MnMoO_4$ (~10 F/g), $CoMoO_4$ (~63 F/g), and $MnMoO_4/CoMoO_4$ composite (~69 F/g). The differences in capacitance of these different samples are partially related to their differences in specific surface areas. The BET surface area of $MnMoO_4$, $MnMoO_4/CoMoO_4$ composite and hierarchical $MnMoO_4/CoMoO_4$ were 3.17, 28.0, 54.06 m^2/g, respectively. Furthermore, self-aggregation within the hierarchical $MnMoO_4/CoMoO_4$ heterostructures was greatly reduced to retain

the effective contact between the active materials and the electrolyte. Besides, the highly dense $CoMoO_4$ nanorods grown on the $MnMoO_4$ nanowires possessed low crystallinity, providing more surface sites for redox reaction and enabling OH^- access to the heterostructures.
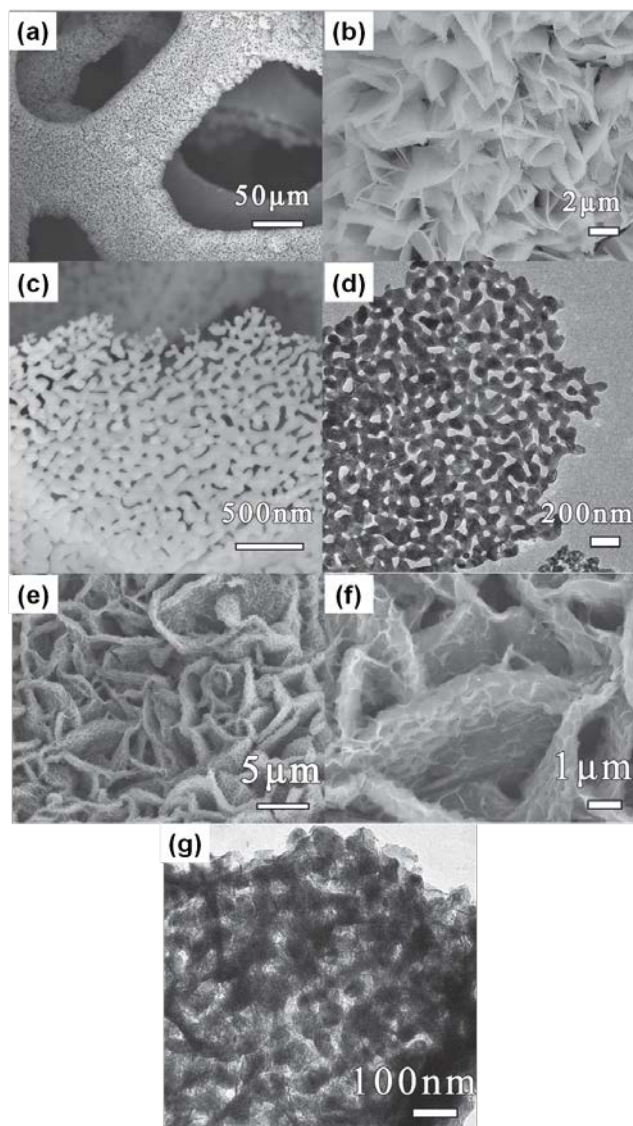

Fig. 15 SEM (a-c) and TEM (d) images of the CoO nanowalls grown directly on the nickel foam; SEM (e,f) and TEM (g) images of the hybrid structure of $CoO@Ni(OH)_2$ obtained after 15 min electrodeposition. Adapted with permission from Ref. [302], ©2012 Wiley-VCH.

The hierarchical $MnMoO_4/CoMoO_4$ heterostructures exhibited good cycling stability and retain 98 % capacitance after 1000 cycles. In comparison to other heterostructures,[293, 298-300] $MnMoO_4/CoMoO_4$ heterostructures exhibited lower capacitance and poorer rate capability. However, the effective potential window (1 V) of this sample is noticeably larger than all other heterostructures.

In addition to heterostructures based on all inorganic components, conducting polymers have also been utilized to fabricate heterostructures with cobalt compounds.[307-309] After growing CoO nanowire arrays on Ni foam, polypyrrole (PPy) was grown onto the nanowire surface as a nanosized thin layer or in the form of nanoparticulates.[308] PPy provided benefits such as high electrical conductivity (10−100 S/cm compared to 10^{-2} S/cm of CoO) to improve electron transport, as well as the pseudocapacitance of PPy itself. The optimized integrated electrode (CoO@PPy) exhibited both high specific capacitance (2223 F/g) and areal capacitances (4.43 F/cm^2); nearly four times higher than those of the pristine CoO nanowire electrode. On the other hand, Han *et al.* prepared CoAl–LDH nanoplatelet array (NPA) on Ni foil by hydrothermal method, followed by electrodeposition of a thin layer of conductive PEDOT polymer onto the surface of the as-prepared LDH NPA.[307] Maximum specific capacitance of 672 F/g was achieved, along with a good long-term cycling stability that retaining 92.5% of the initial capacitance after 5000 cycles.

11. Cobalt compounds-carbon nanomaterials composites

Although pseudocapacitive metal oxides/hydroxides generally exhibit higher specific capacitance as compared to the EDLC of carbon materials, metal oxides/hydroxides undergo physical changes during the repetitious charge-discharge cycles, and thus often have poorer durability. Meanwhile, low conductivity of semiconducting metal oxides/hydroxides severely retards their charge storage capacity especially at high rates. Consequently, rational incorporation of carbon nanomaterials into metal oxide/ hydroxide becomes an important strategy to prepare synergistic composite materials for high performance ECs.[310]

11.1 Composites of cobalt compounds-one dimensional carbon nanomaterials[311-326]

One dimensional (1D) carbon nanomaterials are a distinct class of nanostructured carbon well known for their high electrical conductivity, high mechanical strength, high chemical stability and high surface area. Examples of 1D carbon nanomaterials are carbon nanofibers, single-walled and multi-walled carbon nanotubes (CNTs). Cobalt compounds can be coupled with 1D carbon nanomaterials by diverse routes, including electrodeposition, *in-situ* precipitation/ thermolysis/ thermal decomposition, solid state reaction and so on.

Nickel and cobalt mixed oxides $(Ni/Co)O_x$ were electrochemically deposited onto CNTs film coated-Ni mesh as well as pristine Ni mesh.[311] The CNT film could provide a large surface and interfacial area between $(Ni/Co)O_x$ and the electrolyte solution, keeping the smaller particles from merging together after continuous 1000 cycles. The specific capacitances of $(Ni/Co)O_x$ on Ni mesh and on CNTs-Ni mesh (Ni/Co ratio = 4:6) were 475 F/g and 840 F/g, respectively. In addition, the presence of CNT film increased the cycling stability to over 1000 cycles.

Nitric acid-treated MWCNTs were used as a conductive additive in the preparation of composite electrode based on co-precipitated Co-Al LDH hexagonal nanosheets.[312] When 10 wt % treated MWCNTs were added, the specific capacitance of the electrode increased remarkably from 192 to 342 F/g. The use of MWCNTs improved the diffusion coefficient and the conductivity of the electrode. EIS spectra demonstrated that the inner resistance and contact resistance between particles in the 10 % MWCNTs-LDH composite electrode were smaller than those of the pure Co-Al-LDH. It was speculated that when mixed with

LDH, high surface area and entangled MWCNTs can set up a conductive network to facilitate facile charge-transfer and mass-transfer processes.

On the other hand, $(Ni/Co)O_x$ were grown onto CVD-grown
[5] CNTs film-graphite electrode.[313] Comparative studies showed that $(Ni/Co)O_x$-CNTs (Ni/Co molar ratio = 1:1) had the best reversibility and capacitance. The specific capacitance of $(Ni/Co)O_x$-CNTs was 569 F/g, about 3 times higher than $(Ni/Co)O_x$ without CNTs (193 F/g). Notably, the $(Ni/Co)O_x$-
[10] CNTs exhibited excellent high rate capability to retain 95.4 % of specific capacitance when the current density increased 10 times to 100 mA/cm^2.

A stepwise strategy involving the electrostatic assembly of well dispersed MWCNTs on ITO glass followed by
[15] electrodeposition of cobalt oxyhydroxide (CoOOH) nanoflakes was presented.[314] The specific capacitance of the ITO/MWCNT/CoOOH electrode (389 F/g) was markedly higher than ITO/CoOOH electrode (209 F/g). This capacitance enhancement clearly showed the role of MWCNTs to provide a
[20] unique porous structure and higher surface area to host the electrodeposited CoOOH nanoflakes. Improvement in the transport of electrolyte ions also facilitated the utilization of the electroactive CoOOH. Furthermore, this work demonstrated a few other unique merits: the use of neutral electrolyte (Na_2SO_4),
[25] widen potential window (0.1 to 0.9 V) and tuneable MWCNT/CoOOH pairs.

$NiCo_2O_4$-SWCNTs, Ni-Co hydroxide composite, NiCoAl LDH nanosheets-MWCNTs were prepared by precipitation in the presence of CNTs.[315-317] Slower hydrolysis was observed in
[30] water/ethanol (ratio 1:4) and optimum for uniform coating of $NiCo_2O_4$ nanocrystals onto SWCNT walls. The optimized electrode exhibited high specific capacitance of 1642 F/g (~4.9 F/cm^2) at 0.5 A/g. When the current density increased to 20 A/g, 53.5 % of the highest specific capacitance can be retained,
[35] displaying a good rate capability. The nanocomposite electrode exhibited good cycling stability, i.e. 94.1 % of the initial capacitance was maintained after 2000 cycles. According to EIS analysis, $NiCo_2O_4$-SWCNTs composite showed lower internal resistance and charge transfer resistance than those of pure
[40] $NiCo_2O_4$ sample.

Ko and Yoon synthesized $(Ni/Co)O_x$-carbon fibers onto Ni foam by thermal decomposition of metal salts solution in the presence of carbon fibers.[318] The specific capacitance of $(Ni/Co)O_x$-carbon fibers composite and $(Ni/Co)O_x$ were 1271 and
[45] 936 F/g at scan rate of 5 mV/s, and 955 and 612 F/g when scan rate increased to 100 mV/s. The mass loading of $(Ni/Co)O_x$-carbon fibers composite can be increased from 0.81 to 3.26 mg/cm^2 without reducing considerably the specific capacitance, while providing a high areal capacitance of ~4 F/cm^2. The same
[50] research group extended similar synthesis scheme to prepare $CoMnO_2$-carbon fibers composite[83]. The composite electrodes exhibited specific capacitance of 630 F/g, higher than $CoMnO_2$ alone (419 F/g) and excellent capacitance retention of 95 % after 10000 cycles.

[55] Mullen and Feng's group synthesized Co_3O_4-incorporated 1D nanoporous carbons (NPCs) via an organometallic precursor-controlled thermolysis approach.[319] After thermolysis, AAO template removal and further heat treatment, the polyphenylene skeletons were transformed to 1D NPCs with homogenous
[60] dispersion of Co_3O_4 hollow nanocrystals. The specific capacitance of NPCs/Co_3O_4 was 382 F/g at 3 A/g, higher than conventional MWCNTs-supported Co_3O_4 (126 F/g). At current density of 30 and 60 A/g, 81 % and 72.8 % of the capacitance were retained respectively, showing a remarkable rate capability.
[65] Corrected specific capacitances contributed by Co_3O_4 nanocrystals were 1066, 1028, 951, 879 and 721 F/g at 3, 6, 12, 30, 60 A/g respectively. After 4500 cycles, 89 % of the initial capacitance of the NPCs/Co_3O_4 was maintained.

A carbon nanofibers (CNF) paper was made by thermal
[70] treatment of electrospun polyacrylonitrile fibrous paper, followed by chemical precipitation of $Co(OH)_2$.[320] Interesting, mutually enhanced capacitances in the composite were observed: the composite paper exhibited higher specific capacitance in the potential range of -1 to 0 V, about 24 % higher than the pure CNF
[75] paper; while the specific capacitance of the composite paper in the potential range of -0.2 to 0.35 V was about 30 % higher than that of $Co(OH)_2$ alone. Yan and co-workers reported another study on Co_3O_4/CNTs composites by precipitating Co_3O_4 onto acid-pretreated CNTs.[321] The calculated specific capacitances for
[80] pure MWCNT, Co_3O_4 and composite with different weight percentage of MWCNT were presented in Table 4, along with the results of surface area and porosity. Obviously, the addition of MWCNT significantly improved the specific capacitance of Co_3O_4. This improvement was achieved due to the high specific
[85] surface area and the suitable pore size distribution in favour of the absorption and transport of electrolyte ions through the porous channels within the composite electrode. Besides, EIS analysis showed that the incorporation of MWCNT decreased the internal resistance and charge transfer resistance of Co_3O_4, hence
[90] improved overall electrical conductivity of Co_3O_4. Finally, the capacitance retention after 2000 cycles was determined to be 91 %.

Table 4 Specific surface area, pore volume, pore size and specific capacitance of the Co_3O_4/MWCNT composites. Reproduced with
[95] permission from Ref. [321], ©2011 Elsevier.

Wt % of MWCNTs	BET specific surface area (m^2/g)	BJH pore volume (cc/g)	BJH pore size (nM)	Specific capacitance (F/g)
0	82	0.35	13.8	263
3	86	0.35	12.9	287
5	137	0.29	6.2	418
7	110	0.41	11.9	315
15	116	0.43	11.5	285
100	-	-	-	95

CNTs-CoS composites were also prepared by several authors.[322, 323] Modifying a previously developed interface hydrothermal method[219] by incorporating poly(sodium-4-styrene sulfonate) (PSS)-functionalized MWCNTs (FMWCNTs), Zhang and co-
[100] workers prepared amorphous CoS_x nanoparticles highly dispersed onto the FMWCNTs.[322] PSS with negative charges could covalently functionalize MWCNTs and increase its solubility in aqueous solution. The FMWCNTs surface then tethered metal ions with positive charge and resulted in the homogeneous
[105] deposition of metal sulfide nanoparticles. The use of FMWCNTs efficiently restrained the aggregation of CoS_x nanoparticles and enhanced the homogeneous dispersion, thus the deposited CoS_x nanoparticles had larger exposed surface area and higher surface

energy. Furthermore, the three dimensionally entangled FWCNTs remitted the inter-particle electron hopping resistance during the redox transition and thus enhanced the electronic conductivity of the composite. A specific capacitance of 334 F/g was obtained for the nanocomposite at 0.4 A/g. 89.8 % (300 F/g) of the specific capacitance was maintained when the current density increased to 3 A/g, displaying an excellent rate capability and surpassing all the CoS_x-based electrodes. The capacitance retention was about 95 % after 1000 cycles.

Xu et al.[324] synthesized $CoMoO_4$ nanoplatelets anchored on acid functionalized (AF)-MWCNTs via a solvent-free solid state reaction. The ground mixture was heated in the microwave. The BET surface area of $CoMoO_4$/MWCNT composite was 58.1 m^2/g, in which the composite was found to contain ~24.8 % AF-MWCNTs (BET surface area: 110 m^2/g) and ~75.2 % of $CoMoO_4$ (BET surface area: 41.2 m^2/g). The randomly oriented $CoMoO_4$ nanoplatelets possessed an interesting crystalline-amorphous core-shell structure. In contrast to most cobalt-based compounds and composites, the $CoMoO_4$/MWCNT electrode exhibited pseudocapacitance in a larger potential window of -0.55 to 0.25 V (Hg/HgO). The electrode produced specific capacitances of 170, 115 and 96 F/g at 0.1, 0.5 and 1 A/g, respectively.

11.2 Composites of cobalt compounds-two dimensional carbon nanomaterials

Graphene is strictly a two-dimensional (2D) single-atom-thick planar sheet of sp^2 bonded carbon atoms.[65] However, a loose meaning of "graphene" is usually used to describe a variety of graphene-related materials, covering a broad spectrum of structural and chemical derivatives of graphene.[64, 65, 67-70] Chemically derived graphene, such as graphene oxide (GO) and reduced graphene oxide (rGO) offer advantage in terms of chemical processability to form various composites with cobalt compounds.

By using Na_2S as a precursor of depositing agent (OH^-) and reducing agent (HS^- and H_2S), graphene-$Co(OH)_2$ composites were prepared via simultaneous reduction of GO to rGO and deposition of $Co(OH)_2$.[327] The specific capacitances of $Co(OH)_2$, rGO and $Co(OH)_2$-rGO composite were ~726, ~138 and ~973 F/g. Fan et al. prepared Co_3O_4-rGO composite by microwave-assisted synthesis followed by calcination in air.[328] The highest specific capacitances of Co_3O_4-rGO composite and rGO were ~243 and ~169 F/g, respectively. After 2000 cycles, the capacitance decreased by 4.4 % of the initial capacitance.

Co_3O_4,[329, 330] $Co(OH)_2$,[331] Co_xS_y,[332, 333] $NiCo_2O_4$,[334] $Co_{0.5}Ni_{0.5}(OH)_2$,[335] $NiCo_2S_4$,[336] $Ni(OH)_2$/CoO composite[337] nanostructures bound on rGO were fabricated via different procedures. The as-prepared Co_3O_4-rGO composite delivered a maximum specific capacitance of 478 F/g, while nanosized (<50 nM) commercial Co_3O_4 powders and rGO sheets produced maximum specific capacitances of 118 F/g and 245 F/g, respectively. In the composite, the presence of Co_3O_4 prevents the rGO sheets from aggregation and restacking, increasing the surface area accessible to the electrolyte. Specifically, Wang's study revealed that the BET surface area of bare rGO sheets is 93.7 m^2/g. In the presence of Co_3O_4 nanoparticles as spacers, the BET surface area of the Co_3O_4-rGO was extended to 219.2 m^2/g. On the other hand, the restricted particle sizes of Co_3O_4 formed

onto graphene domain would lead to an increase of their pseudocapacitance.

Yu et al. synthesized Co_3O_4 nanoscrolls-rGO via a two-step chemical precipitation and thermal annealing process.[338] Although the pure Co_3O_4 nanoscrolls presented a very low specific capacitance of ~15 F/g as compared to most reported literature, the incorporation of rGO managed to elevate the specific capacitance to ~160 F/g. Similarly, Co_3O_4-rGO composite prepared by Hu and colleagues exhibited higher specific capacitance (291 F/g) than the individual counterparts of rGO (56 F/g) and Co_3O_4 (161 F/g).[339]

While all the above examples[327, 328, 338-340] involve the conventional chemical synthesis process, Konstantinov and colleagues presented a unique alternative route.[341] In their preparation scheme, commercial powder of $Co(OH)_2$ was dissolved in nitric acid, then added and homogenized into a diluted GO dispersion in water. The 20 % rGO-Co_3O_4 composite was obtained by spray pyrolyzing the suspension into a vertical type spray pyrolysis reactor at 500-1000 °C. SEM and TEM images of the rGO-Co_3O_4 composite obtained are shown in Figure 16a-c, illustrating the globular structure. Co_3O_4 nanoparticles wrapped within bended rGO sheets, forming an interconnected 3D network structure. Specific capacitances of rGO-Co_3O_4 composite were measured from CV as 687 and 580 F/g at 5 and 100 mV/s respectively, demonstrating a high specific capacitance and good rate capability. After 1000 continuous CV cycles, the specific capacitance decreased by 6.9 %.
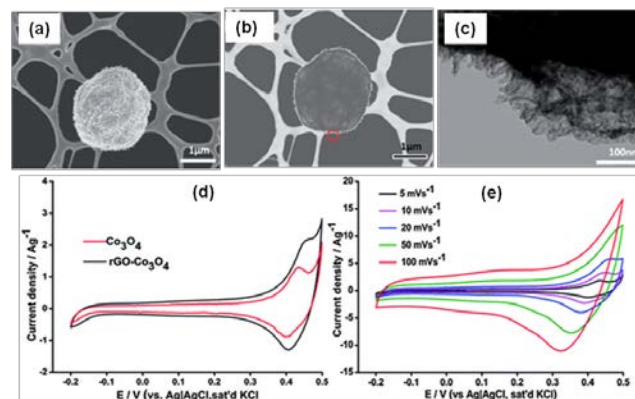

Fig. 16 SEM (a) and TEM (b and c) images of rGO-Co_3O_4 after spraying; (c) comparative CV curves at 5 mV/s for Co_3O_4 and rGO-Co_3O_4 and (d) CV curves at different scan rates for the rGO-Co_3O_4. Adapted from Ref. 341.

In contrast to the irregular nanoparticle shapes in Co_3O_4 and $Co(OH)_2$ hybridized with rGO, Jin's group presented an elegant way to fabricate electrode materials by layered assembly of two types of atomically-thin nanosheets, namely carboxylated graphene oxide and Co-Al LDH-nanosheet (NS).[342] A reported synthesis protocol[343] was adopted to obtain single-layer thin (~0.8 nM) and positive charge-bearing $[Co_{0.66}Al_{0.34}(OH)_2]^+$ (zeta potential = 43 mV). Meanwhile, carboxylated GO (zeta potential = -50 mV) was negatively charged. Thus, the electrostatic interaction between GO and Co-Al LDH-NS could create a layered assembly as shown in Figure 17. The specific capacitances of the layered composite were measured as 1031, 854, 483, 250 F/g at current densities of 1, 2, 8, 20 A/g. After 6000 charge-discharge cycles at 20 A/g, the capacitance remained

stable. In their follow-up study, they fabricated flexible films of Co-Al-LDH NS/rGO via layer-by-layer (LBL) assembly onto surface modified-ITO substrates.[344] Four films with 10, 20, 30 and 40 bilayers were prepared, with a mean thickness of about 4 nm for one bilayer (one Co-Al LDH-NS plus one GO). The specific capacitance of the four samples ranged in 944-880 F/g, not obviously varied with the bilayer numbers. The specific capacitances of the 40-bilayer film were 880, 713, 648, 539 and 461 F/g at scan rates of 5, 10, 20, 50 and 100 mV/s, respectively. After the partial reduction of rGO to restore its conductivity, the specific capacitances of the 40-bilayer film were increased to 1204, 984, 828, 715 and 585 F/g. On the other hand, Co-Al LDH/rGO composite were prepared by precipitation under reflux condition in the presence of urea.[345, 346] The composites showed a maximum specific capacitance of ~700-800 F/g.

Similar with Jin's electrostatic assembly approach,[342] *p*-aminobenzoate (PABA) ion-intercalated Co-Ni hydroxides were exfoliated to charge-bearing nanosheets and used as building blocks to construct composite with graphene oxide.[347] During a post-thermal treatment, GO was reduced by divalent cobalt while Co-Ni hydroxide nanosheets were transformed to $NiCo_2O_4$ particles. The $NiCo_2O_4$-rGO composite exhibited specific capacitances of 835 F/g at 1 A/g and maintained at 73.7 % (615 F/g) when the current density increased to 20 A/g. The specific capacitance of the electrode increased to 1050 F/g after 450 cycles and eventually remained at 908 F/g after 4000 cycles. Comparatively, the electrochemical performance in terms of specific capacitance, rate capability and cycling stability of the $NiCo_2O_4$-rGO composite was substantially better than pure $NiCo_2O_4$ and mechanically mixed $NiCo_2O_4$-rGO composite.
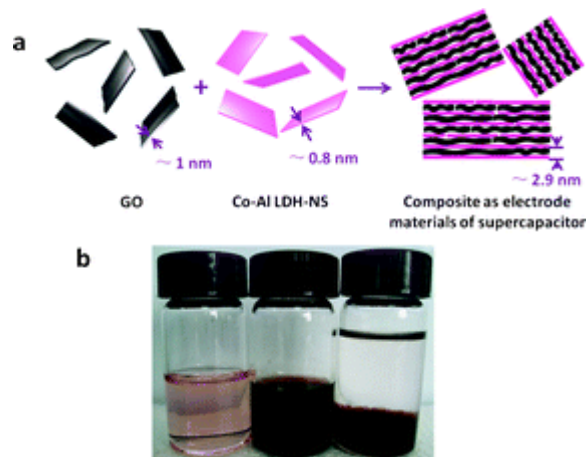

Fig. 17 (a) Schematic of the formation and structure of Co-Al LDH-NS/GO composite and (b) photograph of left an aqueous dispersion of Co-Al LDH-NS, (middle) an aqueous dispersion of GO and (right) a mixture of Co-Al LDH-NS and GO. Reproduced from Ref. [342].

Intriguingly, Yuan *et al.* present a facile approach to fabricate free-standing and binder-free flexible hybrid paper made of monolayer Co_3O_4 microsphere arrays grown on rGO/CNTs (Figure 18).[348] GO was reduced to rGO simultaneously during the hydrothermal treatment. Meanwhile, the CNTs were sandwiched in between the rGO sheets. The weight fraction of Co_3O_4 in the hybrid film was about 48 %. The Co_3O_4-flexible paper electrode exhibited specific capacitances of 378, 364, 351, 330, 323 and 297 F/g at 2, 3, 4, 5, 6 and 8 A/g, respectively. The cycling

performance was evaluated at increasing current densities for 2300 cycles and returned to 2 A/g, about 96 % of the initial capacitance could be recovered and maintained for another 700 cycles. The excellent electrochemical performance of the electrode was attributed to the intimate integration between the rGO/CNTs and the Co_3O_4 microspheres. Another binder- and additive-free electrode was obtained by sequential growth of vertically aligned graphene sheets on Ni foam followed by electrodeposition of $Co(OH)_2$.[349]
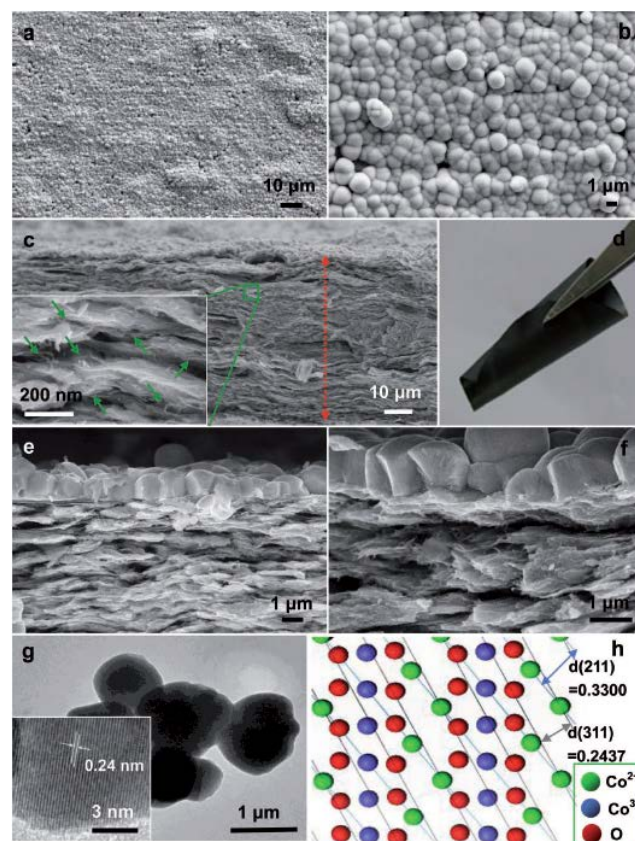

Fig. 18 Typical a,b) top-view and c) side-view FESEM images of the flexible Co_3O_4/rGO/CNTs hybrid paper. The inset in (c) is the enlarged part of the region indicated by the green rectangle. The photograph in (d) demonstrates the flexibility of the paper. e,f) Enlarged cross-sectional view of the paper. g) TEM and HRTEM (the inset in g) images of Co_3O_4 microspheres. h) Atomic structure of the cubic phase Co_3O_4. Adapted with permission from Ref. [348], ©2012 Wiley-VCH.

11.3　Composites of cobalt compounds-three dimensional carbon nanomaterials[50, 350-355]

Ordered mesoporous carbons (OMC), with extremely high surface areas, controllable pore size, narrow pore size distribution, ordered pore structures and interconnected pore channels, have been studied for applications in electrochemical energy storage and sensors.[50, 350] Beside directly being used as electrode materials for EDLCs, OMC can also be used as a 3D support for pseudocapacitive materials. $Co(OH)_2$ was deposited onto the mesoporous carbon CMK-3 by a conventional chemical precipitation method.[351] Without the CMK-3 support, as-precipitated $Co(OH)_2$ consisted of amorphous particles and nanoflakes. In the presence of CMK-3, $Co(OH)_2$ was grown with a uniform distribution of interconnected nanoflakes onto the surface of the CMK-3 wall, forming a unique 3D network

structure with large surface area and inner space. The specific capacitances of the composite electrodes increased linearly with increasing content of CMK-3. Composite with 20 wt % CMK-3 achieved the highest specific capacitance of 750 F/g, contributed by both EDL capacitance originating from the CMK-3 and pseudocapacitance from the Co(OH)$_2$ nanoflakes. The composite electrode exhibited better high rate discharge capability compared with Co(OH)$_2$ electrode. The composite was able to maintain 86 % of its initial specific capacitance when the discharge current density increased from 5 to 50 mA/cm^2. The mesoporous wall of CMK-3 reduces the ion intercalation distance to nanometre range, facilitating the charge transfer. At the same time, the large mesopores (~20-50 nm) of the interlaced nanoflakes enhance the diffusion of electrolyte ions in the porous electrode.

Beside hard templates, soft template approaches have been used to fabricate mesoporous carbon composite films containing cobalt oxide.[352, 353] The presence of Co$_3$O$_4$ nanoparticles increased the specific capacitance of the mesoporous carbon composite thin film from 22 F/g to 114 F/g (10 % cobalt loading) and 125 F/g (20 % cobalt loading). Apart from higher specific capacitance, Co-containing mesoporous carbon foams (Co-MCF) also presented better rate capability. The improvement is attributed to improved wettability and thus better electrolyte-electrode contact, increased graphitization degree, and faradaic pseudocapacitance contributed by cobalt. It should be noted that in both studies,[352, 353] cobalt compounds were used as an additive to enhance the capacitive performance rather than a major electrode material.

Furthermore, NiCo$_2$O$_4$ nanocrystals (3-5 nm) were grown on conductive mesoporous carbon aerogel.[354] At low mass loading (~0.23 mg), the composite electrode showed a very high specific capacitance of 1700 F/g, excellent high rate capabilities and cycling stability. Co$_3$O$_4$ nanoparticles (66% of total weight) were embedded in a specially crafted mesoporous silica (SBA-15)-porous carbon membrane.[355] The specific capacitance of the electrode achieved 1086 F/g (1645 F/g based on Co$_3$O$_4$).

12. The use of 3D macroporous and other nanostructured support or current collectors for cobalt-based electrode materials.

In recent years, beside conventional planar current collectors such as metallic (e.g. Cu, Ni and Ti) foil, 3D macroporous current collectors in the form of foam or mesh are becoming more popular in ECs.[356] Applications of 3D current collectors are motivated by the larger surface area, enhanced electrolyte diffusion, efficient electron pathways and effective utilization of active materials.

12.1 Nickel foam as current collector

Effects of different Ni substrates (plate vs. foam) on specific capacitance of electrodeposited porous α-Co(OH)$_2$ film have been investigated.[207] The capacitance of α-Co(OH)$_2$ porous film/Ni foam is about two times of the capacitance of α-Co(OH)$_2$ porous film/Ni plate. Apparently, the CV curve of α-Co(OH)$_2$ porous film/Ni foam consisted of two redox pairs while there was only one redox pair for the CV curve of α-Co(OH)$_2$ porous film/Ni plate.

However, Xing *et al.* performed a cautious evaluation on the contribution of nickel foam to the specific capacitances of active electrode materials.[357] Based on combinatory results from XPS analysis and electrochemical studies, they found that using nickel foam as a current collector could bring substantial error to the quantification of specific capacitances. In the continuous cycling of pure nickel foam in 1 M KOH, the redox couples relevant to various species of nickel hydroxides and oxyhydroxides were observed. The formation of nickel hydroxides or oxides on the nickel foam was also evidenced by the appearance of golden colour and the XPS analysis. These electroactive species could bring a significant overestimation of specific capacitance of other evaluated electrode materials, especially when small quantity (e.g. < 1 mg) of the electrode materials is used.[198, 207]

As an easily available, cheap, wide pH compatible (from neutral to basic) and high performance current collector, the use of nickel foam is obvious. However, careful subtraction of the capacitance contribution from nickel foam, or additional studies by using other inert 3D macroporous current collectors such as titanium foam, should be performed in order to avoid misleading and overestimated energy storage capacity. This is crucial especially when high capacity novel electrode materials are to be reported.

12.2 Nickel porous and nanostructured current collectors[358-365]

In addition to 3D nickel foam, various nanostructured nickel current collectors were also reported. The use of nanostructured current collectors provides shorter electrolyte ion transport path and larger surface area for high current during redox reaction, thus achieving improved charge storage performance. Chang *et al.* prepared a Ni-Cu alloy layer on nickel foil by electroplating, followed by anodic dissolution of Cu from the alloy layer.[358] Next, either Co$_3$O$_4$[359] and Co(OH)$_2$[360, 361] was deposited onto the porous Ni framework and a flat Ni foil (as a control). At the same deposited Co(OH)$_2$ amount, Co(OH)$_2$-porous Ni framework (60 mF/cm^2 or 2650 F/g) obviously exhibited higher specific capacitance than Co(OH)$_2$-Ni foil (12 mF/cm^2 or 550 F/g). More importantly, the porous Ni framework is beneficial for loading a higher quantity of electroactive materials, leading to higher areal capacitance. Co(OH)$_2$-porous Ni framework presented high rate capability to retain 93 % capacitance when the CV scan rate increased from 5 to 200 mV/s. Notably, similar to Xing's work[357] as mentioned in section 12.1, Chang *et al.* observed that, upon continuous cycling of porous nickel framework in alkaline electrolyte, Ni(OH)$_2$ was formed and contributed to the voltammetric charge. The authors further speculated that the incorporation of Ni(OH)$_2$/NiOOH into the deposited Co(OH)$_2$ probably formed a Co-Ni mixed hydroxide based on an analysis of the CV curve. The incorporation of Ni(OH)$_2$/NiOOH has significantly resolved the dissolution problem of Co(OH)$_2$ in KOH solution.

Xia *et al.* prepared 3D porous nickel film by hydrogen bubble-templated method, followed by constant current cathodic electrodeposition of α-Co(OH)$_2$ nanoflakes[362] (Figure 19). In comparison to α-Co(OH)$_2$ nanoflakes deposited on commercial Ni foam, the α-Co(OH)$_2$ nanoflakes on 3D porous Ni film undergo more complete redox reaction as indicated by the appearance of an additional pair of redox couple. The specific

capacitances of α-Co(OH)$_2$ nanoflakes-3D porous Ni film were 2028 F/g (2 F/cm^2) and 1920 F/g (1.9 F/cm^2) at current densities of 2 A/g and 40 A/g, respectively. These values were noticeably much higher than α-Co(OH)$_2$ nanoflakes-Ni foam (880 F/g and 727 F/g, respectively). The high capacitance of α-Co(OH)$_2$ nanoflakes-3D porous Ni film was able to retain at 94.7 % after 2000 cycles at 2 A/g.

In contrast to the above examples, a porous nickel layer was electrodeposited on hydrothermally synthesized α-Co(OH)$_2$ nanoflake arrays.[363] Incorporation of nickel (15 wt %) activated an additional pair of redox couple, shortened the potential separation between oxidation and reduction peaks and enhanced the peak currents. In addition, from galvanostatic charge-discharge curves, the α-Co(OH)$_2$/Ni composite nanoflake arrays presented lower charge voltage plateau and higher discharge voltage plateau, indicating a smaller polarization. EIS analysis further confirmed a lower charge transfer resistance and ion diffusion resistance of Co(OH)$_2$/Ni composite nanoflake arrays than that of the pristine α-Co(OH)$_2$ nanoflake arrays. The Co(OH)$_2$/Ni composite nanoflake arrays exhibited high rate capability to retain 87.6 % of capacitance when charge-discharge current densities increased from 1 A/g (1310 F/g) to 40 A/g (775 F/g).
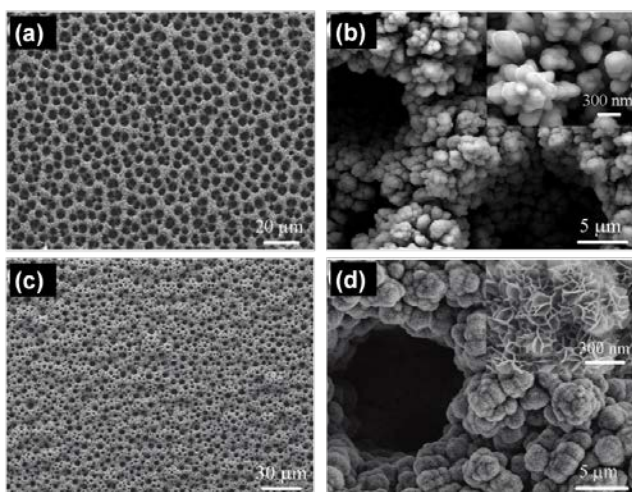
A nickel grainy layer coated Si-microchannel plates (MCPs) was used as an 3D support for Ni(OH)$_2$ and Co(OH)$_2$ nanostructures.[364, 365] Then, α-Co(OH)$_2$ nanostructures were deposited on the Si-MCPs by chemical bath deposition. The top walls of the Si-MCPs/Ni were covered by Co(OH)$_2$ nanorods while the side walls were deposited with Co(OH)$_2$ nanoflakes. An areal capacitance of 1.46 F/cm^2 was obtained for the Si-MCPs/Ni/Co(OH)$_2$ at 10 mV/s.[364] However, the electrode showed poor rate capability and suffered from 19.4 % capacitance loss after 2000 cycles.

12.3   Carbon-materials based 3D current collectors[366-375]

Carbon fiber paper (CFP) is made of interconnected conductive carbon microfibers with macroporous channels. It is extensively used in membrane electrode assembly (MEA) of proton exchange membrane (PEM) fuel cell. The interconnected and conductive fiber networks in CFP provide efficient electron transport paths especially at high rates, while effective electrolyte diffusion enabled by pore channels, establishing CFP as an attractive 3D current collectors for pseudocapacitive metal oxide materials. Liu *et al.* coated a thin layer of Co$_3$O$_4$ nanonets and nanocubes on CFP (Figure 20a-d) and studied the electrochemical capacitance of the electrode by two-electrode setup.[366] Owing to the much lower percolation threshold of Co$_3$O$_4$ nanonets than nanocubes, the nanonets electrode possesses more electron or ion pathways and faster charge carriers transport. In contrast to most reported Co$_3$O$_4$ electrodes, the CV curve of the Co$_3$O$_4$ nanostructures-CFP did not exhibit redox peaks commonly seen. The Co$_3$O$_4$ nanonets-CFP is ~948 F/g at current density of 14.06 A/g (mass loading = 1.4 mg/cm^2), demonstrating a high specific capacitance, high rate capability and long cycling stability up to 5000 cycles. Later, the same research group fabricated a 3D hierarchical Co$_x$Ni$_{1-x}$ double-hydroxide nanosheets coated NiCo$_2$O$_4$ nanowires grown on CFP with an improved rate capability and cycling stability.[367]

Similarly, Rakhi *et al.* adopted CFP as well as planar graphite paper as current collector to grow Co$_3$O$_4$ nanowires by solvothermal method.[368] In their study, it was found that the configuration of nanowires was strongly dependent on the type of substrates: brush-like morphology for carbon fiber paper while flower-like morphology for planar graphite paper as shown in Figure 20e and f. The specific capacitances calculated from the discharge curves (1 A/g) for brush-like and flower-like morphologies in three-electrode configuration were 1525 F/g and 1199 F/g, respectively. Furthermore, the electrodes were subjected to further electrochemical analysis by two-electrode configuration. Similar to Liu's work,[366] the CV curves from two-electrode configuration show no redox peak. The specific capacitances calculated from discharge curves based on two-electrode configuration for brush-like and flower-like morphologies were 911 F/g and 620 F/g respectively at low current density of 0.25 A/g. At high current density (25 A/g), the retained capacitance for brush-like and flower-like morphologies were 87 % and 71 % respectively. The better high rate capability of brush-like morphology was attributed to high electrical conductivity of the composite, homogenous dispersion of Co$_3$O$_4$ nanowires around carbon fibers, rapid transport of the electrolyte ions in the pore channels between carbon fibers and thus increasing the electrochemical utilization of Co$_3$O$_4$. Based on this work, it is worthwhile to further emphasize the differences between the 2-electrode and 3-electrode electrochemical setup.[11] A three-electrode cell is definitely important to study the electrochemical characteristics of electrode materials, e.g. redox behavior of Co$_3$O$_4$; while a two-electrode cell is better to inform the most practical indication of a material's performance, as it simulates various factors in a packaged EC such as physical configuration, internal voltages, and charge transfer.[11]

Being an abundant and cost-effective material, textiles with flexibility, stretchable, wearable and light-weight properties can be incorporated as wearable electronic and energy storage devices.[369] With the availability of graphene and carbon nanotubes in the well-dispersed "ink" form, conductive textiles are now easily attained. By repeating a simple "dipping and drying" procedure, coating of poly(sodium-4-styrene sulfonate)-

functionalized multiwalled carbon nanotubes (MWCNTs) onto a textile sheet was achieved.[370] β-Co(OH)$_2$ nanopetals were then deposited onto this MWCNTs-cotton textile via a mild hydrothermal treatment. High areal capacitances of 11.22 F/cm^2 and 7.71 F/cm^2 were achieved at 15 mA/cm^2 and 60 mA/cm^2, respectively. On the other hand, mesoporous NiCo$_2$O$_4$ nanowire arrays,[371] MnO$_2$ nanowire/CoAl LDH heterostructures[372] were grown on carbon textiles substrates. The NiCo$_2$O$_4$ nanowire arrays exhibited a high specific capacitance of 1010 F/g at high current density (20 A/g), retaining 79 % of the capacitance at 1 A/g.[371]
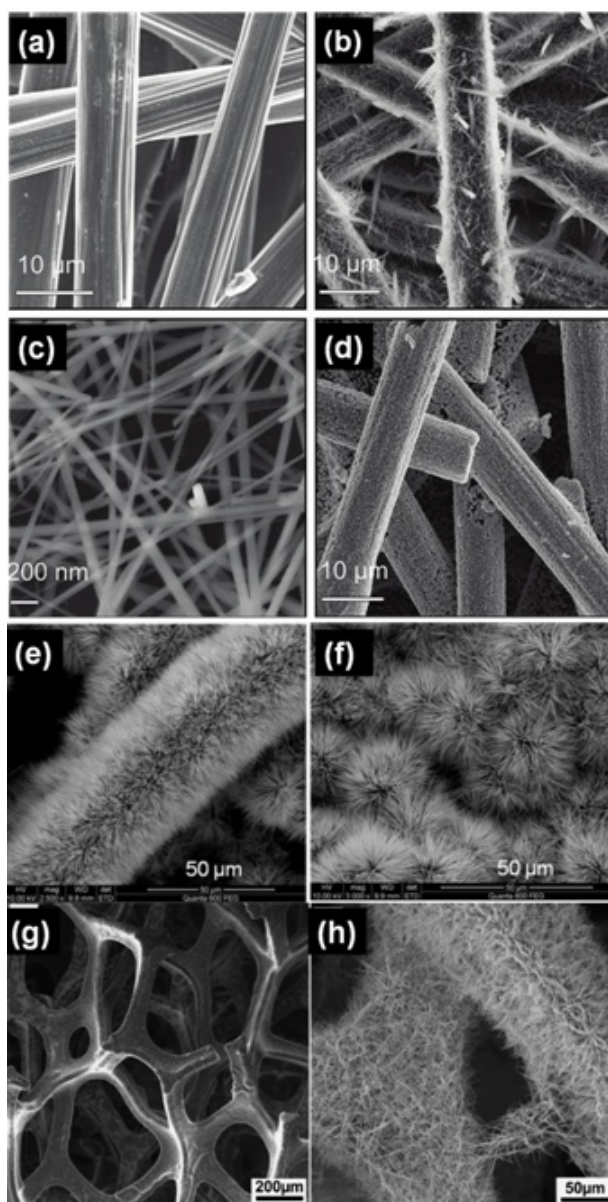

Fig. 20 SEM images of carbon fiber papers (CFP) before coating (a), after coating of Co$_3$O$_4$ nanonet (b and c) and Co$_3$O$_4$ nanocube (d) (Ref. [366]); Co$_3$O$_4$ nanowires with brush-like morphology on CFP (e) and flower like morphology on planar graphite paper (f) (Ref. [368]); graphene foam (g) and Co$_3$O$_4$ nanowires on graphene foam (Ref. [375]). Adapted with permission from Ref. [366], [368] and [375], ©2012 American Chemical Society.

Inspired by the role of nickel foil used in chemical vapour deposition (CVD) growth of graphene recently, CVD-grown graphene[373] and graphite[374] foams were successfully prepared by using nickel foam as a catalyst and sacrificial template. The 3D macroporous graphene foam (Figure 20g), which retains the interconnected architectures in nickel foam, is highly conductive, and free of inter-graphene sheet resistance.[373] Similar with the above examples of CFP and MWCNTs-cotton textiles, hydrothermal method was used to synthesize Co$_3$O$_4$ nanowires onto the graphene foam[375] (Figure 20h). The authors demonstrated that the Co$_3$O$_4$ nanowires-graphene foam presented high specific capacitance of ~1100 F/g at 10 A/g with excellent cycling stability.

12.4 Zeolite materials as 3D micro/meso-porous dispersing support

Li and co-workers introduced an elegant way to exploit high surface area microporous zeolites as a cation-exchange host to disperse loose Co(OH)$_2$ nanowhiskers.[376-379] Coprecipitated Co(OH)$_2$ nanowhiskers were grown on the exterior of ultra-stable Y zeolite (USY), forming a loosely packed microstructure with ample voids (Figure 21).[376, 377] Nevertheless, the composite material is able to exhibit a high specific and areal capacitance. The highest specific capacitance of the composite was 1492 F/g, while corrected specific capacitance for the Co(OH)$_2$ phase was 3500 F/g, which is comparable to theoretical capacitance value (3460 F/g). Despite of the amphiprotic nature of zeolite, cycling stability was good, retaining ~96 % capacitance after 6000 cycles.
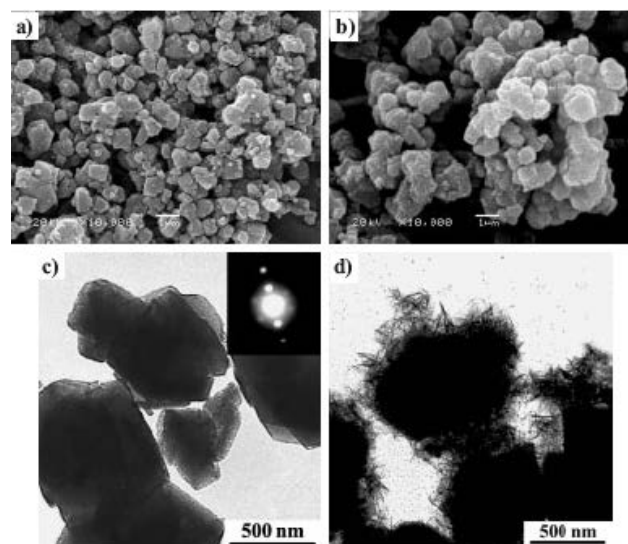
Fig. 21 SEM and TEM images of pure USY (a and c) and Co(OH)$_2$/USY nanocomposite with 48 wt. % Co(OH)$_2$ loading (b and d.) Reproduced with permission from Ref. 310, ©2004 Wiley-VCH.

Conclusions and Outlook

The above summary demonstrates the versatile synthesis approaches for nanostructured cobalt-based compounds, giving sufficiently good controllability on their structural and textural properties that are significant for surface redox reactions. Cobalt compounds, as wide bandgap semiconductors or insulators however, have intrinsically low electrical conductivity and this greatly impair the electron transport kinetics. Doped conductive oxides, nanostructured current collectors, and integration with

conductive carbon nanomaterials are several rational strategies to boost their electrochemical performances. Meanwhile, cobalt-based mixed oxides and cobalt LDHs also present a wide range of new pseudocapacitive materials. The adjustable ratios, compositions and thus properties of these mixed oxides and LDHs offer new opportunities for further improvements. While substantial achievements were made in terms of materials designs, the development has always fallen short for the ever-growing demands ranging from portable electronics to transportation.

Several future trends in this field can be noted as follows:

Cobalt compounds-novel carbon nanomaterials. The emergence of new carbon materials (e.g. graphene foam[373], "activated" graphene[380], graphene quantum dots[381]) as well as the various existing forms provide versatile platforms for the integration with cobalt compounds and its composites. Synergistic combination of carbon nanomaterials with metal oxides can maximize the benefits from both components. For instance, graphene was found to improve the overall electrical conductivity of metal oxides, and this is particularly important for high power applications.[76]

Advanced 3D hierarchical hetero-nanostructures. Multi-component heteronanostructures built from nanoscale components, as well as the strategic exploitation of the remaining free space, offer unique opportunities with multi-facet challenges[24]. The complexity includes balancing various transportation requirements of the electronic, ionic and electrolyte fluid. As an example, while porous nanostructured nanomaterials offer ion transport pathways, the grain boundaries and disorders may induce additional electrical resistance. Although nanostructures have illustrated improved performance over their bulk counterparts, reports on the fundamental understanding such as electron transport for different classes of nanomaterials are scarce.

Current collectors: nano-micro-macro hierarchical architectures and unconventional ones. By designing novel current collectors with a proper hierarchical systems of macropores, mesopores and micropores, a balance of efficient transport of electrolyte, ions and electrons would be achieved. In addition, unconventional current collectors such as carbon fiber papers, CNTs bulky paper, flexible conductive cotton textiles and carbon cloths, flexible and transparent polyethylene terephthalate (PET), sponges, paper etc., offer new arena for different niche designs and applications such as wearable electronics.

Asymmetric ECs.[9] Restricted by the intrinsic electrochemical properties of cobalt compounds, the operating potential window is typically very small (positive potential window of about ~0.5 V). Asymmetric configuration with cobalt compounds as the positive electrode, and other negative electrodes such as carbon nanomaterials and iron oxides[382 and references therein], could possibly extend the effective potential window and give higher energy density. Various asymmetric ECs consisting of cobalt compounds and composites have been demonstrated.[242, 278, 296, 308, 334, 374, 383-391] However, critical factors such as the electrode matching, mass ratio, suitable electrolytes, etc. for optimizing the device electrochemical performance (specific capacitance, EC voltage, energy density, power density and cycling stability) remain to be explored.[392]

Standardization of methods to report electrochemical capacitors' performance. Although impressive specific capacitances (F/g) were widely reported for cobalt-based compounds and composites, many studies were performed on very low mass loading (< 1 mg) of the active materials. Low mass loading possibly lead to exaggerated specific capacitance calculated, especially when electrochemical active current collector is also used.[357] Furthermore, the practical capacitance value and measured output is low. Maintaining high specific capacitance with high mass loading indicate that an electrode material offers a high utilization efficiency and is practical for real applications.[82] It is proposed that authors should always report the mass loading or areal capacitances and even volumetric capacitances of their samples. Standardization of methods to evaluate the performance of electrode materials should be earnestly considered by the scientific community.[11]

Notes and references

ªDepartment of Chemistry, National University of Singapore, 3 Science Drive 3, Singapore 117543; kiankeat@gmail.com (K.K. Lee); chmcws@nus.edu.sg (W.S. Chin)

ᵇDepartment of Physics, National University of Singapore, 2 Science Drive 3, Singapore 117542; physowch@nus.edu.sg (C.H. Sow)

† Electronic Supplementary Information (ESI) available: Detailed experimental conditions (current collectors, potential window, electrolytes, methods) and their electrochemical performance (specific and areal capacitance, cycling life, rate capabilities) from the reviewed literatures were summarized in tables. See DOI: 10.1039/b000000x/

1. R. E. Smalley, *Top Ten Problems of Humanity for Next 50 Years*, Rice University, 2003.
2. R. E. Smalley, *Energy*, Rice University, Rice University, 2003.
3. U. S. D. o. E. Office of Basic Energy Sciences, *Basic Research Needs for Electrical Energy Storage, Report of the Basic Energy Sciences Workshop on Electrical Energy Storage*, 2007.
4. M. S. Whittingham, *MRS Bull.*, 2008, **33**, 411-419.
5. D. R. Rolison and L. F. Nazar, *MRS Bull.*, 2011, **36**, 486-493.
6. M. Winter and R. J. Brodd, *Chem. Rev.*, 2004, **104**, 4245-4270.
7. B. E. Conway, *Electrochemical Supercapacitors: Scientific Fundamentals and Technological Applications* Plenum Press, New York, 1999.
8. K. Naoi, Morita, M., *Electrochem. Soc. Interface*, 2008, **17**, 44-48.
9. J. W. Long, D. Belanger, T. Brousse, W. Sugimoto, M. B. Sassin and O. Crosnier, *MRS Bull.*, 2011, **36**, 513-522.
10. R. J. Brodd, K. R. Bullock, R. A. Leising, R. L. Middaugh, J. R. Miller and E. Takeuchi, *J. Electrochem. Soc.*, 2004, **151**, K1.
11. M. D. Stoller and R. S. Ruoff, *Energy Environ. Sci.*, 2010, **3**, 1294-1301.
12. Y. M. Vol'fkovich and T. M. Serdyuk, *Russ. J. Electrochem.*, 2002, **38**, 935-958.
13. J. R. Miller, Burke, A. F., *Electrochem. Soc. Interface*, 2008, **17**, 53-57.
14. J. W. Long, *Electrochem. Soc. Interface*, 2008, **17**, 33.
15. D. R. Rolison and L. F. Nazar, *MRS Bull.*, 2011, **36**, 486-493.
16. M. J. Laudenslager, R. H. Scheffler and W. M. Sigmund, *Pure Appl. Chem.*, 2010, **82**, 2137-2156.
17. P. J. Hall, M. Mirzaeian, S. I. Fletcher, F. B. Sillars, A. J. R. Rennie, G. O. Shitta-Bey, G. Wilson, A. Cruden and R. Carter, *Energy Environ. Sci.*, 2010, **3**, 1238-1251.
18. J. R. Miller, Simon, P., *Electrochem. Soc. Interface*, 2008, **17**, 31-32.
19. S. A. Sherrill, P. Banerjee, G. W. Rubloff and S. B. Lee, *Phys. Chem. Chem. Phys.*, 2011, **13**, 20714-20723.
20. N. A. Choudhury, S. Sampath and A. K. Shukla, *Energy Environ. Sci.*, 2009, **2**, 55-67.
21. D. Bélanger, Brousse, T., Long, J. W. , *Electrochem. Soc. Interface*, 2008, **17**, 49-52.
22. P. Simon and Y. Gogotsi, *Nat. Mater.*, 2008, **7**, 845-854.

23. S. Sarangapani, B. V. Tilak and C. P. Chen, *J. Electrochem. Soc.*, 1996, **143**, 3791-3799.

24. D. R. Rolison, J. W. Long, J. C. Lytle, A. E. Fischer, C. P. Rhodes, T. M. McEvoy, M. E. Bourg and A. M. Lubers, *Chem. Soc. Rev.*, 2009, **38**, 226-252.

25. K. Naoi, *Fuel Cells*, 2010, **10**, 825-833.

26. P. Simon, Burke, A. F., *Electrochem. Soc. Interface*, 2008, **17**, 38-43.

27. A. S. Arico, P. Bruce, B. Scrosati, J. M. Tarascon and W. van Schalkwijk, *Nat Mater*, 2005, **4**, 366-377.

28. K. Naoi, Simon, P., *Electrochem. Soc. Interface*, 2008, **17**, 34-37.

29. J. Zhang and X. S. Zhao, *ChemSusChem*, 2012, **5**, 818-841.

30. R. Kotz and M. Carlen, *Electrochim. Acta*, 2000, **45**, 2483-2498.

31. Y. Zhang, H. Feng, X. B. Wu, L. Z. Wang, A. Q. Zhang, T. C. Xia, H. C. Dong, X. F. Li and L. S. Zhang, *Int. J. Hydrogen Energy*, 2009, **34**, 4889-4899.

32. A. Burke, *Electrochim. Acta*, 2007, **53**, 1083-1091.

33. G. P. Wang, L. Zhang and J. J. Zhang, *Chem. Soc. Rev.*, 2012, **41**, 797-828.

34. P. Sharma and T. S. Bhatti, *Energy Convers. Manage.*, 2010, **51**, 2901-2912.

35. B. E. Conway, V. Birss and J. Wojtowicz, *J. Power Sources*, 1997, **66**, 1-14.

36. X. Zhao, B. M. Sanchez, P. J. Dobson and P. S. Grant, *Nanoscale*, 2011, **3**, 839-855.

37. M. Jayalakshmi and K. Balasubramanian, *Int. J. Electrochem. Sc.*, 2008, **3**, 1196-1217.

38. A. Burke and M. Miller, *Electrochim. Acta*, 2010, **55**, 7538-7548.

39. A. Burke, *Int. J. Energ. Res.*, 2010, **34**, 133-151.

40. J. N. Tiwari, R. N. Tiwari and K. S. Kim, *Prog. Mater Sci.*, 2012, **57**, 724-803.

41. S. Chen, W. Xing, J. Duan, X. Hu and S. Z. Qiao, *J. Mater. Chem. A*, 2013, **1**, 2941.

42. P. Simon, Y. Gogotsi and B. Dunn, *Science*, 2014, **343**, 1210-1211.

43. W. T. Deng, X. B. Ji, Q. Y. Chen and C. E. Banks, *RSC Adv.*, 2011, **1**, 1171-1178.

44. L. L. Zhang and X. S. Zhao, *Chem. Soc. Rev.*, 2009, **38**, 2520-2531.

45. M. Inagaki, H. Konno and O. Tanaike, *J. Power Sources*, 2010, **195**, 7880-7903.

46. C. Liu, F. Li, L. P. Ma and H. M. Cheng, *Adv. Mater.*, 2010, **22**, E28-+.

47. D. S. Su and R. Schlogl, *ChemSusChem*, 2010, **3**, 136-168.

48. A. Davies and A. P. Yu, *Can. J. Chem. Eng.*, 2011, **89**, 1342-1357.

49. S. W. Lee, B. M. Gallant, H. R. Byon, P. T. Hammond and Y. Shao-Horn, *Energy Environ. Sci.*, 2011, **4**, 1972-1985.

50. C. Z. Yuan, B. Gao, L. F. Shen, S. D. Yang, L. Hao, X. J. Lu, F. Zhang, L. J. Zhang and X. G. Zhang, *Nanoscale*, 2011, **3**, 529-545.

51. Y. P. Zhai, Y. Q. Dou, D. Y. Zhao, P. F. Fulvio, R. T. Mayes and S. Dai, *Adv. Mater.*, 2011, **23**, 4828-4850.

52. S. Bose, T. Kuila, A. K. Mishra, R. Rajasekar, N. H. Kim and J. H. Lee, *J. Mater. Chem.*, 2012, **22**, 767-784.

53. A. Ghosh and Y. H. Lee, *ChemSusChem*, 2012, **5**, 480-499.

54. V. V. N. Obreja, *Physica E-Low-Dimensional Systems & Nanostructures*, 2008, **40**, 2596-2605.

55. M. Noked, A. Soffer and D. Aurbach, *J. Solid State Electrochem.*, 2011, **15**, 1563-1578.

56. J. Biener, M. Stadermann, M. Suss, M. A. Worsley, M. M. Biener, K. A. Rose and T. F. Baumann, *Energy Environ. Sci.*, 2011, **4**, 656.

57. R. W. Fu, Z. H. Li, Y. R. Liang, F. Li, F. Xu and D. C. Wu, *New Carbon Mater.*, 2011, **26**, 171-178.

58. C. Liu and H. M. Cheng, *J. Phys. D-Appl. Phys.*, 2005, **38**, R231-R252.

59. H. Zhang, G. Cao and Y. Yang, *Energy Environ. Sci.*, 2009, **2**, 932-943.

60. H. Pan, J. Y. Li and Y. P. Feng, *Nanoscale Res. Lett.*, 2010, **5**, 654-668.

61. W.-D. Zhang, B. Xu and L.-C. Jiang, *J. Mater. Chem.*, 2010, **20**, 6383-6391.

62. G. Lota, K. Fic and E. Frackowiak, *Energy Environ. Sci.*, 2011, **4**, 1592-1605.

63. J. M. Schnorr and T. M. Swager, *Chem. Mater.*, 2011, **23**, 646-657.

64. L. L. Zhang, R. Zhou and X. S. Zhao, *J. Mater. Chem.*, 2010, **20**, 5983-5992.

65. D. A. C. Brownson, D. K. Kampouris and C. E. Banks, *J. Power Sources*, 2011, **196**, 4873-4885.

66. J. Hou, Y. Shao, M. W. Ellis, R. B. Moore and B. Yi, *Phys. Chem. Chem. Phys.*, 2011, **13**, 15384-15402.

67. M. Pumera, *Energy Environ. Sci.*, 2011, **4**, 668-674.

68. Y. Sun, Q. Wu and G. Shi, *Energy Environ. Sci.*, 2011, **4**, 1113-1132.

69. X. Huang, X. Qi, F. Boey and H. Zhang, *Chem. Soc. Rev.*, 2012, **41**, 666-686.

70. Y. Huang, J. Liang and Y. Chen, *Small*, 2012, **8**, 1805-1834.

71. T. Brezesinski, J. Wang, S. H. Tolbert and B. Dunn, *J. Sol-Gel Sci. Technol.*, 2010, **57**, 330-335.

72. C. D. Lokhande, D. P. Dubal and O. S. Joo, *Curr. Appl. Phys.*, 2011, **11**, 255-270.

73. W. Wei, X. Cui, W. Chen and D. G. Ivey, *Chem. Soc. Rev.*, 2011, **40**, 1697-1721.

74. H. Jiang, J. Ma and C. Li, *Adv. Mater.*, 2012, n/a-n/a.

75. M. B. Sassin, C. N. Chervin, D. R. Rolison and J. W. Long, *Acc. Chem. Res.*, 2012.

76. Z.-S. Wu, G. Zhou, L.-C. Yin, W. Ren, F. Li and H.-M. Cheng, *Nano Energy*, 2012, **1**, 107-131.

77. Q. Lu, J. G. Chen and J. Q. Xiao, *Angew Chem Int Ed Engl*, 2013, **52**, 1882-1889.

78. B. L. Ellis, P. Knauth and T. Djenizian, *Adv Mater*, 2014, **26**, 3368-3397.

79. G. A. Snook, P. Kao and A. S. Best, *J. Power Sources*, 2011, **196**, 1-12.

80. J. Jiang, Y. Li, J. Liu, X. Huang, C. Yuan and X. W. Lou, *Adv. Mater.*, 2012, **24**, 5166-5180.

81. Y.-L. Wang, Y.-Q. Zhao and C.-L. Xu, *J. Solid State Electrochem.*, 2011, **16**, 829-834.

82. Z. Y. Lu, Q. Yang, W. Zhu, Z. Chang, J. F. Liu, X. M. Sun, D. G. Evans and X. Duan, *Nano Res.*, 2012, **5**, 369-378.

83. S. H. KIm, Kim, Y.I., Park, J.H., Ko, J.M., *Int. J. Electrochem. Sc.*, 2009, **4**, 1489-1496.

84. P. Benson, G. W. D. Briggs and W. F. K. Wynne-Jones, *Electrochim. Acta*, 1964, **9**, 275-280.

85. P. Benson, G. W. D. Briggs and W. F. K. Wynne-Jones, *Electrochim. Acta*, 1964, **9**, 281-288.

86. B. E. Conway, *J. Electrochem. Soc.*, 1991, **138**, 1539-1548.

87. T. C. Liu, W. G. Pell and B. E. Conway, *Electrochim. Acta*, 1999, **44**, 2829-2842.

88. V. Srinivasan and J. W. Weidner, *J. Electrochem. Soc.*, 1997, **144**, L210-L213.

89. C. Lin, J. A. Ritter and B. N. Popov, *J. Electrochem. Soc.*, 1998, **145**, 4097-4103.

90. M. Pourbaix, *Atlas of Electrochemical Equilibria in Aqueous Solutions*, 2nd edn., National Association of Corrosion Engineers, Houston, Tex., 1974.

91. J. Chivot, L. Mendoza, C. Mansour, T. Pauporté and M. Cassir, *Corros. Sci.*, 2008, **50**, 62-69.

92. P. Delahay, M. Pourbaix and P. Van Rysselberghe, *J. Chem. Educ.*, 1950, **27**, 683.

93. W. K. Behl and J. E. Toni, *J. Electroanal. Chem. Interfacial Electrochem.*, 1971, **31**, 63-75.

94. C. N. P. Dafonseca, M. A. Depaoli and A. Gorenstein, *Sol. Energy Mater. Sol. Cells*, 1994, **33**, 73-81.

95. H. G. Meier, J. R. Vilche and A. J. Arvía, *J. Electroanal. Chem. Interfacial Electrochem.*, 1982, **138**, 367-379.

96. R. Boggio, A. Carugati and S. Trasatti, *J. Appl. Electrochem.*, 1987, **17**, 828-840.

97. F. Svegl, B. Orel, M. G. Hutchins and K. Kalcher, *J. Electrochem. Soc.*, 1996, **143**, 1532-1539.

98. M. Longhi and L. Formaro, *J. Electroanal. Chem.*, 1999, **464**, 149-157.

99. T. Kessler, A. Visintin, M. R. Dechialvo, W. E. Triaca and A. J. Arvia, *J. Electroanal. Chem.*, 1989, **261**, 315-329.

100. J. Ismail, M. F. Ahmed and P. V. Kamath, *J. Power Sources*, 1991, **36**, 507-516.

101. L. D. Burke, M. E. Lyons and O. J. Murphy, *J. Electroanal. Chem. Interfacial Electrochem.*, 1982, **132**, 247-261.

102. G. Larramona and C. Gutierrez, *J. Electroanal. Chem.*, 1990, **293**, 237-252.

103. R. D. Cowling and Riddifor.Ac, *Electrochim. Acta*, 1969, **14**, 981-&.

104. I. G. Casella and M. R. Guascito, *J. Electroanal. Chem.*, 1999, **476**, 54-63.

105. M. Figlarz, J. Guenot and Tournemo.Jn, *J. Mater. Sci.*, 1974, **9**, 772-776.

106. V. Pralong, A. Delahaye-Vidal, B. Beaudoin, B. Gerand and J. M. Tarascon, *J. Mater. Chem.*, 1999, **9**, 955-960.

107. M. Figlarz, J. Guenot and F. Fievetvincent, *J. Mater. Sci.*, 1976, **11**, 2267-2270.

108. E. Hosono, S. Fujihara, I. Honma and H. S. Zhou, *J. Mater. Chem.*, 2005, **15**, 1938-1945.

109. Y. L. Hou, H. Kondoh, M. Shimojo, T. Kogure and T. Ohta, *J. Phys. Chem. B*, 2005, **109**, 19094-19098.

110. L.-X. Yang, Y.-J. Zhu, L. Li, L. Zhang, H. Tong, W.-W. Wang, G.-F. Cheng and J.-F. Zhu, *Eur. J. Inorg. Chem.*, 2006, **2006**, 4787-4792.

111. X. Liu, R. Yi, N. Zhang, R. Shi, X. Li and G. Qiu, *Chem.-Asian J.*, 2008, **3**, 732-738.

112. Y. Ding, L. Xu, C. Chen, X. Shen and S. L. Suib, *J. Phys. Chem. C*, 2008, **112**, 8177-8183.

113. L. Hu, Q. Peng and Y. Li, *J. Am. Chem. Soc.*, 2008, **130**, 16136-16137.

114. Y. Shao, J. Sun and L. Gao, *J. Phys. Chem. C*, 2009, **113**, 6566-6572.

115. Q. D. Wu, S. Liu, S. M. Yao and X. P. Gao, *Electrochem. Solid-St. Lett.*, 2008, **11**, A215-A218.

116. C. C. Li, X. M. Yin, Q. H. Li, L. B. Chen and T. H. Wang, *Chem.-Eur. J.*, 2011, **17**, 1596-1604.

117. Y. Fan, H. Shao, J. Wang, L. Liu, J. Zhang and C. Cao, *Chem. Commun.*, 2011, **47**, 3469-3471.

118. J. Yang, H. W. Liu, W. N. Martens and R. L. Frost, *J. Phys. Chem. C*, 2010, **114**, 111-119.

119. X. W. Lou, D. Deng, J. Y. Lee, J. Feng and L. A. Archer, *Adv. Mater.*, 2008, **20**, 258-+.

120. F. Zhan, B. Geng and Y. Guo, *Chem.-Eur. J.*, 2009, **15**, 6169-6174.

121. Y. Zhu, H. Li, Y. Koltypin and A. Gedanken, *J. Mater. Chem.*, 2002, **12**, 729-733.

122. C.-H. Chen, S. F. Abbas, A. Morey, S. Sithambaram, L.-P. Xu, H. F. Garces, W. A. Hines and S. L. Suib, *Adv. Mater.*, 2008, **20**, 1205-1209.

123. B. Geng, F. Zhan, C. Fang and N. Yu, *J. Mater. Chem.*, 2008, **18**, 4977-4984.

124. S. R. Alvarado, Y. Guo, T. P. A. Ruberu, A. Bakac and J. Vela, *J. Phys. Chem. C*, 2012, **116**, 10382-10389.

125. J. T. Sampanthar and H. C. Zeng, *J. Am. Chem. Soc.*, 2002, **124**, 6668-6675.

126. Y. Li, B. Tan and Y. Wu, *J. Am. Chem. Soc.*, 2006, **128**, 14258-14259.

127. D. Wang, Q. Wang and T. Wang, *Inorg. Chem.*, 2011, **50**, 6482-6492.

128. X. Chen, J. P. Cheng, Q. L. Shou, F. Liu and X. B. Zhang, *CrystEngComm*, 2012, **14**, 1271-1276.

129. G. Godillot, L. Guerlou-Demourgues, P. L. Taberna, P. Simon and C. Delmas, *Electrochem. Solid-St. Lett.*, 2011, **14**, A139-A142.

130. F. Tronel, L. Guerlou-Demourgues, M. Menetrier, L. Croguennec, L. Goubault, P. Bernard and C. Delmas, *Chem. Mater.*, 2006, **18**, 5840-5851.

131. J. A. Xu, L. Gao, J. Y. Cao, W. C. Wang and Z. D. Chen, *Electrochim. Acta*, 2010, **56**, 732-736.

132. L. Gong, X. Liu, L. Su and L. Wang, *J. Solid State Electrochem.*, 2011, **16**, 297-304.

133. M. B. Zheng, J. Cao, S. T. Liao, J. S. Liu, H. Q. Chen, Y. Zhao, W. J. Dai, G. B. Ji, J. M. Cao and J. Tao, *J. Phys. Chem. C*, 2009, **113**, 3887-3894.

134. R.-T. Wang, L.-B. Kong, J.-W. Lang, X.-W. Wang, S.-Q. Fan, Y.-C. Luo and L. Kang, *J. Power Sources*, 2012, **217**, 358-363.

135. W. Du, R. Liu, Y. Jiang, Q. Lu, Y. Fan and F. Gao, *J. Power Sources*, 2013, **227**, 101-105.

136. Y. Wang, Y. Lei, J. Li, L. Gu, H. Yuan and D. Xiao, *ACS Appl. Mater. Interfaces*, 2014, **6**, 6739-6747.

137. T. Ishikawa and E. Matijević, *Colloid Polym. Sci.*, 1991, **269**, 179-186.

138. R. Xu and H. C. Zeng, *J. Phys. Chem. B*, 2003, **107**, 12643-12649.

139. W.-W. Wang and Y.-J. Zhu, *Mater. Res. Bull.*, 2005, **40**, 1929-1935.

140. Z. G. Zhao, F. X. Geng, J. B. Bai and H. M. Cheng, *J. Phys. Chem. C*, 2007, **111**, 3848-3852.

141. S. K. Meher and G. R. Rao, *J. Phys. Chem. C*, 2011, **115**, 25543-25556.

142. J. P. Cheng, X. Chen, J.-S. Wu, F. Liu, X. B. Zhang and V. P. Dravid, *CrystEngComm*, 2012, **14**, 6702.

143. K. Byrappa and M. Yoshimura, in *Handbook of Hydrothermal Technology*, William Andrew Publishing, Norwich, NY, 2001.

144. W. Shi, S. Song and H. Zhang, *Chem Soc Rev*, 2013, **42**, 5714-5743.

145. Y. Mao, T.-J. Park, F. Zhang, H. Zhou and S. S. Wong, *Small*, 2007, **3**, 1122-1139.

146. X. Wang and Y. Li, *Inorg. Chem.*, 2006, **45**, 7522-7534.

147. C. N. R. Rao, V. V. Agrawal, K. Biswas, U. K. Gautam, M. Ghosh, A. Govindaraj, G. U. Kulkarni, K. R. Kalyanikutty, K. Sardar and S. R. C. Vivekchandi, *Pure Appl. Chem.*, 2006, **78**, 1619-1650.

148. S. Xiong, C. Yuan, X. Zhang, B. Xi and Y. Qian, *Chem.-Eur. J.*, 2009, **15**, 5320-5326.

149. G. Wang, X. Shen, J. Horvat, B. Wang, H. Liu, D. Wexler and J. Yao, *J. Phys. Chem. C*, 2009, **113**, 4357-4361.

150. L. Cui, J. Li and X. G. Zhang, *J. Appl. Electrochem.*, 2009, **39**, 1871-1876.

151. T. Zhu, J. S. Chen and X. W. Lou, *J. Mater. Chem.*, 2010, **20**, 7015-7020.

152. B. Wang, T. Zhu, H. B. Wu, R. Xu, J. S. Chen and X. W. Lou, *Nanoscale*, 2012, **4**, 2145-2149.

153. Y. Wang, Z. Zhong, Y. Chen, C. Ng and J. Lin, *Nano Res.*, 2011, **4**, 695-704.

154. Y. Xiao, A. Zhang, S. Liu, J. Zhao, S. Fang, D. Jia and F. Li, *J. Power Sources*, 2012, **219**, 140-146.

155. S. K. Meher and G. R. Rao, *J. Phys. Chem. C*, 2011, **115**, 15646-15654.

156. L. Hou, C. Yuan, L. Yang, L. Shen, F. Zhang and X. Zhang, *RSC Adv.*, 2011, **1**, 1521-1526.

157. Y. Xiao, S. Liu, F. Li, A. Zhang, J. Zhao, S. Fang and D. Jia, *Adv. Funct. Mater.*, 2012, **22**, 4052-4059.

158. T.-Y. Wei, C.-H. Chen, K.-H. Chang, S.-Y. Lu and C.-C. Hu, *Chem. Mater.*, 2009, **21**, 3228-3233.

159. X. Wang, A. Sumboja, E. Khoo, C. Yan and P. S. Lee, *J. Phys. Chem. C*, 2012, **116**, 4930-4935.

160. X. Qing, S. Liu, K. Huang, K. Lv, Y. Yang, Z. Lu, D. Fang and X. Liang, *Electrochim. Acta*, 2011, **56**, 4985-4991.

161. C. Yuan, L. Yang, L. Hou, L. Shen, F. Zhang, D. Li and X. Zhang, *J. Mater. Chem.*, 2011, **21**, 18183-18185.

162. F. Zhang, C. Yuan, X. Lu, L. Zhang, Q. Che and X. Zhang, *J. Power Sources*, 2012, **203**, 250-256.

163. X. H. Xia, J. P. Tu, Y. J. Mai, X. L. Wang, C. D. Gu and X. B. Zhao, *J. Mater. Chem.*, 2011, **21**, 9319-9325.

164. X.-h. Xia, J.-p. Tu, Y.-q. Zhang, Y.-j. Mai, X.-l. Wang, C.-d. Gu and X.-b. Zhao, *RSC Adv.*, 2012, **2**, 1835.

165. Q. Yang, Z. Lu, Z. Chang, W. Zhu, J. Sun, J. Liu, X. Sun and X. Duan, *RSC Adv.*, 2012, **2**, 1663-1668.

166. B. R. Duan and Q. Cao, *Electrochim. Acta*, 2012, **64**, 154-161.

167. Q. Yang, Z. Lu, X. Sun and J. Liu, *Sci. Rep.*, 2013, **3**, 3537.

168. R. S. Mane and C. D. Lokhande, *Mater. Chem. Phys.*, 2000, **65**, 1-31.

169. G. Hodes, *Phys. Chem. Chem. Phys.*, 2007, **9**, 2181-2196.

170. J. A. Switzer and G. Hodes, *MRS Bull.*, 2010, **35**, 743-752.

171. S. M. Pawar, B. S. Pawar, J. H. Kim, O.-S. Joo and C. D. Lokhande, *Curr. Appl. Phys.*, 2011, **11**, 117-161.

172. Y. Gao, S. Chen, D. Cao, G. Wang and J. Yin, *J. Power Sources*, 2010, **195**, 1757-1760.

173. H. Cheng, Z. G. Lu, J. Q. Deng, C. Y. Chung, K. L. Zhang and Y. Y. Li, *Nano Res.*, 2010, **3**, 895-901.

174. Y. G. Li, B. Tan and Y. Y. Wu, *J. Am. Chem. Soc.*, 2006, **128**, 14258-14259.

175. S. G. Kandalkar, D. S. Dhawale, C. K. Kim and C. D. Lokhande, *Synth. Met.*, 2010, **160**, 1299-1302.
176. Q. Pan, H. Jin, H. Wang and G. Yin, *Electrochim. Acta*, 2007, **53**, 951-956.
177. J. Liu, X. Huang, Y. Li, Z. Li, Q. Chi and G. Li, *Solid State Sciences*, 2008, **10**, 1568-1576.
178. J. Liu, X. Huang, Y. Li, K. M. Sulieman, X. He and F. Sun, *J. Mater. Chem.*, 2006, **16**, 4427-4434.
179. X. Wen, W. Zhang and S. Yang, *Langmuir*, 2003, **19**, 5898-5903.
180. Y. Li, K. Huang, Z. Yao, S. Liu and X. Qing, *Electrochim. Acta*, 2011, **56**, 2140-2144.
181. H. Wang, L. Zhang, X. Tan, C. M. B. Holt, B. Zahiri, B. C. Olsen and D. Mitlin, *J. Phys. Chem. C*, 2011, **115**, 17599-17605.
182. V. Srinivasan and J. W. Weidner, *J. Power Sources*, 2002, **108**, 15-20.
183. J.-K. Lee, G.-P. Kim, K.-H. Kim, I. K. Song and S.-H. Baeck, *J. Nanosci. Nanotechno.*, **10**, 3676-3679.
184. J. B. Wu, Y. Lin, X. H. Xia, J. Y. Xu and Q. Y. Shi, *Electrochim. Acta*, 2011, **56**, 7163-7170.
185. Y. F. Yuan, X. H. Xia, J. B. Wu, X. H. Huang, Y. B. Pei, J. L. Yang and S. Y. Guo, *Electrochem. Commun.*, 2011, **13**, 1123-1126.
186. X.-H. Xia, J.-P. Tu, X.-L. Wang, C.-D. Gu and X.-B. Zhao, *Chem. Commun.*, 2011, **47**, 5786-5788.
187. V. R. Shinde, S. B. Mahadik, T. P. Gujar and C. D. Lokhande, *Appl. Surf. Sci.*, 2006, **252**, 7487-7492.
188. R. Tummala, R. K. Guduru and P. S. Mohanty, *J. Power Sources*, 2012, **209**, 44-51.
189. C. Yuan, X. Zhang, B. Gao and J. Li, *Mater. Chem. Phys.*, 2007, **101**, 148-152.
190. C. Yuan, L. Hou, L. Shen, D. Li, F. Zhang, C. Fan, J. Li and X. Zhang, *Electrochim. Acta*, 2010, **56**, 115-121.
191. Z.-A. Hu, Y.-L. Xie, Y.-X. Wang, L.-J. Xie, G.-R. Fu, X.-Q. Jin, Z.-Y. Zhang, Y.-Y. Yang and H.-Y. Wu, *J. Phys. Chem. C*, 2009, **113**, 12502-12508.
192. L. Wang, Z. H. Dong, Z. G. Wang, F. X. Zhang and J. Jin, *Adv. Funct. Mater.*, 2013, **23**, 2758-2764.
193. L.-B. Kong, J.-W. Lang, M. Liu, Y.-C. Luo and L. Kang, *J. Power Sources*, 2009, **194**, 1194-1201.
194. C. Yuan, X. Zhang, L. Hou, L. Shen, D. Li, F. Zhang, C. Fan and J. Li, *J. Mater. Chem.*, 2010, **20**, 10809-10816.
195. L. Hou, C. Yuan, L. Yang, L. Shen, F. Zhang and X. Zhang, *CrystEngComm*, 2011, **13**, 6130-6135.
196. C. Z. Yuan, L. Yang, L. R. Hou, D. K. Li, L. F. Shen, F. Zhang and X. G. Zhang, *J. Solid State Electrochem.*, 2012, **16**, 1519-1525.
197. J. Jiang, J. Liu, R. Ding, J. Zhu, Y. Li, A. Hu, X. Li and X. Huang, *ACS Appl. Mater. Interfaces*, 2010, **3**, 99-103.
198. F. Cao, G. X. Pan, P. S. Tang and H. F. Chen, *J. Power Sources*, 2012, **216**, 395-399.
199. V. Gupta, T. Kusahara, H. Toyama, S. Gupta and N. Miura, *Electrochem. Commun.*, 2007, **9**, 2315-2319.
200. W.-J. Zhou, J. Zhang, T. Xue, D.-D. Zhao and H.-l. Li, *J. Mater. Chem.*, 2008, **18**, 905-910.
201. W. J. Zhou, M. W. Xu, D. D. Zhao, C. L. Xu and L. Li, *Microporous Mesoporous Mater.*, 2009, **117**, 55-60.
202. W.-J. Zhou, D.-D. Zhao, M.-W. Xu, C.-L. Xu and H.-L. Li, *Electrochim. Acta*, 2008, **53**, 7210-7219.
203. P. K. Nayak and N. Munichandraiah, *J. Electrochem. Soc.*, 2008, **155**, A855-A861.
204. S. L. Chou, J. Z. Wang, H. K. Liu and S. X. Dou, *J. Electrochem. Soc.*, 2008, **155**, A926-A929.
205. Z. J. Yu, Y. Dai and W. Chen, *J. Chin. Chem. Soc.*, 2010, **57**, 423-428.
206. T. Zhao, H. Jiang and J. Ma, *J. Power Sources*, 2011, **196**, 860-864.
207. L.-B. Kong, M.-C. Liu, J.-W. Lang, M. Liu, Y.-C. Luo and L. Kang, *J. Solid State Electrochem.*, 2010, **15**, 571-577.
208. K. Hoshino and Y. Hitsuoka, *Electrochem. Commun.*, 2005, **7**, 821-828.
209. Y. Asano, T. Komatsu, K. Murashiro and K. Hoshino, *J. Power Sources*, 2011, **196**, 5215-5222.
210. T. Xue, X. Wang and J.-M. Lee, *J. Power Sources*, 2012, **201**, 382-386.
211. E. Hosono, S. Fujihara, I. Honma, M. Ichihara and H. S. Zhou, *J. Power Sources*, 2006, **158**, 779-783.
212. K. K. Lee, P. Y. Loh, C. H. Sow and W. S. Chin, *Electrochem. Commun.*, 2012, **20**, 128-132.
213. K. K. Lee, P. Y. Loh, C. H. Sow and W. S. Chin, *Biosens. Bioelectron.*, 2013, **39**, 255-260.
214. A. D. Jagadale, D. P. Dubal and C. D. Lokhande, *Mater. Res. Bull.*, 2012, **47**, 672-676.
215. F. Tao, Y. Q. Zhao, G. Q. Zhang and H. L. Li, *Electrochem. Commun.*, 2007, **9**, 1282-1287.
216. S.-J. Bao, C. M. Li, C.-X. Guo and Y. Qiao, *J. Power Sources*, 2008, **180**, 676-681.
217. P. Justin and G. Ranga Rao, *Int. J. Hydrogen Energy*, 2010, **35**, 9709-9715.
218. Q. Wang, L. Jiao, H. Du, J. Yang, Q. Huan, W. Peng, Y. Si, Y. Wang and H. Yuan, *CrystEngComm*, 2011, **13**, 6960.
219. C. Yuan, B. Gao, L. Su, L. Chen and X. Zhang, *J. Electrochem. Soc.*, 2009, **156**, A199.
220. L. Hou, C. Yuan, D. Li, L. Yang, L. Shen, F. Zhang and X. Zhang, *Electrochim. Acta*, 2011, **56**, 7454-7459.
221. L. Zhang, H. B. Wu and X. W. Lou, *Chem. Commun.*, 2012, **48**, 6912-6914.
222. W. Dong, X. Wang, B. Li, L. Wang, B. Chen, C. Li, X. Li, T. Zhang and Z. Shi, *Dalton T.*, 2011, **40**, 243-248.
223. J.-Y. Lin and S.-W. Chou, *RSC Adv.*, 2013, **3**, 2043.
224. X. Guo, F. Zhang, D. G. Evans and X. Duan, *Chem. Commun.*, 2010, **46**, 5197-5210.
225. Q. Wang and D. O'Hare, *Chem. Rev.*, 2012.
226. X.-M. Liu, Y.-H. Zhang, X.-G. Zhang and S.-Y. Fu, *Electrochim. Acta*, 2004, **49**, 3137-3141.
227. H. KuanXin, Z. Xiaogang and L. Juan, *Electrochim. Acta*, 2006, **51**, 1289-1292.
228. L.-H. Su and X.-G. Zhang, *J. Power Sources*, 2007, **172**, 999-1006.
229. L.-H. Su, X.-G. Zhang, C.-H. Mi and Y. Liu, *J. Power Sources*, 2008, **179**, 388-394.
230. L. H. Su, X. G. Zhang, C. H. Mi, B. Gao and Y. Liu, *Phys. Chem. Chem. Phys.*, 2009, **11**, 2195-2202.
231. J. W. Jiang, X. G. Zhang, L. H. Su, L. J. Zhang and F. Zhang, *Chinese Journal of Inorganic Chemistry*, 2010, **26**, 1623-1628.
232. Y. Wang, W. Yang, S. Zhang, D. G. Evans and X. Duan, *J. Electrochem. Soc.*, 2005, **152**, A2130-A2137.
233. Z.-A. Hu, Y.-L. Xie, Y.-X. Wang, H.-Y. Wu, Y.-Y. Yang and Z.-Y. Zhang, *Electrochim. Acta*, 2009, **54**, 2737-2741.
234. Y. Wang, W. Yang and J. Yang, *Electrochem. Solid-St. Lett.*, 2007, **10**, A233.
235. Y. Wang, W. Yang, C. Chen and D. G. Evans, *J. Power Sources*, 2008, **184**, 682-690.
236. M. A. Woo, M.-S. Song, T. W. Kim, I. Y. Kim, J.-Y. Ju, Y. S. Lee, S. J. Kim, J.-H. Choy and S.-J. Hwang, *J. Mater. Chem.*, 2011, **21**, 4286.
237. X. Liu, R. Ma, Y. Bando and T. Sasaki, *Adv. Mater.*, 2012, **24**, 2148-2153.
238. V. Gupta, S. Gupta and N. Miura, *J. Power Sources*, 2008, **175**, 680-685.
239. V. Gupta, S. Gupta and N. Miura, *J. Power Sources*, 2008, **177**, 685-689.
240. V. Gupta, S. Gupta and N. Miura, *J. Power Sources*, 2009, **189**, 1292-1295.
241. P. Y. Loh, K. K. Lee, Y. Ng, C. H. Sow and W. S. Chin, *Electrochem. Commun.*, 2014, **43**, 9-12.
242. H. Chen, L. Hu, M. Chen, Y. Yan and L. Wu, *Adv. Funct. Mater.*, 2014, **24**, 934-942.
243. P. Vialat, C. Mousty, C. Taviot-Gueho, G. Renaudin, H. Martinez, J.-C. Dupin, E. Elkaim and F. Leroux, *Adv. Funct. Mater.*, 2014, n/a-n/a.
244. C.-C. Hu and C.-Y. Cheng, *Electrochem. Solid-St. Lett.*, 2002, **5**, A43-A46.
245. X. Lu, X. Huang, S. Xie, T. Zhai, C. Wang, P. Zhang, M. Yu, W. Li, C. Liang and Y. Tong, *J. Mater. Chem.*, 2012, **22**, 13357-13364.
246. V. Gupta, T. Kawaguchi and N. Miura, *Mater. Res. Bull.*, 2009, **44**, 202-206.

247. J.-H. Zhong, A.-L. Wang, G.-R. Li, J.-W. Wang, Y.-N. Ou and Y.-X. Tong, *J. Mater. Chem.*, 2012, **22**, 5656.

248. C. Yuan, J. Li, L. Hou, X. Zhang, L. Shen and X. W. D. Lou, *Adv. Funct. Mater.*, 2012, **22**, 4592-4597.

249. T. Y. Wei, C. H. Chen, H. C. Chien, S. Y. Lu and C. C. Hu, *Adv. Mater.*, 2010, **22**, 347-351.

250. G. Hu, C. Tang, C. Li, H. Li, Y. Wang and H. Gong, *J. Electrochem. Soc.*, 2011, **158**, A695-A699.

251. Y. Q. Wu, X. Y. Chen, P. T. Ji and Q. Q. Zhou, *Electrochim. Acta*, 2011, **56**, 7517-7522.

252. M.-C. Liu, L.-B. Kong, C. Lu, X.-M. Li, Y.-C. Luo and L. Kang, *ACS Appl. Mater. Interfaces*, 2012, **4**, 4631-4636.

253. M. C. Liu, L. B. Kong, C. Lu, X. M. Li, Y. C. Luo and L. Kang, *ACS Appl Mater Interfaces*, 2012, **4**, 4631-4636.

254. J.-J. Deng, J.-C. Deng, Z.-L. Liu, H.-R. Deng and B. Liu, *J. Mater. Sci.*, 2009, **44**, 2828-2835.

255. J.-W. Lang, L.-B. Kong, M. Liu, Y.-C. Luo and L. Kang, *J. Electrochem. Soc.*, 2010, **157**, A1341.

256. C. Wang, X. Zhang, D. Zhang, C. Yao and Y. Ma, *Electrochim. Acta*, 2012, **63**, 220-227.

257. G. Wang, L. Zhang, J. Kim and J. Zhang, *J. Power Sources*, 2012, **217**, 554-561.

258. J. Li, M. Yang, J. Wei and Z. Zhou, *Nanoscale*, 2012, **4**, 4498-4503.

259. H. Jiang, J. Ma and C. Li, *Chem. Commun.*, 2012, **48**, 4465-4467.

260. C. Yuan, J. Li, L. Hou, L. Yang, L. Shen and X. Zhang, *J. Mater. Chem.*, 2012, **22**, 16084-16090.

261. H. Wang, Q. Gao and L. Jiang, *Small*, 2011, **7**, 2454-2459.

262. J. Xiao and S. Yang, *RSC Adv.*, 2011, **1**, 588-595.

263. W. Zhu, Z. Lu, G. Zhang, X. Lei, Z. Chang, J. Liu and X. Sun, *J. Mater. Chem. A*, 2013, **1**, 8327-8331.

264. L. Su, L. Gong and J. Gao, *J. Power Sources*, 2012, **209**, 141-146.

265. X. L. Li, J. F. Liu and Y. D. Li, *Mater. Chem. Phys.*, 2003, **80**, 222-227.

266. R. Zou, K. Xu, T. Wang, G. He, Q. Liu, X. Liu, Z. Zhang and J. Hu, *J. Mater. Chem. A*, 2013, **1**, 8560-8566.

267. D. Cai, S. Xiao, D. Wang, B. Liu, L. Wang, Y. Liu, H. Li, Y. Wang, Q. Li and T. Wang, *Electrochim. Acta*, 2014.

268. Q. Wang, X. Wang, B. Liu, G. Yu, X. Hou, D. Chen and G. Shen, *J. Mater. Chem. A*, 2013, **1**, 2468-2473.

269. J. Chang, J. Sun, C. Xu, H. Xu and L. Gao, *Nanoscale*, 2012, **4**, 6786-6791.

270. R. R. Salunkhe, K. Jang, H. Yu, S. Yu, T. Ganesh, S.-H. Han and H. Ahn, *J. Alloys Compd.*, 2011, **509**, 6677-6682.

271. R. R. Salunkhe, K. Jang, S.-w. Lee and H. Ahn, *RSC Adv.*, 2012, **2**, 3190-3193.

272. G. Zhang and X. W. Lou, *Adv Mater*, 2013, **25**, 976-979.

273. G. Q. Zhang, H. B. Wu, H. E. Hoster, M. B. Chan-Park and X. W. Lou, *Energy Environ. Sci.*, 2012, **5**, 9453-9456.

274. D. P. Dubal, A. D. Jagadale, S. V. Patil and C. D. Lokhande, *Mater. Res. Bull.*, 2012, **47**, 1239-1245.

275. H. Chen, J. Jiang, L. Zhang, H. Wan, T. Qi and D. Xia, *Nanoscale*, 2013, **5**, 8879-8883.

276. J. Pu, T. Wang, H. Wang, Y. Tong, C. Lu, W. Kong and Z. Wang, *ChemPlusChem*, 2014, **79**, 577-583.

277. L. Yu, G. Zhang, H. B. Wu and X. W. Lou, *Angew. Chem.*, 2014, **126**, 3785-3788.

278. Y. Li, L. Cao, L. Qiao, M. Zhou, Y. Yang, P. Xiao and Y. Zhang, *J. Mater. Chem. A*, 2014, **2**, 6540-6548.

279. W. Du, Z. Zhu, Y. Wang, J. Liu, W. Yang, X. Qian and H. Pang, *RSC Adv.*, 2014, **4**, 6998-7002.

280. H. C. Chen, J. J. Jiang, L. Zhang, D. D. Xia, Y. D. Zhao, D. Q. Guo, T. Qi and H. Z. Wan, *J. Power Sources*, 2014, **254**, 249-257.

281. H. Z. Wan, J. J. Jiang, J. W. Yu, K. Xu, L. Miao, L. Zhang, H. C. Chen and Y. J. Ruan, *CrystEngComm*, 2013, **15**, 7649-7651.

282. J. Pu, F. L. Cui, S. B. Chu, T. L. Wang, E. H. Sheng and Z. H. Wang, *ACS Sustainable Chem. Eng.*, 2014, **2**, 809-815.

283. K. Karthikeyan, D. Kalpana and N. Renganathan, *Ionics*, 2009, **15**, 107-110.

284. M. Davis, C. Gümeci, B. Black, C. Korzeniewski and L. Hope-Weeks, *RSC Adv.*, 2012, **2**, 2061.

285. J.-M. Luo, B. Gao and X.-G. Zhang, *Mater. Res. Bull.*, 2008, **43**, 1119-1125.

286. P. Xu, K. Ye, D. Cao, J. Huang, T. Liu, K. Cheng, J. Yin and G. Wang, *J. Power Sources*, 2014, **268**, 204-211.

287. F. Zhang, L. Hao, L. J. Zhang and X. G. Zhang, *Int. J. Electrochem. Sc.*, 2011, **6**, 2943-2954.

288. D. Y. Lee, S. J. Yoon, N. K. Shrestha, S. H. Lee, H. Ahn and S. H. Han, *Microporous Mesoporous Mater.*, 2012, **153**, 163-165.

289. Z. Lu, W. Zhu, X. Lei, G. R. Williams, D. O'Hare, Z. Chang, X. Sun and X. Duan, *Nanoscale*, 2012, **4**, 3640-3643.

290. H. Pang, Z. Yan, W. Wang, J. Chen, J. Zhang and H. Zheng, *Nanoscale*, 2012, **4**, 5946-5953.

291. H. Pang, Y. Liu, J. Li, Y. Ma, G. Li, Y. Ai, J. Chen, J. Zhang and H. Zheng, *Nanoscale*, 2013, **5**, 503-507.

292. J. Liu, C. Cheng, W. Zhou, H. Li and H. J. Fan, *Chem. Commun.*, 2011, **47**, 3436-3438.

293. C. Yan, H. Jiang, T. Zhao, C. Li, J. Ma and P. S. Lee, *J. Mater. Chem.*, 2011, **21**, 10482.

294. C. Shang, S. Dong, S. Wang, D. Xiao, P. Han, X. Wang, L. Gu and G. Cui, *ACS Nano*, 2013, **7**, 5430-5436.

295. F. Yang, J. Yao, F. Liu, H. He, M. Zhou, P. Xiao and Y. Zhang, *J. Mater. Chem. A*, 2013, **1**, 594.

296. X. Wang, A. Sumboja, M. Lin, J. Yan and P. S. Lee, *Nanoscale*, 2012, **4**, 7266-7272.

297. D. T. Dam, X. Wang and J.-M. Lee, *RSC Adv.*, 2012, **2**, 10512-10518.

298. J. Liu, J. Jiang, C. Cheng, H. Li, J. Zhang, H. Gong and H. J. Fan, *Adv. Mater.*, 2011, **23**, 2076-2081.

299. C. Guan, J. Liu, C. Cheng, H. Li, X. Li, W. Zhou, H. Zhang and H. J. Fan, *Energy Environ. Sci.*, 2011, **4**, 4496-4499.

300. X. Xia, J. Tu, Y. Zhang, X. Wang, C. Gu, X.-B. Zhao and H. J. Fan, *ACS Nano*, 2012.

301. X. Xia, J. Tu, Y. Zhang, J. Chen, X. Wang, C. Gu, C. Guan, J. Luo and H. J. Fan, *Chem. Mater.*, 2012, **24**, 3793-3799.

302. C. Guan, X. Li, Z. Wang, X. Cao, C. Soci, H. Zhang and H. J. Fan, *Adv. Mater.*, 2012, **24**, 4186-4190.

303. L.-Q. Mai, F. Yang, Y.-L. Zhao, X. Xu, L. Xu and Y.-Z. Luo, *Nat. Commun.*, 2011, **2**, 381.

304. K. M. Hercule, Q. Wei, A. M. Khan, Y. Zhao, X. Tian and L. Mai, *Nano Lett.*, 2013, **13**, 5685-5691.

305. H. Zhang, Y. Chen, W. Wang, G. Zhang, M. Zhuo, H. Zhang, T. Yang, Q. Li and T. Wang, *J. Mater. Chem. A*, 2013, **1**, 8593-8600.

306. K. Xu, R. Zou, W. Li, Y. Xue, G. Song, Q. Liu, X. Liu and J. Hu, *J. Mater. Chem. A*, 2013, **1**, 9107-9113.

307. J. Han, Y. Dou, J. Zhao, M. Wei, D. G. Evans and X. Duan, *Small*, 2013, **9**, 98-106.

308. C. Zhou, Y. Zhang, Y. Li and J. Liu, *Nano Lett.*, 2013, **13**, 2078-2085.

309. L. Han, P. Tang and L. Zhang, *Nano Energy*, 2014, **7**, 42-51.

310. M. Zhi, C. Xiang, J. Li, M. Li and N. Wu, *Nanoscale*, 2013, **5**, 72-88.

311. H. Kuan-Xin, W. Quan-Fu, Z. Xiao-gang and W. Xin-Lei, *J. Electrochem. Soc.*, 2006, **153**, A1568.

312. L.-H. Su, X.-G. Zhang and Y. Liu, *J. Solid State Electrochem.*, 2007, **12**, 1129-1134.

313. Z. Fan, J. Chen, K. Cui, F. Sun, Y. Xu and Y. Kuang, *Electrochim. Acta*, 2007, **52**, 2959-2965.

314. H. Zheng, F. Tang, M. Lim, T. Rufford, A. Mukherji, L. Wang and G. Lu, *J. Power Sources*, 2009, **193**, 930-934.

315. X. Wang, X. Han, M. Lim, N. Singh, C. L. Gan, M. Jan and P. S. Lee, *J. Phys. Chem. C*, 2012, **116**, 12448-12454.

316. R. R. Salunkhe, K. Jang, S.-w. Lee, S. Yu and H. Ahn, *J. Mater. Chem.*, 2012, **22**, 21630-21635.

317. J. Yang, C. Yu, X. Fan, Z. Ling, J. Qiu and Y. Gogotsi, *J. Mater. Chem. A*, 2013, **1**, 1963-1968.

318. Y. I. Yoon, Ko, J.M., *Int. J. Electrochem. Sc.*, 2008, **3**, 1340-1347.

319. Y. Y. Liang, M. G. Schwab, L. J. Zhi, E. Mugnaioli, U. Kolb, X. L. Feng and K. Mullen, *J. Am. Chem. Soc.*, 2010, **132**, 15030-15037.

320. Z. Tai, J. Lang, X. Yan and Q. Xue, *J. Electrochem. Soc.*, 2012, **159**, A485.

321. J. Lang, X. Yan and Q. Xue, *J. Power Sources*, 2011, **196**, 7841-7846.

322. C. Yuan, L. Shen, F. Zhang, X. Lu, D. Li and X. Zhang, *J. Colloid Interface Sci.*, 2010, **349**, 181-185.

323. C.-Y. Chen, Z.-Y. Shih, Z. Yang and H.-T. Chang, *J. Power Sources*, 2012, **215**, 43-47.

324. Z. Xu, Z. Li, X. Tan, C. M. B. Holt, L. Zhang, B. S. Amirkhiz and D. Mitlin, *RSC Adv.*, 2012, **2**, 2753-2755.

325. G. Zhang and X. W. Lou, *Sci. Rep.*, 2013, **3**, 1470.

326. L. Wan, J. Xiao, F. Xiao and S. Wang, *ACS Appl. Mater. Interfaces*, 2014, **6**, 7735-7742.

327. S. Chen, J. Zhu and X. Wang, *J. Phys. Chem. C*, 2010, **114**, 11829-11834.

328. J. Yan, T. Wei, W. Qiao, B. Shao, Q. Zhao, L. Zhang and Z. Fan, *Electrochim. Acta*, 2010, **55**, 6973-6978.

329. C. Xiang, M. Li, M. Zhi, A. Manivannan and N. Wu, *J. Power Sources*, 2013, **226**, 65-70.

330. W. Zhang, F. Liu, Q. Li, Q. Shou, J. Cheng, L. Zhang, B. J. Nelson and X. Zhang, *Phys. Chem. Chem. Phys.*, 2012, **14**, 16331-16337.

331. Z. Li, J. Wang, L. Niu, J. Sun, P. Gong, W. Hong, L. Ma and S. Yang, *J. Power Sources*, 2014, **245**, 224-231.

332. B. Wang, J. Park, D. Su, C. Wang, H. Ahn and G. Wang, *J. Mater. Chem.*, 2012, **22**, 15750-15756.

333. Q. Wang, L. Jiao, H. Du, Y. Si, Y. Wang and H. Yuan, *J. Mater. Chem.*, 2012, **22**, 21387-21391.

334. X. Wang, W. S. Liu, X. Lu and P. S. Lee, *J. Mater. Chem.*, 2012, **22**, 23114-23119.

335. Y. Cheng, H. Zhang, C. V. Varanasi and J. Liu, *Energy Environ. Sci.*, 2013, **6**, 3314-3321.

336. S. Peng, L. Li, C. Li, H. Tan, R. Cai, H. Yu, S. Mhaisalkar, M. Srinivasan, S. Ramakrishna and Q. Yan, *Chem. Commun.*, 2013, **49**, 10178-10180.

337. L. Jiang, R. Zou, W. Li, J. Sun, X. Hu, Y. Xue, G. He and J. Hu, *J. Mater. Chem. A*, 2013, **1**, 478.

338. W. Zhou, J. Liu, T. Chen, K. S. Tan, X. Jia, Z. Luo, C. Cong, H. Yang, C. M. Li and T. Yu, *Phys. Chem. Chem. Phys.*, 2011, **13**, 14462-14465.

339. H.-W. Wang, Z.-A. Hu, Y.-Q. Chang, Y.-L. Chen, Z.-Y. Zhang, Y.-Y. Yang and H.-Y. Wu, *Mater. Chem. Phys.*, 2011, **130**, 672-679.

340. B. Wang, Y. Wang, J. Park, H. Ahn and G. Wang, *J. Alloys Compd.*, 2011, **509**, 7778-7783.

341. A. Chidembo, S. H. Aboutalebi, K. Konstantinov, M. Salari, B. Winton, S. A. Yamini, I. P. Nevirkovets and H. K. Liu, *Energy Environ. Sci.*, 2012, **5**, 5236.

342. L. Wang, D. Wang, X. Y. Dong, Z. J. Zhang, X. F. Pei, X. J. Chen, B. Chen and J. Jin, *Chem. Commun.*, 2011, **47**, 3556-3558.

343. Z. Liu, R. Ma, M. Osada, N. Iyi, Y. Ebina, K. Takada and T. Sasaki, *J. Am. Chem. Soc.*, 2006, **128**, 4872-4880.

344. X. Dong, L. Wang, D. Wang, C. Li and J. Jin, *Langmuir*, 2011, **28**, 293-298.

345. L. Zhang, X. Zhang, L. Shen, B. Gao, L. Hao, X. Lu, F. Zhang, B. Ding and C. Yuan, *J. Power Sources*, 2012, **199**, 395-401.

346. J. Fang, M. Li, Q. Li, W. Zhang, Q. Shou, F. Liu, X. Zhang and J. Cheng, *Electrochim. Acta*, 2012, **85**, 248-255.

347. H.-W. Wang, Z.-A. Hu, Y.-Q. Chang, Y.-L. Chen, H.-Y. Wu, Z.-Y. Zhang and Y.-Y. Yang, *J. Mater. Chem.*, 2011, **21**, 10504-10511.

348. C. Yuan, L. Yang, L. Hou, J. Li, Y. Sun, X. Zhang, L. Shen, X. Lu, S. Xiong and X. W. Lou, *Adv. Funct. Mater.*, 2012, **22**, 2560-2566.

349. C. Zhao, X. Wang, S. Wang, Y. Wang, Y. Zhao and W. Zheng, *Int. J. Hydrogen Energy*, 2012, **37**, 11846-11852.

350. D. S. Su and R. Schlögl, *ChemSusChem*, 2010, **3**, 136-168.

351. J. Zhang, L.-B. Kong, J.-J. Cai, Y.-C. Luo and L. Kang, *J. Solid State Electrochem.*, 2010, **14**, 2065-2075.

352. M. Dai, L. Song, J. T. LaBelle and B. D. Vogt, *Chem. Mater.*, 2011, **23**, 2869-2878.

353. Y.-K. Lv, Y.-L. Feng, L.-H. Gan, M.-X. Liu, L. Xu, C. Liu, H.-W. Zheng and J. Li, *J. Solid State Chem.*, 2012, **185**, 198-205.

354. H.-C. Chien, W.-Y. Cheng, Y.-H. Wang and S.-Y. Lu, *Adv. Funct. Mater.*, 2012, **22**, 5038-5043.

355. J. Zhi, S. Deng, Y. Zhang, Y. Wang and A. Hu, *J. Mater. Chem. A*, 2013, **1**, 3171-3176.

356. R. R. Salunkhe, B. P. Bastakoti, C.-T. Hsu, N. Suzuki, J. H. Kim, S. X. Dou, C.-C. Hu and Y. Yamauchi, *Chem.-Eur. J.*, 2014, **20**, 3084-3088.

357. W. Xing, S. Qiao, X. Wu, X. Gao, J. Zhou, S. Zhuo, S. B. Hartono and D. Hulicova-Jurcakova, *J. Power Sources*, 2011, **196**, 4123-4127.

358. J. K. Chang, S. H. Hsu, I. W. Sun and W. T. Tsai, *J. Phys. Chem. C*, 2008, **112**, 1371-1376.

359. D. Ming-Jay, H. Fu-Lu, I. W. Sun, T. Wen-Ta and C. Jeng-Kuei, *Nanotechnology*, 2009, **20**, 175602.

360. J.-K. Chang, C.-M. Wu and I. W. Sun, *J. Mater. Chem.*, 2010, **20**, 3729.

361. C.-M. Wu, C.-Y. Fan, I. W. Sun, W.-T. Tsai and J.-K. Chang, *J. Power Sources*, 2011, **196**, 7828-7834.

362. X. H. Xia, J. P. Tu, Y. Q. Zhang, Y. J. Mai, X. L. Wang, C. D. Gu and X. B. Zhao, *J. Phys. Chem. C*, 2011, **115**, 22662-22668.

363. G. X. Pan, X. Xia, F. Cao, P. S. Tang and H. F. Chen, *Electrochim. Acta*, 2012, **63**, 335-340.

364. T. Liu, S. Xu, L. Wang, J. Chu, Q. Wang, X. Zhu, N. Bing and P. K. Chu, *J. Mater. Chem.*, 2011, **21**, 19093.

365. M. Li, S. Xu, T. Liu, F. Wang, P. Yang, L. Wang and P. K. Chu, *J. Mater. Chem. A*, 2013, **1**, 532-539.

366. L. Yang, S. Cheng, Y. Ding, X. Zhu, Z. L. Wang and M. Liu, *Nano Lett.*, 2012, **12**, 321-325.

367. L. Huang, D. Chen, Y. Ding, S. Feng, Z. L. Wang and M. Liu, *Nano Lett.*, 2013, **13**, 3135-3139.

368. R. B. Rakhi, W. Chen, D. Cha and H. N. Alshareef, *Nano Lett.*, 2012.

369. L. Hu and Y. Cui, *Energy Environ. Sci.*, 2012, **5**, 6423-6435.

370. C. Yuan, L. Hou, D. Li, L. Shen, F. Zhang and X. Zhang, *Electrochim. Acta*, 2011, **56**, 6683-6687.

371. L. Shen, Q. Che, H. Li and X. Zhang, *Adv. Funct. Mater.*, 2014, **24**, 2630-2637.

372. J. Zhao, Z. Lu, M. Shao, D. Yan, M. Wei, D. G. Evans and X. Duan, *RSC Adv.*, 2013, **3**, 1045-1049.

373. Z. P. Chen, W. C. Ren, L. B. Gao, B. L. Liu, S. F. Pei and H. M. Cheng, *Nat. Mater.*, 2011, **10**, 424-428.

374. X. Xia, D. Chao, Z. Fan, C. Guan, X. Cao, H. Zhang and H. J. Fan, *Nano Lett.*, 2014, **14**, 1651-1658.

375. X.-C. Dong, H. Xu, X.-W. Wang, Y.-X. Huang, M. B. Chan-Park, H. Zhang, L.-H. Wang, W. Huang and P. Chen, *ACS Nano*, 2012.

376. L. Cao, F. Xu, Y. Y. Liang and H. L. Li, *Adv. Mater.*, 2004, **16**, 1853-1857.

377. Y. Y. Liang, L. Cao, L. B. Kong and H. L. Li, *J. Power Sources*, 2004, **136**, 197-200.

378. Y. Y. Liang, S. J. Bao and H. L. Li, *J. Solid State Electrochem.*, 2007, **11**, 571-576.

379. L.-B. Kong, J.-J. Cai, L.-L. Sun, J. Zhang, Y.-C. Luo and L. Kang, *Mater. Chem. Phys.*, 2010, **122**, 368-373.

380. Y. Zhu, S. Murali, M. D. Stoller, K. J. Ganesh, W. Cai, P. J. Ferreira, A. Pirkle, R. M. Wallace, K. A. Cychosz, M. Thommes, D. Su, E. A. Stach and R. S. Ruoff, *Science*, 2011, **332**, 1537-1541.

381. K. A. Ritter and J. W. Lyding, *Nat. Mater.*, 2009, **8**, 235-242.

382. K. K. Lee, S. Deng, H. M. Fan, S. Mhaisalkar, H. R. Tan, E. S. Tok, K. P. Loh, W. S. Chin and C. H. Sow, *Nanoscale*, 2012, **4**, 2958-2961.

383. L.-B. Kong, M. Liu, J.-W. Lang, Y.-C. Luo and L. Kang, *J. Electrochem. Soc.*, 2009, **156**, A1000-A1004.

384. J.-W. Lang, L.-B. Kong, M. Liu, Y.-C. Luo and L. Kang, *J. Electrochem. Soc.*, 2010, **157**, A1341-A1346.

385. Y.-Y. Liang, H.-L. Li and X.-G. Zhang, *Mat. Sci. Eng. A-Struct.*, 2008, **473**, 317-322.

386. C. Tang, Z. Tang and H. Gong, *J. Electrochem. Soc.*, 2012, **159**, A651-A656.

387. J. Xiao and S. Yang, *J. Mater. Chem.*, 2012, **22**, 12253-12262.

388. H. Wang, Q. Gao and J. Hu, *J. Power Sources*, 2010, **195**, 3017-3024.

389. H. Wang, C. M. B. Holt, Z. Li, X. Tan, B. S. Amirkhiz, Z. Xu, B. C. Olsen, T. Stephenson and D. Mitlin, *Nano Res.*, 2012, **5**, 605-617.

390. W. Zhang, C. Ma, J. Fang, J. Cheng, X. Zhang, S. Dong and L. Zhang, *RSC Adv.*, 2013, **3**, 2483.

Journal of Materials Chemistry A Accepted Manuscript

391. J. Xu, Q. Wang, X. Wang, Q. Xiang, B. Liang, D. Chen and G. Shen, *ACS Nano*, 2013, **7**, 5453-5462.
392. J. Li and F. Gao, *J. Power Sources*, 2009, **194**, 1184-1193.

5

Journal of Materials Chemistry A Accepted Manuscript